Title
Extending Stochastic Representations of Geomagnetic Axial Dipole Evolution

Author
Sadhasivan, Mayuri

Publication Date
2018

UNIVERSITY OF CALIFORNIA SAN DIEGO

Extending Stochastic Representations of Geomagnetic Axial Dipole Evolution

A thesis submitted in partial satisfaction of the
requirements for the degree
Master of Science

in

Earth Sciences

by

Mayuri Sadhasivan

Committee in charge:

Professor Catherine Constable, Chair
Professor Duncan Agnew
Professor Jeffrey Gee

2018

The thesis of Mayuri Sadhasivan is approved, and it is acceptable in quality and form for publication on microfilm and electronically:

Chair

University of California San Diego

2018

DEDICATION

To every person who has ever taught me anything - I am 99 % sure I wouldn't be here without you.

TABLE OF CONTENTS

LIST OF FIGURES

LIST OF TABLES

ACKNOWLEDGEMENTS

Thanks to Bruce Buffett and Matthias Morzfeld for sharing illuminative discussions and MATLAB code. Thanks also to Professors Duncan Agnew and Jeffrey Gee for taking the time to read my thesis and offering helpful suggestions. I'd especially like to acknowledge my advisor, Professor Catherine Constable for giving me the time I needed to learn to do things that made me initially uncomfortable, reading my thesis many times over, and constantly setting an example of the kind of person who is humble even when they have done some really amazing things. Finally, I have so much gratitude for my family, friends, and any teachers who clawed past my tenacity and taught me perceive a difficult situation differently - I owe any and all of my creative problem solving abilities to their persistence, patience, and forgiveness.

ABSTRACT OF THE THESIS

Extending Stochastic Representations of Geomagnetic Axial Dipole Evolution

by

Mayuri Sadhasivan

Master of Science in Earth Sciences

University of California San Diego, 2018

Professor Catherine Constable, Chair

Stochastic models have been developed to describe the time-varying axial dipole moment of the geomagnetic field sustained by turbulent fluid motions in Earth's outer core. Previous stochastic models failed to predict the high-frequency variations present in the frequency spectrum of the axial dipole moment. In this study, we recast the Langevin model - which describes temporal variations in the axial dipole moment as a nonlinear tug-of-war between the moment's slow drift towards and higher-frequency fluctuations away from equilibrium - as an order-3 continuous-autoregressive model, which is a linear differential equation driven by white noise. Both models are parametrized by a diffusion coefficient D_{eq} that dictates the relative influence between fluctuations and drift on axial dipole behavior, timescales $\{\tau_m, \tau_s\}$ by which fluctuations away from steady state occur, and a drift timescale τ_l by which the axial dipole moment returns to steady state. Numerical simulations of our new model have frequency spectra that resemble a recently-published composite spectrum for the geomagnetic axial dipole moment. The latter goes like f^0 at lowest frequencies, f^{-2} at intermediate frequencies, f^{-4} at higher frequencies and f^{-6} at highest frequencies. Our model parameters facilitate such a shape; D_{eq} dictates the scale of the total spectrum and $\{\tau_l, \tau_m, \tau_s\}$ dictate the transition frequencies between adjacent regimes. Estimating the model parameters by comparison with the composite spectrum, we infer that $\{\tau_l, \tau_m, \tau_s\}$ correspond to the timescales expected for Ohmic diffusion, MAC waves, and torsional oscillations, respectively in Earth's outer core while D_{eq} reflects a rate at which Ohmic diffusion re-stabilizes the axial dipole field on ten-thousand year timescales while MAC waves and torsional oscillations render it unstable on decadal and sub-decadal timescales.

Chapter 1

Earth's Magnetic Field and a Review of Basic Stochastic Models

1.1 Background

The geomagnetic field acts as an energy barrier that shields Earth's atmosphere from cosmic radiation and the solar wind, potentially protecting life on Earth. Awareness of the geomagnetic field has shaped human history. The geomagnetic field was used as early as the Age of Exploration for ship navigation [Jackson et al., 2000] and even prior to that, the field was used by ancient cultures to develop an observational understanding of the elements in nature.

Today, precise measurements of the geomagnetic field strength and direction facilitate our understanding of deep Earth structure and composition. Any magnetic field must originate from a current source [Griffiths, 2017]. The geomagnetic field was initially presumed to be of external origin since the Earth was assumed to be entirely solid. Yet in 1838 Gauss demonstrated that the field is of primarily internal origin by fitting a spherical harmonic model to his field measurements. The fit predicted negligible influence from external sources, indicating that the source current lies in Earth's interior [Glassmeier and Tsurutani, 2014].

Seismic tomography, akin to an ultrasound of the Earth, helps scientists visualize and model Earth's internal structure. Vanishing shear wave velocities in seismic velocity inversion models indicate the presence of a fluid shell at about 2891 km depth [Shearer, 2009]. Iron being an abundant element in the solar system, Earth's moment of inertia requiring a density increase towards the center [Gutenberg, 1951], and iron being heavy enough to sink towards Earth's center during accretion, all point to an iron-rich outer core. The outer core current and resulting field are called the geodynamo and it is believed to have existed for as long as 4.2 billion years. The longevity of the geomagnetic field and its temporal evolution are tied to Earth's thermal evolution as entropy production in the Earth's outer core drives the vigorous convection required to sustain a global magnetic field over geologic timescales [Moffatt, 1978], [O'Rourke et al., 2017].

1.2 Representing the Geomagnetic Field Using Spherical Harmonics

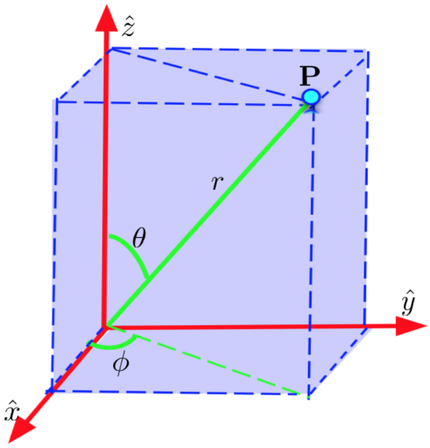

Figure 1.1: Spherical coordinate system. The field $\vec{B}(r, \theta, \phi)$ is measured at point P, with colatitude θ, longitude ϕ and radius r.

Fluid motions in the outer core produce changes in the externally-measured field. We define (r, θ, ϕ) according to Figure 1.1. As shown by Gauss, the presumed source-free region in Earth's mantle and above allow the representation of the geomagnetic field, $\vec{B}(r, \theta, \phi)$, by a magnetic potential $\psi(r, \theta, \phi)$ with

$$\vec{B}(r, \theta, \phi) = -\nabla\psi. \tag{1.1}$$

This implies that the potential satisfies Laplace's equation in the region because a magnetic field never diverges, i.e.

$$0 = \nabla \cdot \vec{B} = -\nabla^2\psi. \tag{1.2}$$

We prefer to solve for the potential in spherical coordinates because it allows for a more physically useful solution relevant to the Earth. Applying separation of variables, Gauss demonstrated that the solution looks like

$$\psi(r,\theta,\phi) = a\sum_{l=1}^{\infty}\sum_{m=0}^{l}\left(\frac{a}{r}\right)^{l+1}\Big(g_l^m\cos(m\phi) + h_l^m\sin(m\phi)\Big)P_l^m\Big(\cos(\theta)\Big) \tag{1.3}$$

where each $P_l^m(x)$ is called an "associated Legendre polynomial". Each associated Legendre polynomial is identified by a degree and order pair, (l,m), where $m \in [-l,l]$. The first few associated Legendre polynomials are

$$\begin{aligned}
P_0^0(x) &= 1 \\
P_1^0(x) &= x \\
P_1^1(x) &= -(1-x^2)^{\frac{1}{2}} \\
P_2^0(x) &= \frac{1}{2}(3x^2-1) \\
P_2^1(x) &= -3x(1-x^2)^{\frac{1}{2}} \\
P_2^2(x) &= 3(1-x^2) \\
P_3^0(x) &= \frac{1}{2}x(5x^2-3).
\end{aligned} \tag{1.4}$$

Often times the series solution is written as

$$\psi(r,\theta,\phi) = a\sum_{l=1}^{\infty}\sum_{m=0}^{l}\left(\frac{a}{r}\right)^{l+1}c_l^m e^{im\phi}P_l^m\Big(\cos(\theta)\Big) \tag{1.5}$$

where c_l^m is assumed to be a complex amplitude instead of $\{g_l^m, h_l^m\}$, which are assumed to be real amplitudes. Each angular term, $Y_l^m(\theta,\phi) = e^{im\phi}P_l^m\Big(\cos(\theta)\Big)$, is called a spherical harmonic. Note that solutions to Laplace's equation that explode at infinite radius have been removed because we study the part of the geomagnetic field that exists at the surface of Earth and outward.

The first few spherical harmonics are

$$
\begin{aligned}
Y_0^0(\theta,\phi) &= \left(\frac{1}{4\pi}\right)^{\frac{1}{2}} \\
Y_1^0(\theta,\phi) &= \left(\frac{3}{4\pi}\right)^{\frac{1}{2}}\cos(\theta) \\
Y_1^{\pm 1}(\theta,\phi) &= \mp\left(\frac{3}{8\pi}\right)^{\frac{1}{2}}\sin(\theta)e^{\pm i\phi} \\
Y_2^0(\theta,\phi) &= \left(\frac{5}{16\pi}\right)^{\frac{1}{2}}(3\cos^2(\theta)-1) \\
Y_2^{\pm 1}(\theta,\phi) &= \mp\left(\frac{15}{8\pi}\right)^{\frac{1}{2}}\sin(\theta)\cos(\theta)e^{\pm i\phi} \\
Y_2^{\pm 2}(\theta,\phi) &= \left(\frac{15}{32\pi}\right)^{\frac{1}{2}}\sin^2(\theta)e^{\pm 2i\phi} \\
Y_3^0(\theta,\phi) &= \left(\frac{7}{16\pi}\right)^{\frac{1}{2}}\Big(5\cos^3(\theta)-3\cos(\theta)\Big).
\end{aligned}
\tag{1.6}
$$

Recognizing that $e^{im\phi} = \cos(m\phi) + i\sin(m\phi)$, we show the structure of the real part, corresponding to the cosine, and the magnitude of the first few spherical harmonic functions in Figure 1.2 to help with visualization. The magnitudes are colored to show the role of the complex exponential before taking the magnitude because $|e^{im\phi}| = 1$.

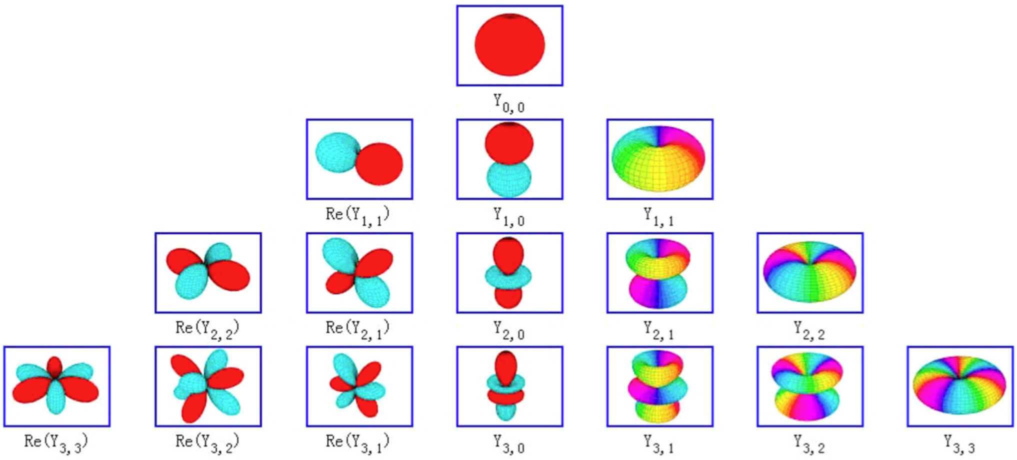

Figure 1.2: The real components of the first few spherical harmonics are on the left. On the right, the absolute values of and the wavelengths in ϕ in the first few spherical harmonics are given as the shape and the color, respectively. [Wang et al., 2016]

On the left in Figure 1.2, red indicates where the real part of the spherical harmonic is positive and blue indicates where the real part is negative. The shape caves in where the value of the real part approaches 0 and likewise balloons out where the real part approaches a large absolute value. Computing the absolute value of each spherical harmonic yields the plots on the right in Figure 1.2. Again, each shape caves in where the value of the absolute value approaches 0 and balloons out where the absolute value is large. The spherical harmonic order m dictates the color pattern on the surface; the real and the imaginary part of $e^{im\phi} = \cos(m\phi) + i\sin(m\phi)$ each have m repeated wavelengths within the domain $\phi \in [0, 2\pi]$. Each rainbow cycle in Figure 1.2 represents one, full wavelength in ϕ so we see the cycle repeat once when $m = 1$, twice when $m = 2$, and so on.

The spherical harmonics are useful because they give us a way to decompose any function of θ and ϕ into a linear combination of simpler, more tractable parts. Just as we need a linear combination of three orthogonal directions to uniquely describe the net direction of a vector in space, we use a linear combination of spherical harmonic functions to uniquely describe the shape of our geomagnetic potential, $\psi(r, \theta, \phi)$. The spherical harmonics are all mutually orthogonal on a spherical surface.

The amplitude, c_l^m or equivalently g_l^m and h_l^m, of each spherical harmonic is called a Gauss coefficient and plays an analogous role to the amplitude of each sinusoidal term in a Fourier series decomposition for an analogous function of one independent variable. Each spherical harmonic is identified by its degree and order pair, (l, m), where $m \in [-l, +l]$. This is analogous to how each sinusoid in a Fourier series is identified by its unique integer frequency.

We use the real Gauss coefficients g_l^m and h_l^m to describe the geomagnetic field. They are estimated from comparisons between spherical harmonic models and data. Equation 1.1 tells us that the magnetic field is the gradient of the geomagnetic potential so each directional component of $\vec{B}(r, \theta, \phi)$ can also be written as a spherical harmonic series by taking the appropriate derivative of $\psi(r, \theta, \phi)$.

After doing so, we can compare the field components predicted by the model with actual field observations made at specific locations on Earth's surface, (a, θ, ϕ), where a is Earth's radius. Changing ∞ to an arbitrary l_{max} in Equation 1.3 and recasting the equation into matrix form, we apply least squares or regularized inversion to estimate the first several Gauss coefficients $\{g_l^m, h_l^m\}$ that describe the geomagnetic field.

Our understanding of the geomagnetic field has been significantly improved by plotting spherical harmonics' relative contributions to the total field as a function of degree l and comparing which has more and less influence. The Lowes spatial spectrum

$$R_l = (l+1)\left(\frac{a}{r}\right)^{2l+4} \sum_{m=0}^{l} \left((g_l^m)^2 + (h_l^m)^2\right) \tag{1.7}$$

reflects the energy contribution of each spherical harmonic degree to the total signal [Hulot et al., 2011]. R_l is actually derived as the average squared field strength over a surface radius r. The Lowes spectrum for geomagnetic field data pertaining to a time-varying global field model, which we will discuss later on, is plotted in Figure 1.3. By plotting the Lowes spectrum, studies have consistently shown that the dipole field, corresponding to $l = 1$, dominates the geomagnetic field [Backus et al., 1996]. A description of the dipole field can thus be considered an analysis of the total geomagnetic field, to first approximation.

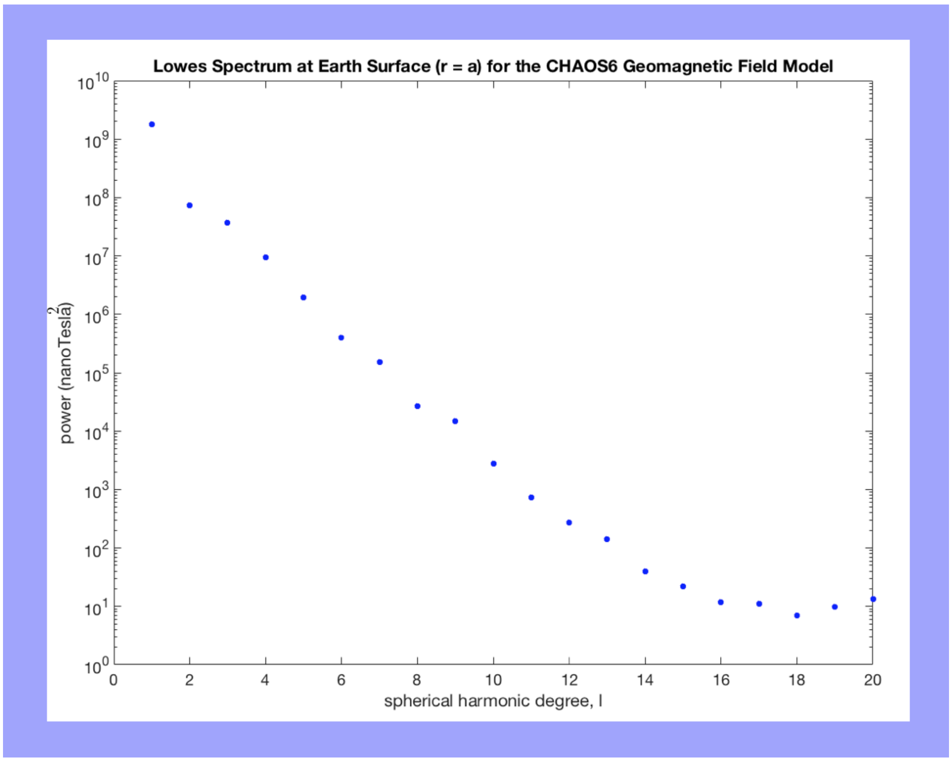

Figure 1.3: The Lowes spectrum for geomagnetic field model CHAOS6 [Finlay et al., 2016]. CHAOS6 incorporates field measurements via SWARM satellites and ground observatories.

Earth's dipole field consists of contributions from spherical harmonic orders

$m = \{0, 1, -1\}$. The three m values each correspond to a dipolar field with its central axis oriented in one of three Cartesian directions as indicated in Figure 1.6 [Backus et al., 1996]. It is well-known that today the axis of the dipole field is offset from Earth's geographic axis by 11°. Yet measurements of the geomagnetic field have shown that the dipole tilt wobbles around Earth's rotational axis and so averages to a 0° tilt across time. We thus deduce that the spherical harmonic with the strongest energy contribution and the most temporal variability in the total geomagnetic field is the axial dipole with its axis oriented along the rotation axis of the Earth. This assumption that field measurements at Earth's surface approximately reflect a purely g_1^0 field is called the geocentric axial dipole approximation (GAD).

The axial dipole field strength is given by the Gauss coefficient $g_1^0(t)$ and is directly related to a vector quantity called the axial dipole moment, $\varphi(t)$, via

$$g_1^0(t) = \frac{\mu_0 \varphi(t)}{4\pi a^3}. \tag{1.8}$$

μ_0 is the magnetic permeability in a vacuum and a is Earth's radius [Backus et al., 1996]. Since the axial dipole field contribution seems to dominate the time-varying geomagnetic field, temporal variations in the geomagnetic axial dipole moment serve as a useful proxy for variations in the total geomagnetic field. We discuss the GAD and other similar approximations later.

1.3 Measurements of the Field

1.3.1 Data Types

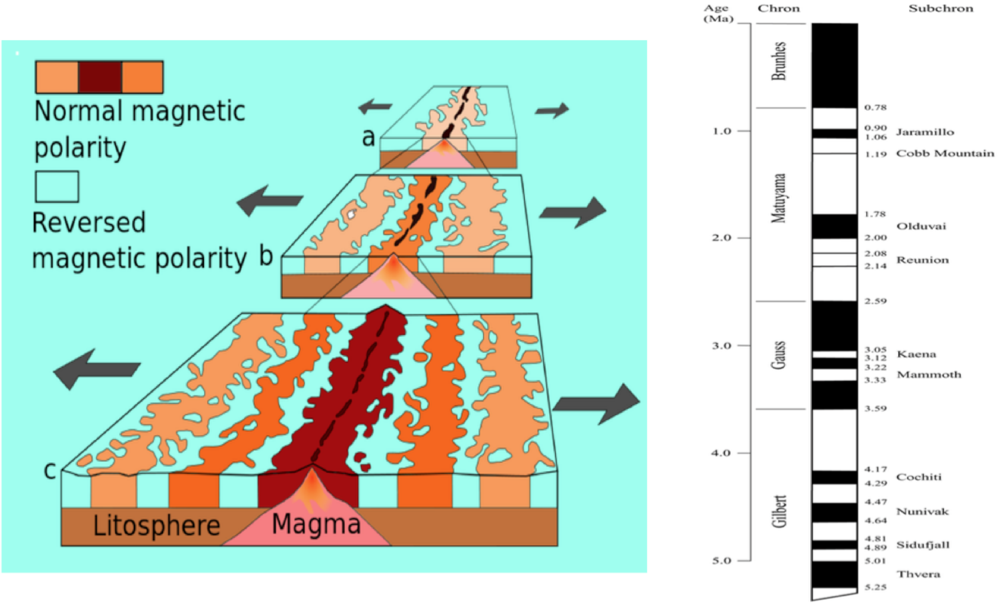

Figure 1.4: Geomagnetic reversals are recorded by the spreading sea floor. a), b) and c) depict the sea floor 6 million years ago, 3 million years ago, and in the present day, respectively. Not shown here, a geomagnetic excursion is when the geomagnetic dipole moment shrinks to near-zero, hinting at a possible reversal, but then grows back to its original polarity without reversing and then stabilizing in the opposite polarity. It is speculated that excursions and reversals are driven by the same geodynamo mechanism.

Various types of field data record the field on various timescales. Million-year changes in the geomagnetic field are observed in the magnetostratigraphic record and marine magnetic anomalies at the ocean floor. After erupting out of a mid-ocean ridge, each new “stripe” of magma cools, becomes magnetized parallel to the ambient field, and is rafted away from the ridge. Stripes further from the ridge are older and carry a remanent magnetization parallel to the ambient field from a longer time ago. The sequence of cooled magma strips hence records local field variations over time and can capture field reversals when they occur. This phenomenon results in magnetic stripes on the seafloor that are associated with lineated marine magnetic anomalies measured at the sea surface, as illustrated in Figure 1.4.

For the ancient field, we rely predominantly on sedimentary, archeological, and igneous data [Tauxe, 2010]. As magnetic lake and ocean sediments sink, settle and eventually compact, the magnetic particles acquire a net (small) preferential alignment parallel to the ambient geomagnetic field as the sediment is lithified. This process is subject to more physical and chemical perturbations than the remanence acquisition process of igneous rock and archeological artifacts (like pottery). The latter are originally heated by the Earth or in a kiln, and acquire a thermal remanent magnetization as they cool through their Curie temperature. Like each magnetic stripe on the moving ocean floor, each archeological or igneous sample captures a time-snapshot of the ambient field. Meanwhile, the sequence of stripes along the seafloor and sedimentary media both record time series of field variations.

At more recent times, the historical field record, which bridges the gap from 1590 to 1980 C.E., comes from ship logs during the Age of Exploration [Jackson et al., 2000]. In 2000 C.E., Jackson et al. compiled all of these data and constructed a time-varying spherical harmonic model for the historical field. The Gauss coefficients in Equation 1.3 were treated as functions of time and the resulting spherical harmonic model was fit to data. Jackson et al. (2000) called the resulting model GUFM1.

Finally, ground observatories and satellites have mapped the modern field since 1980 C.E. to increasing spatial and temporal accuracy. The Lowes spectrum in Figure 1.3 corresponds to the average Gauss coefficients that were fit to SWARM satellite data during 2015 C.E. [Finlay et al., 2016]. A spherical harmonic description of all available modern field data is maintained currently and is called the International Geomagnetic Reference Field (IGRF). We detail how to construct time-varying global field models later.

1.3.2 Coordinate Systems

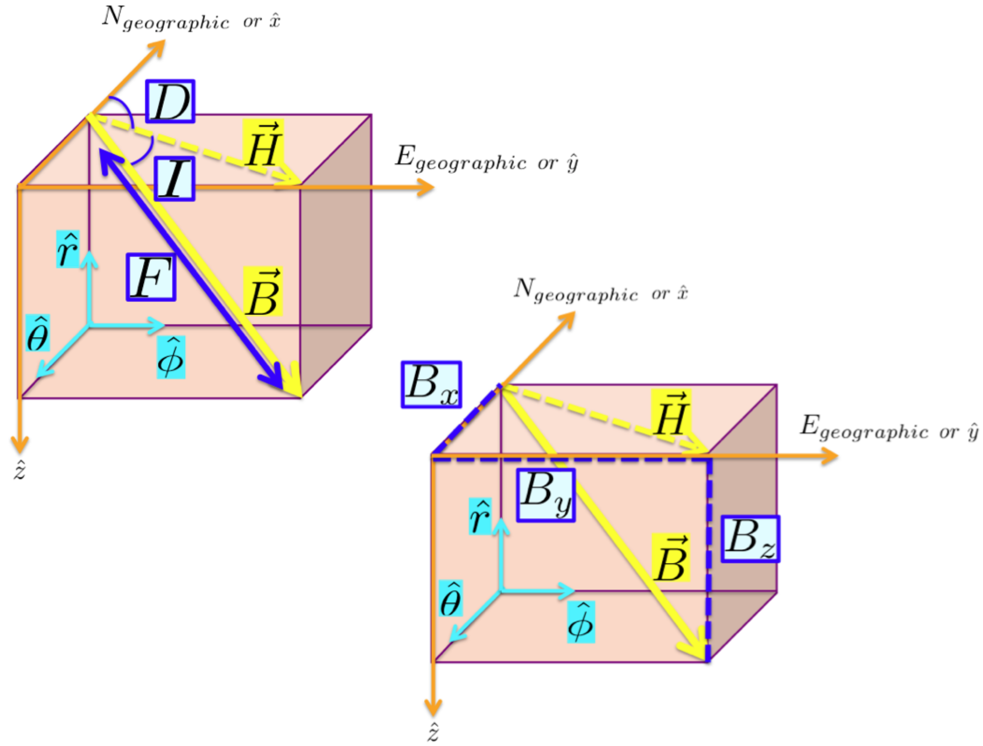

Figure 1.5: $\vec{B}$ (solid yellow) can be decomposed into (B_x, B_y, B_z), in local Cartesian coordinates, or can be represented by (I,D,F) - both in dark blue. The global spherical coordinate system with origin at Earth's center is shown in light blue, and when Earth is assumed to be perfectly spherical the local Cartesian coordinate system maps onto the global system by $\hat{x} \rightarrow -\hat{\theta}$, $\hat{y} \rightarrow \hat{\phi}$, $\hat{z} \rightarrow -\hat{r}$.

The field is measured as either

$$\text{I} = \text{inclination}$$

$$\text{D} = \text{declination}$$

$$\text{F} = \text{intensity}$$

or

$$B_x = \text{northward field component}$$
$$B_y = \text{eastward field component}$$
$$B_z = \text{downward field component}$$

at various geographic locations [Tauxe, 2010]. This is illustrated in Figure 1.5. Intensity (F) is the magnitude (i.e. strength) of the local geomagnetic field $\vec{B}$. Inclination (I) is the angle between the local horizontal and the local field. H in the diagram is the horizontal intensity of the local field, or the component of the field vector parallel with the local horizontal. Declination (D) is the angle between $\vec{H}$, which points toward geomagnetic north, and geographic north.

Earth is a little ellipsoidal so (I, D, F) or (B_x, B_y, B_z) are assumed to be measured relative to an oblate Earth. If we assume instead that the Earth is approximately spherical, we replace the term "geographic" with "geocentric" and automatically have that

$$B_r = -B_z$$
$$B_\theta = -B_x$$
$$B_\phi = B_y$$

or

$$B_r = F\sin(I)$$
$$B_\theta = F\cos(I)\cos(D)$$
$$B_\phi = F\cos(I)\sin(D).$$

where (r, θ, ϕ) are still the spherical coordinates with respect to an origin at the spherical Earth's center.

1.3.3 Spatial Structure

Knowing that the geomagnetic field is dominantly dipolar allows us to analyze the consequences of assuming that our field measurements come from a purely dipolar source. Suppose that we measure a (I, D, F) at a site. Our measurement is easily converted into $(B_r, B_\theta, B_\phi) = \vec{B}$ assuming Earth is spherical. Next, suppose that our measurements are a part of a purely-dipolar field. Note that we do not mean a GAD field; we suppose all three $l = 1$ terms are present and their net effect is a field with its central axis oriented differently from the geographic poles. This concept is illustrated in Figure 1.6.

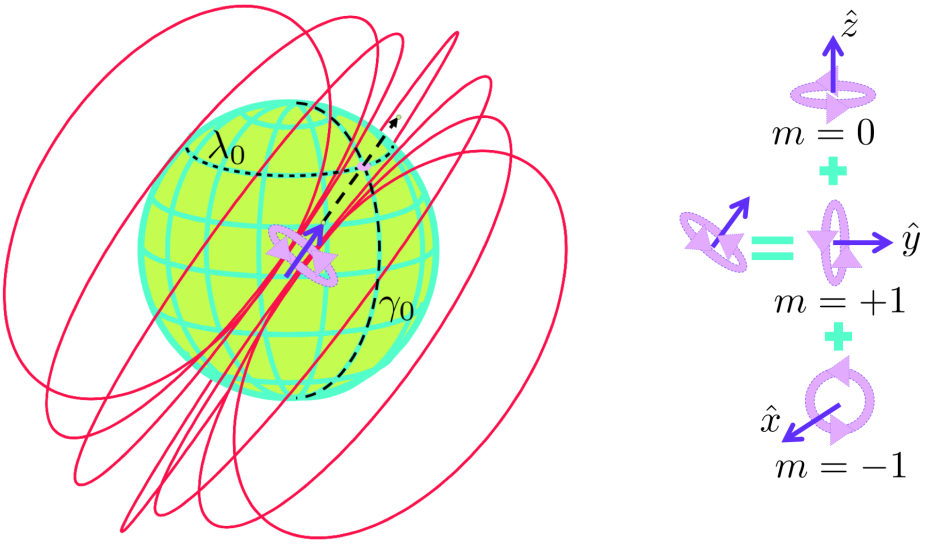

Figure 1.6: A dipolar field with $\{g_1^0, g_1^{-1}, g_1^1\}$ spherical harmonic components is drawn with central axis offset from the geographic pole (modern-day field offset is 11°). The virtual geographic pole (VGP), at which the extension of the geocentric dipole pokes through Earth's surface, is given by λ_0 and γ_0. The lilac rings are hypothetical current sources that would give rise to each dipole orientation.

Using the definition of a dipole magnetic field and spherical coordinate trigonometry, we compute the direction and magnitude of a geocentric dipole whose field would give rise to our local measurement at Earth's surface. The geocentric dipole, illustrated in Figure 1.6 as a purple vector at Earth's center, dictates the strength and orientation of the dipolar field. If we extend the dipole until it pierces through Earth's surface, the point where it pokes through is called the virtual geomagnetic pole (VGP). We refer to the latitude and longitude of the VGP by λ_0 and γ_0, respectively and label them in Figure 1.6. The magnitude of the geocentric dipole is called the virtual dipole moment (VDM).

If we instead suppose that our measurements are a part of a GAD field, then the VGP will poke through at the North or South pole depending on the field's polarity and the magnitude of the GAD vector is called the VADM, for virtual axial dipole moment. Certain studies prefer to assume a purely dipolar, rather than GAD, field because it is one less assumption.

With a single field measurement (I, D, F) we can estimate a corresponding $(\lambda_0, \gamma_0, \text{VDM})$. So with a sequence of (I, D, F) measurements from various geographic locations we can estimate a corresponding sequence of $(\lambda_0, \gamma_0, \text{VDM})$. This helps to determine what Gauss coefficients will produce spherical harmonic models that exhibit spatial structures similar to those observed in the geomagnetic field. As usual, a spherical harmonic expansion according to Equation 1.3 is written for the geomagnetic field up to a chosen l_{max}. Theoretical expressions for (I,D,F) at any point on Earth's surface, (a, θ, ϕ), are derived. Since actual field measurements are not made at every location on Earth's surface, the (I, D, F) predicted by the model are computed at each (θ, ϕ) pair pertaining to each observation site.

Comparisons between the model and data (I,D,F) can be made or we can advance one step further. Theoretical expressions for $(\lambda_0, \gamma_0, \mathrm{VDM})$ corresponding to (I,D,F) at any surface location (a, θ, ϕ) can be derived. The $(\lambda_0, \gamma_0, \mathrm{VDM})$ corresponding to each actual observation is also computed. Then theoretical and observed curves of λ_0, γ_0 or VDM as functions of colatitude θ or longitude ϕ are compared. In the next few sections we discuss several instances where this approach facilitated the development of spatially complex, statistical field models.

1.4 Time Variations in the Geomagnetic Field - Statistical Descriptions

1.4.1 Sources of Uncertainty in Measurements and Simulations

Variations in the total and dipole field occur on a variety of timescales. Changes in the length of day have been tied to decadal field variations and torsional oscillations in the outer core [Buffett et al., 2009]. The rock record shows long polarity intervals, with some cases lasting over millions of years. Asymmetric rates of axial dipole growth and decay have been identified in paleomagnetic and marine data and are speculated to reflect coupled diffusion and advection in the outer core [Avery et al., 2017].

A deterministic process can be described by observing the physical system and applying the mandatory conservation laws for mass, momentum, and energy. It would be ideal to develop a deterministic description of the fluid behavior in Earth's outer core and then compute the resulting geomagnetic field. Unfortunately, we have no way of directly observing the outer core. We can simulate the outer core by time-stepping through the three conservation laws for fluid motion, Ohm's law, and Maxwell's equations. Together these are called the magnetohydrodynamic equations and they are non-dimensionalized before we time-step through them. This means that the parameters of the equations we ultimately use are non-dimensional ratios that weigh relative influences between different physical properties on the total core flow. Table 1.1 lists parameters that contribute to the non-dimensional magnetohydrodynamic equations.

Table 1.1: Dimensionless magnetohydrodynamic parameters.

Name	Symbol	Definition	Physical Ratio
Rayleigh Number	Ra	$\frac{g\alpha\Delta T L^3}{\kappa\nu}$	$\frac{\text{buoyant force}}{\text{(viscous force)}\cdot\text{(heat diffusion rate)}}$
Reynolds Number	Re	$\frac{UL}{\nu}$	$\frac{\text{inertial force}}{\text{viscous force}}$ (laminar flow)
Magnetic Reynolds Number	Rm	$\frac{UL}{\eta}$	$\frac{\text{fluid advection}}{\text{magnetic (Ohmic) diffusion}}$
Prandtl Number	Pr	$\frac{\nu}{\kappa}$	$\frac{\text{kinematic viscosity}}{\text{thermal diffusivity}}$
Magnetic Prandtl Number	Pm	$\frac{\nu}{\eta}$	$\frac{\text{kinematic viscosity}}{\text{magnetic diffusivity}}$
Rossby Number	Ro	$\frac{U}{2\Omega L}$	$\frac{\text{inertial force}}{\text{Coriolis force}}$
Ekman Number	Ek	$\frac{\nu}{2\Omega L^2}$	$\frac{\text{viscous force}}{\text{Coriolis force}}$
Taylor Number	Ta	$\left(\frac{2\Omega L^2}{\nu}\right)^2$	$\frac{\text{inertial force}}{\text{viscous force}}$ (rotational flow)
Hartmann Number	Ha	$\frac{BL}{\sqrt{\nu\rho\eta}}$	$\frac{\text{Lorentz force}}{\text{viscous force}}$
Elsasser Number	Γ	$\frac{B^2}{\eta\rho\Omega}$	$\frac{\text{Lorentz force}}{\text{Coriolis force}}$

Unfortunately, numerical dynamo simulations do not reach the region of parameter space that would accurately describe Earth's outer core, assuming that we know the parameter values for Earth in the first place. For example, the actual geodynamo is predicted to operate at a tiny Ekman number and a huge Hartmann number that correspond to extremely low fluid viscosity and thus lots of turbulence. Computers have difficulty time stepping at a high enough rate to capture all of this turbulence at a small enough spatial scale while also successfully capturing long-term trends in field behavior, so geodynamo simulations are built at higher Ekman numbers and lower Hartmann numbers that computers can handle.

Because we simulate the geodynamo with parameters that do not necessarily represent the Earth, we often find that our assumed values warp the simulated magnetic field so it becomes difficult to translate the simulation back to real-world units. For instance, using a larger-than-reality Ekman number implies either a change in the viscosity of the fluid or a change in Earth's rotation rate - it is ambiguous which has occurred. So when we try to assign a real-world timescale to each timestep in the simulation, we have a choice between timescales - one that assumes the large Ekman number is due to a change in outer-core viscosity and one that assumes it is due to a change in Earth's rotation rate.

Whether the simulation is trying capture flow dynamics at the core-mantle boundary (CMB) or flow dynamics in the whole core can drastically change the timescale used. The slip of fluid against solid mantle at the CMB plays a role in Ohmic diffusion (diffusion of magnetic energy out of the outer core), which operates on 10^4 year timescales while the turbulence that occurs in main body of the outer core regulates advection, which occurs on 10^1 year timescales [Jackson and Finlay, 2015].

Meanwhile, the actual geodynamo is predicted to operate at a huge Hartmann number that corresponds to extremely low fluid viscosity. Again to accommodate limited computational power, geodynamo simulations are built at lower Hartmann numbers that computers can handle and eventually it becomes unclear what units should be used to scale the simulated field strength. The morphology of the global simulated field and frequencies that appear to be present in a simulation depend on which time and field strength scalings are used. So when we compare a simulated geomagnetic field with the measured field, it becomes difficult to tell whether the simulation is truly "Earthlike" and mimics the real geodynamo or if it just *seems* Earthlike because of the arbitrary scaling units that were applied.

In an ideal world, the GUFM1 model would be extended to longer timescales reflecting the underlying geodynamo process; however there are limitations in the available paleomagnetic data. It is also impossible to collect time series of paleomagnetic observations with roughly equal spacing in time and with consistent resolution on the geological timscales of interest. Igneous rocks act as magnetometers by acquiring a thermal remanent magnetization as they cool, while ocean and lake sediments acquire a detrital remanent magnetization as magnetic grains in the sediments preferentially align with the local field [Tauxe, 2010]. Sedimentary cores drilled out of ocean and lake floors may provide time series of the local field, but different sites with varying sedimentation rates exhibit secular variation with varying amounts of temporal smoothing. The geological processes producing sedimentary magnetization cannot be replicated in the lab, so each intensity measurement made at a section along the core is understood only relative to the measurement made at the previous section, while the detrital remanence of the entire core could be warped by physical and chemical changes in the local environment.

In fact, the relative measurements from sedimentary data are calibrated with respect to absolute measurements taken from lava flows or archeomagnetic data. The latter are absolute measurements because the acquisition of thermal remanent magnetization is not nearly as susceptible to environmental perturbations and thus can be approximately replicated in the lab. Unfortunately, the exact timing of lava flows (i.e. when they cooled) is generally unknown (with historical exceptions); at each observation site we sample many flows in an attempt to capture as much secular variation as we can across a sufficiently long time interval between the oldest and youngest flows at the site [Constable and Johnson, 1999]. Lava flow and archaeological sites are unevenly geographically and temporally distributed, which contributes to another source of uncertainty in our conclusions about the global field at any time.

1.4.2 JC95 - A Time-Averaged Field

All of the above hinder the development of a deterministic model for the geomagnetic field based on clear and reliable data. However, the variety of data across both space and time do facilitate a statistical approach, in which we observe spatial structures in the time-averaged geomagnetic field. Capitalizing on this approach, Johnson and Constable (1995) developed inverse models using lava flow data spanning 0-5 Ma to better understand the robustness of spatial features we see in the geomagnetic field [Johnson and Constable, 1995]. Johnson and Constable (1995) began by averaging their {I,D} measurements within small spatial bins confined within adjacent latitudes and longitudes. This revealed that the difference between the means and the {I,D} that would result at the center of each spatial bin from a GAD model, is a function of longitude. Johnson and Constable (1995) also obtained that the aforementioned difference is not identical when the data averaged together are selected from normal polarity versus reverse polarity epochs. We call the latter an instance of "normal versus reverse polarity asymmetry".

Johnson and Constable (1995) employ the Kolmogorov Smirnov (KS) test to determine whether the properties of the normal and reverse polarity epochs visible in the data are statistically similar. The KS test essentially yields a parameter that tells whether two different datasets come from the same, underlying probability density distribution. Johnson and Constable (1995) computed that the VGP distributions of the normal and reverse polarity data were different, giving another piece of evidence for normal versus reverse polarity asymmetry.

Johnson and Constable (1995) then applied regularized inversion to generate new models for the time-averaged paleofield across all of the normal polarity data and across all of the reverse polarity data, separately. From their models, the authors showed that the power in the Lowes spectrum at degree-$l \leq 2$ Gauss coefficients looks *totally* different between the normal and reverse polarity data, yet another sign of normal versus reverse polarity asymmetry. Furthermore, the RMS misfit between the normal polarity model and the reverse polarity model was high, indicating that normal and reverse polarity morphologies are probably different.

Johnson and Constable (1995) mention that this asymmetry is a conundrum because the magnetic induction equation the governs the behavior of the geodynamo does not allow for this asymmetry; letting $\vec{B} \rightarrow -\vec{B}$ in the equation changes nothing. Finally, the authors note that the appearance of certain field structures in the models depended heavily on certain subsets of the data and disappeared when those data were not included in the inversion.

We take this to mean that field structures that appear in data must be assessed as robust before developing field models that reflect those structures because some structures disappear suddenly when we eliminate a single dataset. As suggested by Johnson and Constable (1995), perhaps it would be wise to determine which datasets have significant impact on the overall model and then eliminate these to yield a model that is the lower bound on field complexity.

1.4.3 Time Variations as a Probability Density Function

If we assume that the field evolves through time in a totally random fashion, then we are assuming that the probability of the field exhibiting a certain behavior in the present does not depend on what it did in its past. Such a process is referred to as "uncorrelated" or "white" noise. It is often assumed that white noise is described by a Gaussian probability density function,

$$P(y) = \frac{1}{\sqrt{\sigma^2 2\pi}} e^{-\frac{(y-\mu)^2}{2\sigma^2}} \tag{1.9}$$

where μ is the mean and σ^2 is the variance of the white noise $y(t)$. In 1.9 the white noise is a scalar-valued process, but the geomagnetic field is a vector-valued process. So we treat the field $\vec{B}$ as a random vector variable whose probability density distribution can be characterized by the time-averaged paleofield and its variance from that mean [Constable and Johnson, 1999]. [1]

A white noise representation for the geomagnetic field provides a useful logical seed, yet no natural process can be totally random. Also, the dependence of the current state of a system on previous states tends to decrease as we compare further into the past. Each second that a tossed ball falls, for instance,

---

[1] Essentially this means that the strength and each directional component of the field will have its own probability density distribution.

the instantaneous velocity of the ball is highly dependent on the velocity a second earlier (in this case by the negative acceleration) but far less dependent on the velocity three minutes ago. This leads to the concept of autocovariance, which is a curve that tells us the similarity between the current state of a system to its past states, with respect to increasing “lag time” τ by which we make the comparison into the past. A process that depends on its past is said to be “correlated” or “red” noise. The autocovariance of time-varying process $y(t)$ is defined as

$$R_y(\tau) \equiv < y(t-\tau)y(t) > \tag{1.10}$$

where the brackets indicate that we are taking the expectation value (i.e. average). When using this formula we are assuming that $y(t)$ is a zero-mean process. A procedure for calculating $R_y(\tau)$ is illustrated in Figure 1.7.

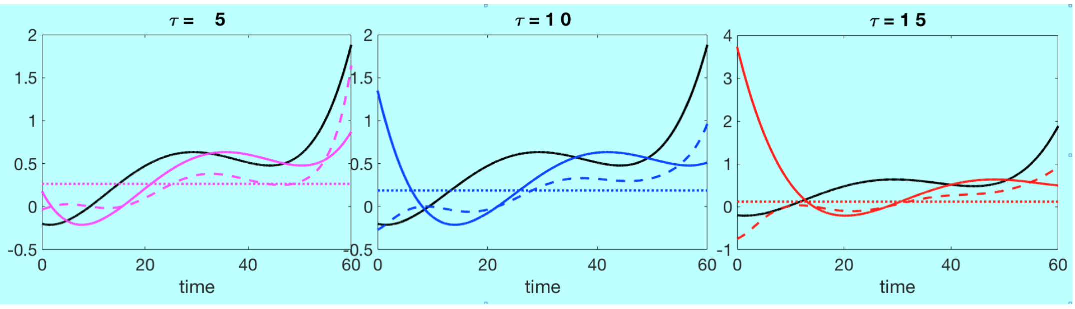

Figure 1.7: Take $y(t)$ (solid black) and shift it to the right by a chosen lag time, τ, to get $y(t-\tau)$ (solid color). Multiply the original and the shifted curves to get a product curve (dashed color) and take the average value of the product (dotted color). The latter is the autocovariance of $y(t)$ at τ. We compute the autocovariance for a continuous domain of lag times and thus obtain $R_y(\tau)$ for a continuous domain of τ values.

Our scenario with the ball-toss is an example of a deterministic process, but the concept of autocovariance is applicable to all natural processes. It is often helpful to first treat geomagnetic field variations as white noise and then observe what happens when we propose an analytic form for its autocovariance function. The most common form proposed is exponential decay, like

$$R_y(\tau) = \beta e^{-\frac{\tau}{\tau_0}} \tag{1.11}$$

where τ_0 is the "memory timescale" of the process that dictates how slowly a system forgets its past.

1.4.4 Giant Gaussian Processes

Regardless of whether the geomagnetic field evolves as a correlated or uncorrelated process, it experiences variations in its strength and direction with respect to time. This indicates that the Gauss coefficients, which dictate the spherical harmonic makeup of the field, are functions of time. Perhaps the most apparent evidence of this is that field morphology changes dramatically as reversals occur [2], indicating that the spherical harmonic composition of the field is dynamic during the reversal. Hence we should treat not only $\vec{B}$ as a whole, but also the individual Gauss coefficients $\{g_l^m(t), h_l^m(t)\}$, as random variables with each their own probability density distribution. This idea provided incentive for the development of the original Giant Gaussian Process [Constable and Parker, 1988].

---

[2] Precisely how the morphology changes is debated; most scientists say that the dipole moment shrinks to zero and then emerges with the opposite polarity because paleointensity records through excursions and reversals all show decreases in intensity.

An uncorrelated stochastic process - CP88

Constable and Parker (1988) developed the first Giant Gaussian Process (GGP) model. Taking into account both the anomalously high power of the $l = 1$ term in the Lowes spectrum of MAGSAT satellite data and the large value for the strength of the axial dipole field, g_1^0, in the data relative to its non-axial counterparts, $\{g_1^1, h_1^1\}$, Constable and Parker (1988) concluded that the total field is dominated by an axial dipole contribution. To model the temporal evolution of the field in a way that did not require too much detail, Constable and Parker (1988) then decided to let each Gauss coefficient be Gaussian-distributed random noise, with mean and variance selected from the MAGSAT data. Each Gauss coefficient of degree-l except the axial dipole, $g_1^0(t)$, was defined to have 0 mean and variance

$$\sigma_l^2 = \frac{\bar{R}_l}{(2l+1)(l+1)} \tag{1.12}$$

where the numerator

$$\bar{R}_l = \left(\frac{c}{a}\right)^{2l} \alpha^2 \tag{1.13}$$

is the average value of the Lowes spectrum for the MAGSAT data. To indicate its uniqueness, the axial dipole was given a mean value of

$$\bar{g}_1^0 = 30\mu T \tag{1.14}$$

to match the average value of the MAGSAT data.

Constable and Parker (1988) simulated a statistical distribution for the field by generating a sequence of random deviates for each Gauss coefficient, drawing repeatedly from each respective Gaussian distribution. There was no temporal autocovariance in this simulation, i.e. each Gauss coefficient was treated like a process with no memory of the previous field. The authors compared the simulated field to paleomagnetic data from a global compilation by Lee (1983). This data set spans 0-5 Ma and contains 20 polarity reversals. If they neglected the short intervals during which the paleofield was reversing, Constable and Parker (1988) essentially had a large collection of empirical realizations for both the normal and reverse polarity field to which they could compare their model.

Constable and Parker (1988) showed that the paleomagnetic observations contained latitudinally-dependent features. The Lee (1983) data had 19 stable polarity intervals. All of the normal-polarity data were grouped together and the same was done for all of the reverse-polarity data. Because of a lack of data to indicate otherwise, Constable and Parker (1988) assumed that the field intrinsically has the same statistical behavior regardless of polarity. Hence they flipped the sign of all of the reverse polarity data and then assimilated it into the normal polarity data, producing one dataset presumed to reflect *either* stable polarity behavior.

Constable and Parker (1988) next partitioned the observations sites for each value in the giant dataset into latitude bands. Then they computed the mean and standard deviation across all of the data within each latitude band. This produced a sequence of mean values and a sequence of standard deviation values for both inclination and declination, corresponding to the sequence of latitude bands. Allowing each band to be represented by the latitude at its center, the authors thus obtained a sequence for each variable in $\{\bar{I}, \bar{D}, \sigma_I, \sigma_D\}$ as a function of latitude. A smooth curve was produced to see the general trend of each variable with respect to latitude.

To compare their model with paleomagnetic data, Constable and Parker (1988) derived the theoretical distributions of inclinations and declinations that would result at any point on Earth's surface, from their simulated field. The average and standard deviation in inclination across all longitudes and time was computed. This same process was repeated for declination, ultimately yielding $\{\bar{I}, \bar{D}, \sigma_I, \sigma_D\}$ at each latitude. Fitting a best fit curve to the sequence values taken on by each variable with respect to latitude, the authors compared this curve to the one determined from the data of Lee (1983). They discovered that the two curves did not match. After some experimentation, Constable and Parker (1988) deduced that the best way to model these features was by lowering σ_1 by half and raising the mean axial quadrupole to

$$\bar{g}_2^0 = 0.06\bar{g}_1^0, \tag{1.15}$$

respectively. Once implemented, these modifications were used to generate a new field simulation and curves for $\{\bar{I}, \bar{D}, \sigma_I, \sigma_D\}$ with respect to latitude. The curves roughly matched those exhibited by the paleomagnetic data. We note that this model, which we call CP88 from now on, was based on MAGSAT data of the modern field and was subsequently modified to accommodate latitude-dependent features of the 0-5 Ma paleomagnetic data. CP88 was not built with any memory of its past; we now explore a model that successfully predicted observed behaviors of the geomagnetic field during a reversal because it described each Gauss coefficient as correlated red noise.

Adding in temporal correlations for reversals - C90

While CP88 was designed explicitly to model the field during stable polarity intervals, Constable (1990) decided to construct a model for the field during a reversal. Geomagnetic reversals are usually thought to be driven by the axial dipole switching direction. Constable (1990) let the mean axial dipole drive the reversal process as

$$\bar{g}_1^0(t) = e^{-\lambda_1(t-t_s)} - e^{-\lambda_2(t_f-t)} \tag{1.16}$$

where $\{\lambda_1, \lambda_2\}$ dictate the rate of axial dipole decay and regrowth while $\{\tau_s, \tau_f\}$ are the start and end of the reversal.

The author initially defined the variance of the axial dipole field to be Gaussian white noise about this time dependent mean. Meanwhile, the rest of the Gauss coefficients were defined to be Gaussian-distributed random variables with 0 mean like in CP88. Realizations of the first few Gauss coefficients with time as well as the mean axial dipole are plotted in Figure 1.8.

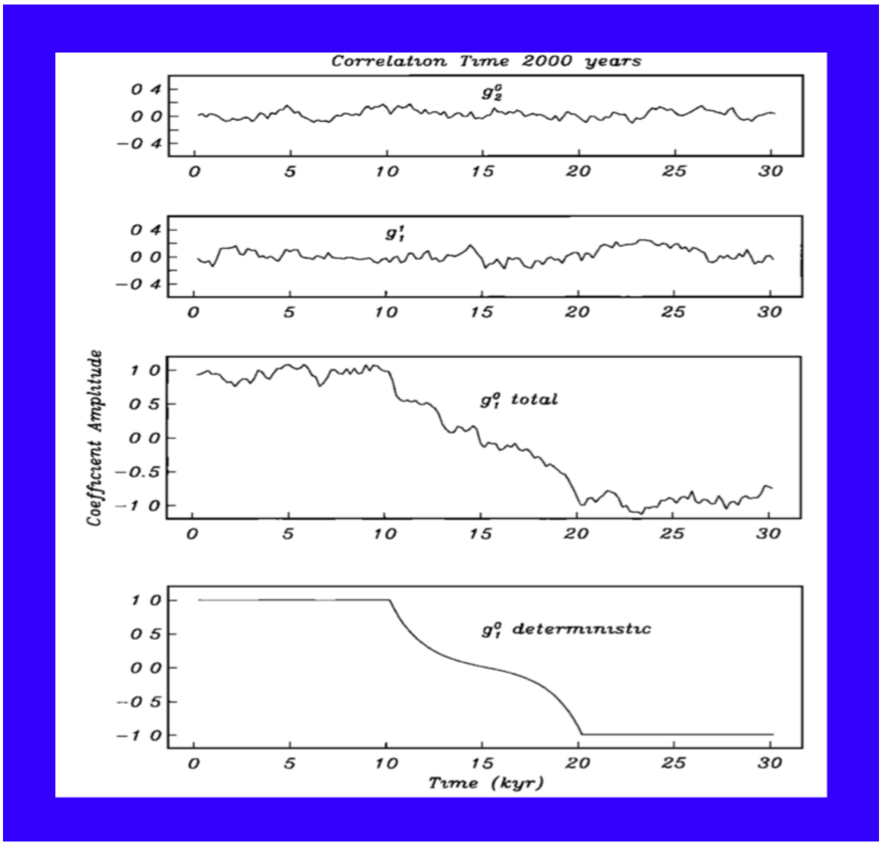

Figure 1.8: Time series for the axial quadrupole (top), non-axial dipole (second), axial dipole (third), and mean axial dipole (bottom) produced by the C90 model [Constable, 1990].

CP88 was built by comparing an initial model based on satellite data to paleomagnetic data and then making appropriate modifications to the model. Taking the same approach, Constable (1990) noticed that the virtual geomagnetic pole (VGP) paths appeared to have a variety of interesting patterns during reversal records. Studies of reversal records have shown the VGP to wander from one pole to another during the reversal, sometimes loitering and looping at the poles and sometimes being longitudinally confined.

In order to generate a GGP model that would exhibit such a variety of VGP paths during a simulated reversal, Constable (1990) modified their initial model to include autocovariance in time, now letting each Gauss coefficient be an order-1 autoregressive (AR1) process described by

$$g_l^m(t) - \bar{g}_l^m(t) = a\Big(g_l^m(t-1) - \bar{g}_l^m(t-1)\Big) + \zeta_t \tag{1.17}$$

where $\bar{g}_l^m(t)$ is the average value of the Gauss coefficient at time t [Constable, 1990]. Constable (1990) still defined $\bar{g}_1^0(t)$ according to the exponential formula while setting $\bar{g}_l^m(t) = 0$ for all of the other Gauss coefficients. a is the autoregressive parameter dictating how dependent the behavior of the Gauss coefficient at time t is, on its behavior at time $t-1$. ζ_t is Gaussian distributed white noise. So in this model, each Gauss coefficient is not a purely random process with respect to time; it is driven by such a process, but has some temporal memory correlating its behavior to its past. We will refer to this model from now on as C90.

The autocorrelation function of the AR1 process is derived to be

$$\rho(r) = a^{|r|} \tag{1.18}$$

where r is a discrete lag time. From this, Constable (1990) showed that if a reversal simulation is chosen to have timestep Δt and τ_c is quantitatively defined to be the time taken for the autocorrelation of $g_1^0(t)$ to drop to 0.1, then

$$a = (0.1)^{\frac{\Delta t}{\tau_c}} \tag{1.19}$$

should be the parameter used in the model to simulate reversals. Constable (1990) simulated three different reversals with autocorrelation times {2000, 4400, 9000} years and the same timestep Δt as shown in Figure 1.9.

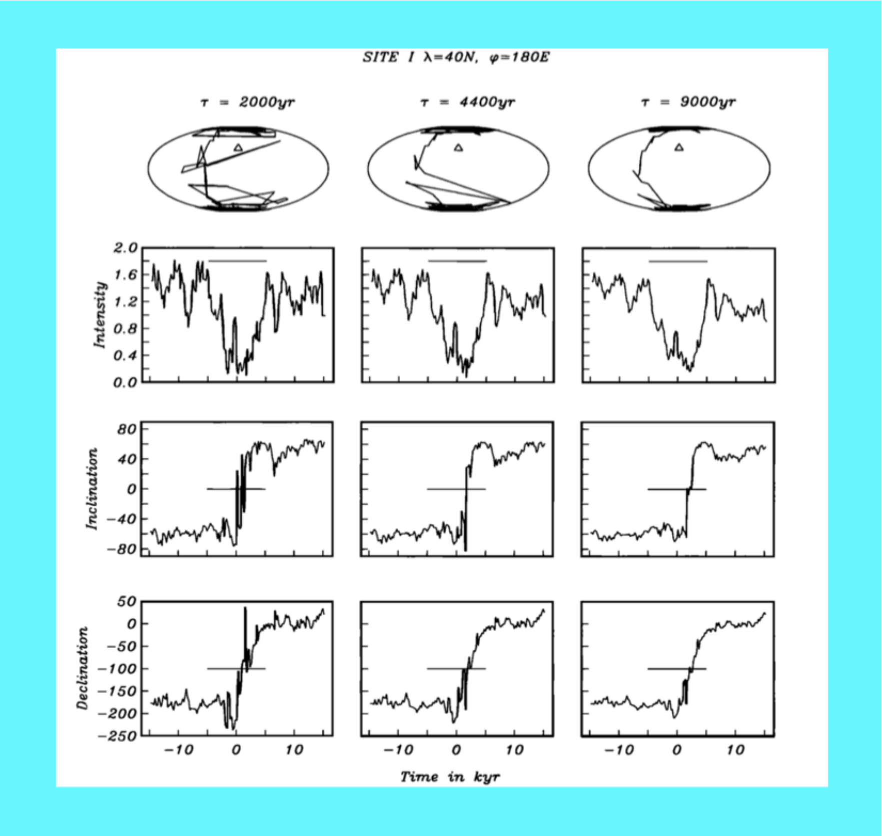

Figure 1.9: Time series of inclination, declination, and intensity during three simulated reversals produced by C90 with corresponding VGP paths (top row) for three different autocorrelation times τ_c. The triangle indicates the site at which these time series would be observed if C90 accurately described the Earth [Constable, 1990].

Constable (1990) computed the VGP path during each model reversal; it was shown that a longer τ_c simulated smooth VGP paths similar to paleomagnetic data that show longitudinal confinement. It was also shown that whether the VGP loops or loiters around the poles is dependent on observer location. Ultimately, Constable (1990) demonstrated that allowing the mean axial dipole to be a deterministic function whose behavior we can predict and treating secular variation as an AR1 process produces a way to model the full range of VGP paths observed in paleomagnetic reversal records.

Improving the spatial representation in CP88 - CJ98 and TK03

The models of Johnson and Constable (1995) demonstrate various time-averaged features that could be used in future GGP modeling. Another feature was addressed by Constable and Johnson (1999), who noticed that CP88 cannot model the variation in VGP dispersion [3] about the geographic axis as a function of latitude correctly [Constable and Johnson, 1999]. This is a sequence of values for standard deviation in VGP, each value corresponding to a subset of data found within a discrete latitude band.

A modification to CP88 made by Quidelleur and Courtillot (1996) fixed this by allowing $\{g_2^1, h_2^1\}$ to have three times the variance as the other $l = 2$ coefficients [Quidelleur and Courtillot, 1996]. We refer to their model as QC96. To test the capacity of QC96 to accurately model another physical parameter, Constable and Johnson (1999) plotted the probability density distribution of all of the paleomagnetic intensity data compiled by Tanaka et al. (1995). Over this, Constable and Johnson (1999) plotted the probability density distribution of paleointensities that would result, at the same observation sites as Tanaka et al. (1995), from a simulation of QC96. Remember the latter series is built by generating a sequence of random deviates for each Gauss coefficient, drawn from its Gaussian distribution afforded by the QC96 model. The variance of paleointensity data is clearly underpredicted by the model.

Similarly, Constable and Johnson (1999) obtained VDM values that correspond to all of the Tanaka et al. (1995) data by calculating the magnitude of the dipole moment at Earth's center that could hypothetically yield each observation, as discussed earlier. Plotting the probability density distribution of all these VDM values, Constable and Johnson (1999) saw that QC96 underpredicts

---

[3] "dispersion" = standard deviation

the spatio-temporal variability in both local field intensity and VDM. To fix the model, Constable and Johnson (1999) raised the variance of the axial dipole in QC96 until the distributions looked right. The new model, which we call CJ98, exhibits the desired variance in VDM and field intensity without impacting directional variability. CJ98 was thus designed to fit the VGP dispersion of the lava flow data compiled by Johnson and Constable (1995) (this was the aim of QC96) and to fit the VDM distribution exhibited by the lava flow data of Tanaka et al. (1995).

We now have a somewhat complex model of the geomagnetic field that can predict its statistical behavior over time while matching spatial properties that are frequently observed in the paleofield. Tauxe and Kent (2004)) give a table of the GGP models discussed so far; this table also includes the model TK03, which we now discuss.

When they were building CP88, Constable and Parker (1988) argued that due to measurement error the variance of the observed {I,D} values at each latitude should be larger than the variance of the {I,D} that would result from CP88 at that latitude. This was the main reason for lowering σ_1 by half. Yet in Constable and Johnson (1999) the variance of the axial dipole is raised specifically in order to get a desired variance in local field intensity and VDM. So the variance of $g_1^0(t)$ in CJ98 is much higher than that of $g_1^1(t)$ and $h_1^1(t)$. Similarly, notice that Quidelleur and Courtillot (1996) raised the variance of $\{g_2^1(t), h_2^1(t)\}$ above that of the other $l = 2$ Gauss coefficients in order to model the VGP dispersion in the paleofield.

Tauxe and Kent (2004) pointed out that in CJ98, several Gauss coefficients with odd $l - m$ seemed to have higher variance than those with even $l - m$ [Tauxe and Kent, 2004]. In spherical harmonic literature the former and latter are called antisymmetric and symmetric Gauss coefficients, respectively. McFadden, Merrill and McElhinny (1988) explained how antisymmetric Gauss coefficients with larger variance cause increased VGP dispersion at high latitudes, which Tauxe and Kent (2004) argued was the reason why CJ98 was successful [McFadden et al., 1988]. Tauxe and Kent (2004) decided that instead of raising σ_2^1 and σ_1^0 relative to $\{\sigma_2^0, \sigma_2^2\}$ and σ_1^1, perhaps it would be wiser to just raise all $\sigma_l^m \quad | \quad l - m =$ odd relative to $\sigma_l^m \quad | \quad l - m =$ even to accomplish the same goals as CJ98.

Tauxe and Kent (2004) let

$$\beta = \frac{\sigma_l^m \quad | \quad l - m = odd}{\sigma_l^m \quad | \quad l - m = even} \tag{1.20}$$

and change the mean value of $g_1^0(t)$ to 15 μT because they believe that the mean value of the 0-5 Ma field is half that of the modern field. Tauxe and Kent (2004) acknowledged that CJ98 was built to describe the field during stable polarity intervals because all of the data whose associated VGP was "too close" to the equator was labeled as indicative of a reversal or excursion, and removed before modeling. Recall that paleomagnetists expect geomagnetic reversals to be marked in their data by a VGP near the equator or a VDM near 0. "Too close" was defined to be at latitudes less than 55°. Hence, the authors pointed out that CJ98 underpredicts VGP dispersion at low latitudes. Meanwhile, the CP88 parameter α obtained from the Lowes spectrum significantly impacts VGP dispersion at equatorial latitudes and β impacts VGP dispersion at high latitudes.

Starting with CP88, Tauxe and Kent (2004) fit α and β to the spherical harmonic decomposition of sedimentary data compiled by Merill and McElhinny (1997) spanning 0-5 Ma. The sedimentary data was averaged across time and the Gauss coefficients that best described the average field were used to compute the new α and β using the same method as in CP88 and as derived above, respectively. These new parameters were then used to define the variances of each Gauss coefficient in the new GGP model, TK03.

A sequence of TK03 realizations was then built by drawing a sequence of random deviates for each Gauss coefficient from its probability density distribution according to TK03. The Lowes spectrum of each realization was plotted; Tauxe and Kent (2004) demonstrated that the modern field poorly represents the 0-5 Ma field by showing the modern field's Lowes spectrum to be an upper bound on the cloud of spectra generated from realizations of TK03. This model also proposed that low-latitude, transitional VGP's are way more likely to be observed at sites near the poles than near the equator. So even if a geomagnetic reversal did occur at some time in the past, whether or not we see it in our data may depend on where our samples were collected.

With the datasets they had at the time, Tauxe and Kent (2004) successfully modeled

1.) VGP dispersion as a function of latitude

2.) VDM spatio-temporal variability

3.) difference in mean inclination as a function of latitude

4.) paleointensity spatio-temporal variability

5.) {I,D} dispersion as a function of latitude

Tauxe and Kent (2004) decided to plot the {I,D} values predicted by TK03 on a stereonet projection because this is a common practice with paleomagnetic data. When they did so, Tauxe and Kent (2004) noticed that the stereonet distribution did not match that of the observed values in some time intervals from Merill and McElhinny (1997), even while the above five characteristics *did* match between TK03 and the data. As a checkpoint, Tauxe and Kent (2004) incorporated sedimentary inclination error into a simple, GAD approximation for the average field and concluded that this reproduces the five traits listed as well as the stereonet distribution of sedimentary data, so perhaps TK03 needs to be re-evaluated. Our understanding of GGP models will evolve as new datasets and paleofield statistics emerge; evidently we must verify that various types of uncertainty in data acquisition do not suffice to describe observations before starting to include spatial complexity beyond a GAD model.

1.4.5 Time-varying Global Field Models

We use the word "model" throughout this paper yet it means something different depending on context. So far, the word "model" has primarily been used when referring to the Giant Gaussian Processes. In that case the word refers to a statistical description of the field, in which each Gauss coefficient is given its own probability density distribution and the parameters of each distribution are extrapolated from actual data. We also mentioned the inversion models of Johnson and Constable (1995) that were built by averaging paleomagnetic data to get a time-averaged paleofield and then computing the Gauss coefficients that describe mean paleofield. These Gauss coefficients are single values estimated directly from the data, not random variables that can take on a range of possible values with probability density distribution defined by parameters estimated from data.

The JC95 models cannot predict the temporal variability of the field and are like a time average of the field. So while the JC95 inversion models were extremely useful when analyzing spatial features of the field they do not provide any predictive insight into future geomagnetic field behavior. In contrast, the GGP models at least offered a statistical description of the future field based on its past behavior. We now mention a third type of "model" that offers deterministic insight into the past field but not the future field. These are called "time-varying global field models". We illustrate the process of building one and then discuss their utility.

Suppose that we want to model just a snapshot of the field at time t_0. The spherical harmonic expansion of the geomagnetic field at t_0 is given by

$$B_i(r,\theta,\phi) = -\nabla_i\left(a\sum_{l=1}^{\infty}\sum_{m=0}^{l}\left(\frac{a}{r}\right)^{l+1} c_l^m(t_0)e^{im\phi}P_l^m\Big(\cos(\theta)\Big)\right) \tag{1.21}$$

where B_i is the ith directional field component, ∇_i is the ith directional derivative in spherical coordinates and $c_l^m(t_0)$ is a complex Gauss coefficient. Suppose also that measurements of the field at that time are made at various (r,θ,ϕ) on Earth's surface. We solve for the Gauss coefficients that best fit the data. Rewriting Equation 1.21 into matrix form, we get

$$\vec{B_i} = \mathbf{S}\cdot\vec{c} \tag{1.22}$$

where everything except the Gauss coefficients have been absorbed into $\mathbf{S}$, $\vec{c}$ is a sequence of all the desired Gauss coefficients, and $\vec{B_i}$ is a sequence of field measurements. This matrix system is solved using inversion techniques [Constable et al., 1987] and outputs the Gauss coefficients. If we have measurements that recorded the field at different times as well as locations, then feeding the data into Equation 1.22 and applying regularized inversion gives us the Gauss coefficients that best describe the structure of time-averaged field captured by our measurements.

Now suppose we want to model the time-varying behavior of the field according to our measurements. We first replace t_0 with t in Equation 1.21. It is usually assumed at this point that each Gauss coefficient is a time-varying process whose variations can be modeled with a polynomial spline. So each Gauss coefficient is a chain of polynomials linked together at successive “knot points”, where each polynomial best describes the variations in the Gauss coefficient within a local time interval. This looks like

$$c_l^m(t) = \sum_{j=1}^{L} \left(a_j^{l,m} t^3 + b_j^{l,m} t^2 + c_j^{l,m} t + d_j^{l,m} \right) \tag{1.23}$$

where the superscript (l,m) indicates that $\{a,b,c,d\}$ describe the time variations of the degree l and order m Gauss coefficient while the subscript j denotes the jth polynomial in the spline for that Gauss coefficient. The jth and the $j+1$th polynomial are forced to have equivalent first and second derivatives at the knot point between them - this ensures that our spline is smooth and does not have abrupt concavity changes. Inserting our spline equation into the spherical harmonic series and rewriting as a matrix system yields

$$\vec{B}_i = \mathbf{T} \cdot \vec{\alpha} \tag{1.24}$$

where $\mathbf{T}$ contains everything except $\{a_j^{l,m}, b_j^{l,m}, c_j^{l,m}, d_j^{l,m}\}$, which are listed in $\vec{\alpha}$. Regularized inversion is again applied to determine the values in $\vec{\alpha}$ that best fit the data, $\{\vec{B}_i\}$. Thus, we obtain a polynomial spline description for the temporal variations of each Gauss coefficient. Putting all of the time-varying Gauss coefficients together produces a time-varying global field model. GUFM1 is an example of such a model, built from historical data. Another such model, called PADM2M, which was built by applying a penalized maximum-likelihood approach to absolute and relative paleointensity data, producing a cubic B-spline representation for $g_1^0(t)$ [Ziegler et al., 2011].

Time-varying global field models do not provide us with a way of telling how the curves of $\{g_l^m(t), h_l^m(t)\}$ will extend into the future. The polynomial splines are not simple, analytic functions with predictable shape and $\{a_j^{l,m}, b_j^{l,m}, c_j^{l,m}, d_j^{l,m}\}$ do not have specific, physical meaning. If we wanted to estimate what the field will look like in the future based on our time-varying global field model we *could* compute the average value and variance of each Gauss coefficient across its interpolation curve and claim that the Gauss coefficient will have that mean and variance in the future - this is essentially how the GGP models were built. Hence, time-varying global field models serve as a reference from which we build and to which we compare statistical descriptions of the field.

1.4.6 Continuous Stochastic Processes

The GGP-based models are good at depicting spatial field variations, yet give obviously limited insight into temporal field behavior where correlations are important [4]. From C90 it is clear that “stochastic” does not mean the deviations of each Gauss coefficient from its mean must be purely random noise; it could mean that the time-varying process has some memory of its own past while

---

[4] Recall that CP88, CJ98 and TK03 assume that the Gauss coefficients are uncorrelated, random processes.

being driven by random noise. C90 gave an especially useful example of how treating the Gauss coefficients as an autoregressive, rather than purely random, process can facilitate modeling of field variations that are clearly visible in the paleofield.

It is prudent to note that the geomagnetic field evolves continuously with time, so it might be better to model the Gauss coefficients as continuously-varying functions of time. We are particularly interested in the axial dipole field contribution, $g_1^0(t)$, as a giant chunk of the observed secular variation is predicted to be driven by $g_1^0(t)$ (reversals, excursions, asymmetric growth and decay). So we want an autoregressive model for the axial dipole field, or possibly the axial dipole moment, that is continuous with time. A theoretical framework for describing continuous autoregressive processes was first developed to study Brownian motion (e.g. [Brockwell, 2001]). Within this framework, an autoregressive process is described by a differential equation of the desired order that is driven by white noise just as in the discrete treatment. We can rewrite the order-m discrete autoregressive series employed by C90 as

$$\varphi'_t = a_1\varphi'_{t-1} + a_2\varphi'_{t-2} + \ldots + a_m\varphi'_{t-m} + \zeta_t \tag{1.25}$$

$$\rightarrow a_0\varphi'_t + a_1\varphi'_{t-1} + a_2\varphi'_{t-2} + \ldots + a_m\varphi'_{t-m} = \zeta_t \tag{1.26}$$

where we suppose that φ'_t is the deviation of axial dipole moment about its mean, ζ_t is a Gaussian-distributed white noise process, and $a_0 = 1$ and $\{a_1, \ldots, a_m\}$ are unknown constants so their sign just got absorbed in the second line. [5] Whereas in the discrete timestep regime our autoregressive model has

---

[5] From now on, we use $g_1^0(t)$ to signify the strength of the axial dipole field and φ_t to signify the axial dipole moment.

the finite-difference operator $D^i\varphi'_t = \varphi'_{t-i}$,

$$\rightarrow a_0D^0\varphi'_t + a_1D^1\varphi'_t + a_2D^2\varphi'_t + \ldots + a_mD^m\varphi'_t = \zeta_t \tag{1.27}$$

$$\rightarrow \sum_{i=0}^{m} a_iD^i\varphi'_t \quad \Big| \quad D^i\varphi'_t = \varphi'_{t-i} \tag{1.28}$$

in a continuous time regime our autoregressive model has the differential operator $d^i\varphi'(t) = \frac{d^i\varphi'}{dt^i}$,

$$a_m\frac{d^m\varphi'}{dt^m} + a_{m-1}\frac{d^{m-1}\varphi'}{dt^{m-1}} + \ldots + a_1\frac{d\varphi'}{dt} + a_0\varphi'(t) = \zeta(t) \tag{1.29}$$

$$\rightarrow a_md^m\varphi'(t) + a_{m-1}d^{m-1}\varphi'(t) + \ldots + a_1d^1\varphi'(t) + a_0d^0\varphi'(t) = \zeta(t) \tag{1.30}$$

$$\rightarrow \sum_{i=0}^{m} a_id^i\varphi'(t) = \zeta(t) \quad \Big| \quad d^i\varphi'(t) = \frac{d^i\varphi'}{dt^i} \tag{1.31}$$

in which $\zeta(t)$ is again a Gaussian-distributed, now continuous, white noise process.

An Autoregressive Model

Several authors have used the continuous autoregressive model to simulate data. For instance, Hellio et al. (2014) described each Gauss coefficient pertaining to archeomagnetic data from Syria and France, depicting the geomagnetic field from 4000 B.C. to present-day and present-day to 1900 A.D. respectively, by the stochastic differential equation

$$\frac{d^2\varphi'}{dt^2} + \frac{2\sqrt{3}}{\tau_c}\frac{d\varphi'}{dt} + \frac{3}{\tau_c^2}\varphi'(t) = \zeta(t) \tag{1.32}$$

in which τ_c is a different autocorrelation timescale for each Gauss coefficient [Hellio et al., 2014]. The autocorrelation function of such a process is shown to be

$$\rho(\tau) = \left(1 + \frac{\sqrt{3}}{\tau_c}\tau\right)e^{\frac{-\sqrt{3}}{\tau_c}} \tag{1.33}$$

at each spherical harmonic degree, l. (We will go through similar steps to compute an autocovariance function for our new stochastic model, later.) Hellio et al. (2014) further demonstrated that

$$\tau_c = \sqrt{3}\frac{\sigma_{g_l}}{\sigma_{\dot{g}_l}} \tag{1.34}$$

when σ_{g_l} and $\sigma_{\dot{g}_l}$ are the variance of the degree-l Gauss coefficients and their time derivative, respectively. Both were determined from satellite observations of the modern field. The main parameter of the Hellio et al. (2014) model is τ_c and its value is extrapolated from modern field data for each Gauss coefficient similarly to how the variance and the mean of the Gauss coefficients were obtained from modern field data in CP88. The method of Hellio et al. (2014) contrasts with that of C90, in that C90 arbitrarily chose various autocorrelation timescales and observed their differing impacts on VGP paths during a reversal, while Hellio et al. (2014) obtained a fixed autocorrelation timescale from data and observe the resulting impacts on time-varying behavior in the axial dipole moment.

An Equivalent Langevin Model

Meanwhile, Buffett et al. (2013) proposed an alternative stochastic description for the axial dipole moment, the Langevin equation

$$\frac{d\varphi}{dt} = v(\varphi) + \sqrt{D(\varphi)}\Gamma(t). \tag{1.35}$$

Here, $\varphi(t) = \bar{\varphi} + \varphi'(t)$ where $\bar{\varphi}$ is the time-averaged axial dipole moment and $\varphi'(t)$ is as usual, the deviation from this mean. The $v(\varphi)$ term is called the drift and describes the tendency of the axial dipole moment to trend toward its time-average, which we assume to be its steady state. The $\sqrt{D(\varphi)}\Gamma(t)$ term is called the diffusion and describes fluctuations away from steady state [Buffett et al., 2013]. Note that the term "diffusion" here is an artifact from studies of gas dynamics, for which the Langevin equation was originally built, and does *not* refer to Ohmic diffusion in Earth's outer core.

$\Gamma(t)$ tells us when the fluctuations away from steady state occur and in the traditional Langevin equation, $\Gamma(t)$ is assumed to be Gaussian-distributed white noise. The diffusion coefficient D_{eq} tells the relative influence between underlying geodynamo processes governing the fluctuations and those governing the drift, on axial dipole moment behavior. When $D(\varphi)$ is large, $\Gamma(t)$ is weighted more heavily than $v(\varphi)$ in the Langevin equation. So the fluctuations play a larger role than the drift does in axial dipole moment behavior. After the axial dipole moment is perturbed from its equilibrium behavior, it does not have a lot of time to return to equilibrium before being pulled away again. Thus, an axial dipole moment that evolves according to the Langevin equation with high values for $D(\varphi)$ exhibits a high variance across time.

Buffett et al. (2013) demonstrate how the drift $v(\varphi)$ and diffusion coefficient

$D(\varphi)$ can be estimated from actual data or from a time-varying global field model by binning values from a time series for the axial dipole moment and then computing

$$v(\varphi) \approx \frac{< \varphi(t+\delta t) - \varphi(t) >}{\delta t} \tag{1.36}$$

$$D(\varphi) \approx \frac{< \Big(\varphi(t+\delta t) - \varphi(t)\Big)^2 >}{2\delta t} \tag{1.37}$$

in each bin. Equations 1.36 and 1.37 are called the Kramers-Moyal equations [Siefert and Peinke, 2004].

Buffett et al. (2013) posit that the geomagnetic axial dipole moment drifts toward its steady state in the same way regardless of whether the geomagnetic field is in normal or in reverse polarity. This implies that the drift $v(\varphi)$ is odd with respect to axial dipole moment $\varphi(t)$, as illustrated in Figure 1.10a. The authors similarly suggest that the relative influences of drift and diffusion on dipole behavior have no reason to be distinct between normal and reverse polarity, so $D(\varphi)$ is even with respect to axial dipole moment, as illustrated in Figure 1.10b.

Using PADM2M [Ziegler et al., 2011] as a time series representing variations in only the magnitude of $\varphi(t)$, applying Equations 1.36 and 1.37, and extending the results to negative $\varphi(t)$ values to represent reverse dipole polarities, Buffett et al. (2013) obtain the curves shown in Figure 1.10 for the effective drift and diffusion coefficient.

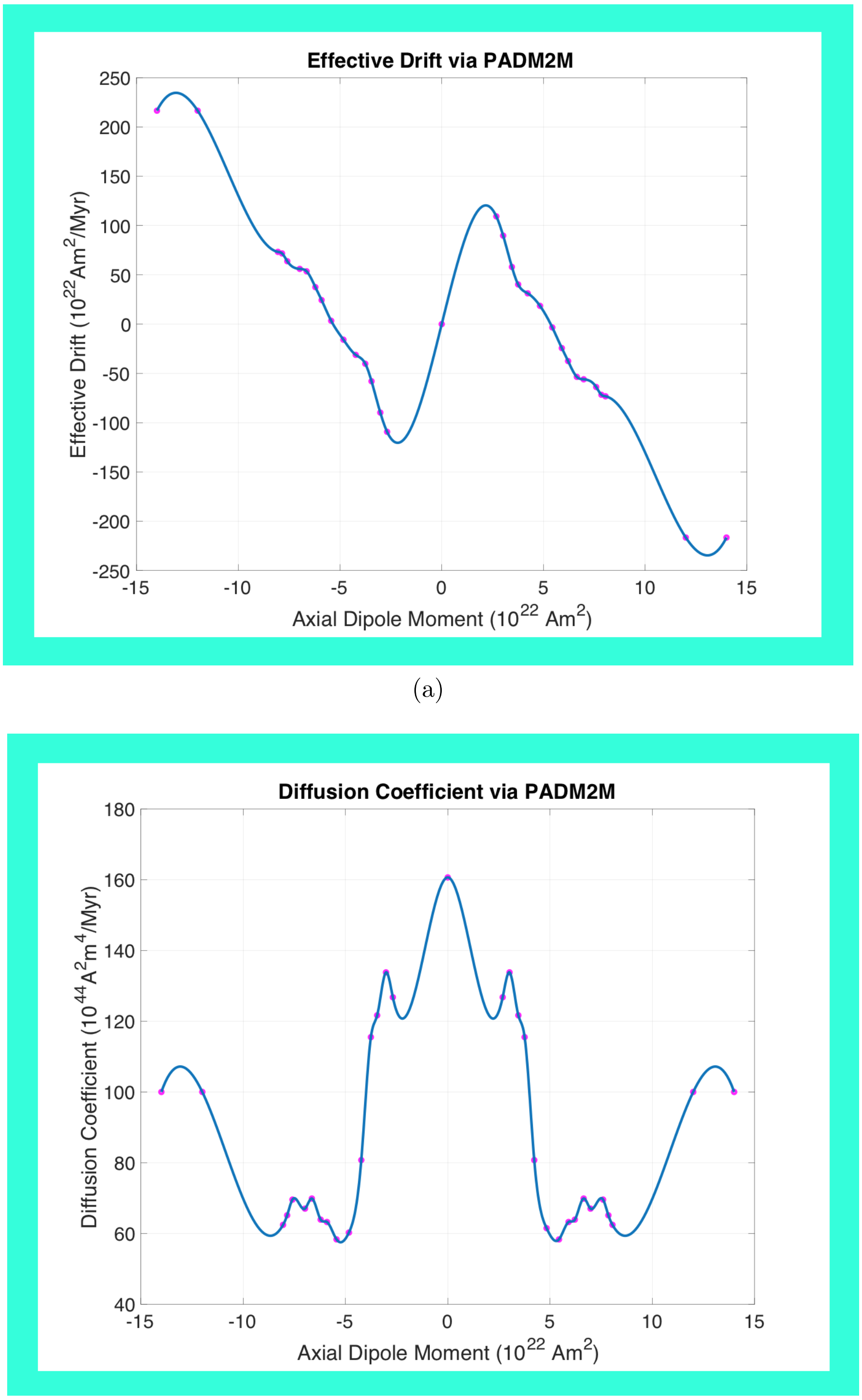

(a)

(b)

Figure 1.10: Kramers-Moyal estimates for the effective drift and diffusion coefficient are obtained by binning PADM2M and drawn as the pink dots to the right of 0 Am^2 [Buffett et al., 2013]. The pink dot at 0 Am^2 is extrapolated assuming that $v(\varphi)$ is odd and $D(\varphi)$ is even. Then the Kramers-Moyal estimates are extended to include the drift and diffusion coefficient during reverse polarity states; these are the pink dots to the left of 0 Am^2. Finally, a blue spline is drawn through the extrapolated points.

From Figure 1.10, the authors infer that when the axial dipole moment is near its time-average value, $5.34 \cdot 10^{22} Am^2$ (i.e. $\varphi'(t)$ is small), the drift and diffusion coefficient are linear with negative slope and roughly constant, respectively. The authors represent the drift and diffusion coefficient according to

$$v(\varphi) = -\frac{\varphi(t) - \bar{\varphi}}{\tau_l} \qquad \text{and} \qquad D(\varphi) \approx D(\bar{\varphi}) = D_{eq} \tag{1.38}$$

as long as $\varphi(t) - \bar{\varphi}$ is small. The approximations above might need to be reconsidered when we model axial dipole behavior that tends to be way larger or way smaller than its time-averaged value, like during reversals. Bouligand et al. (2016) suggested that the diffusion term could be assumed to be autoregressive rather than purely random motion. This yields

$$\frac{d\epsilon}{dt} + \frac{\epsilon(t)}{\tau_m} = \zeta(t) \tag{1.39}$$

where $\epsilon(t) = \sqrt{D_{eq}}\Gamma(t)$ and τ_m is the autocorrelation timescale of the diffusion. Bouligand et al. (2016) then show that the initial Langevin equation can be rewritten as

$$\frac{d^2\varphi'}{dt^2} + \Big(\frac{1}{\tau_l} + \frac{1}{\tau_m}\Big)\frac{d\varphi'}{dt} + \frac{\varphi'(t)}{\tau_l \tau_m} = \zeta(t) \tag{1.40}$$

where $\zeta(t)$ is again Brownian motion and $\varphi'(t) = \varphi(t) - \bar{\varphi}$ is the deviation of the axial dipole moment away from its mean [Bouligand et al., 2016]. We will show the steps taken to derive this when we develop our new stochastic model. Bouligand et al. (2016) effectively show that Hellio et al. (2014) and Buffett et al. (2013) were using similar stochastic models.

To summarize, stochastic models are useful to understanding the geomagnetic field because the model parameters, like the timescales in Equation 1.40, dictate how the axial dipole's past influences its future without requiring knowledge of the fluid motions in Earth's outer core. In Equation 1.40, the timescales $\{\tau_l, \tau_m\}$ must be chosen to reflect the secular variation of the axial dipole moment in time-varying global field models constructed from paleomagnetic, historical, observatory, and satellite data. We use time-varying global field models as a way of looking at the field in the past, but because the time series derived for each Gauss coefficient is not parametrized by anything that has physical meaning, we cannot use these models to predict future behavior of the field.

In contrast, the discrete GGP models and new continuous stochastic models offer a way to use past statistics of the field across large periods of time to simulate the statistical distribution of the future field, under the assumption that the field is stationary. We will see that numerical simulations are useful because they allow us to connect our model parameters with physical behaviors of the geodynamo. For example, Buffett and Matsui (2015) use the Langevin model to infer that the estimate of the drift timescale τ_l obtained by looking at the slope of $v(\varphi)$ computed using the axial dipole moment of a numerical dynamo and equations 1.36 and 1.37 depends on the vigor of fluid convection in the outer core. They then attribute the drift timescale to dipole decay and the diffusion timescale to helical flow in the outer core.

1.5 Power Spectral Density for Stochastic Models

An efficient way to infer characteristic timescales for temporal variations of the axial dipole moment is by plotting its frequency spectrum. The frequency spectrum, often defined as the Fourier transform of the autocovariance function, tells us the frequencies at which different signals within a process repeat themselves. For example, imagine an infinite sinusoidal process

$$y(t) = \sin(f_0 t). \tag{1.41}$$

If we perform the calculation illustrated in Figure 1.7, then $R_y(\tau)$ is also a sinusoid with frequency f_0. Taking the Fourier transform

$$S_y(f) = \mathscr{F}\Big(R_y(\tau)\Big) \tag{1.42}$$

then yields a frequency spectrum with a spike at f_0 and 0 everywhere else. By the same calculation, the frequency spectrum $S_y(f)$ of a process that is a linear combination of three sinusoids, each with a different frequency from the next, has three spikes and is 0 everywhere else.

Most natural processes can be Fourier expanded into a linear combination of infinitely-many sinusoids. Thus most natural processes ultimately have frequency spectra with infinitely many spikes, which ends up just looking like a nonzero net curve. It may be asked why we take the Fourier transform of the autocovariance of the process rather than simply taking the Fourier transform of the original process, to find the frequencies in the process. It can be derived that the frequency spectrum can alternatively be defined as

$$S_y(f) =< |\tilde{y}(f)|^2 > \tag{1.43}$$

where the brackets denote an expectation value and $\tilde{y}(f)$ is the Fourier transform of the original process. So essentially the frequency spectrum *is* the Fourier transform of the original process - specifically its magnitude, which is then squared to amplify the visualization of what frequencies are present, and finally averaged to indicate that we want a picture of the frequencies that appear to be consistent across all time. The brackets here come directly from the brackets in Equation 1.7. In the following sections we explore several attempts to model the frequency spectrum of the axial dipole moment.

1.5.1 The Poisson Reversal Model

Constable et al. (1998) proposed that the sequence of geomagnetic reversals in an 11 Myr Oligocene record from oceanic sediments in the South Atlantic could be modeled as a Poisson process in which the probability of a reversal is always constant [Constable et al., 1998]. The field was modeled to be at constant amplitude A until dropping to 0 at a reversal. The average reversal rate λ and average reversal duration δ of an event in this Poisson process were obtained from the Oligocene record. Constable et al. (1998) showed that the frequency spectrum of this process is

$$S(f) = \frac{4\lambda e^{-\lambda\delta}}{\lambda^2 + 4\pi^2 f^2}\left(1 - e^{-\lambda\delta}\Big(\cos(2\pi f\delta) + \frac{\lambda\sin(2\pi f\delta)}{2\pi f}\Big)\right) \tag{1.44}$$

This is a lot like the original GGP model in its lack of memory but this Poisson process operates on million-year time scales while the GGP model was built to model thousand-year statistical variability in the geomagnetic field. The 11 Myr Oligocene record was obtained from a long core drilled out of the ocean floor. The record exhibits a data gap so Constable et al. (1998) split the record into five segments in time before the gap and five segments after the gap.

Empirical frequency spectra from each of the five segments in the more recent part, 22.74 to 28.77 Ma, roughly fit $S(f)$ at low frequencies when $\lambda = 4$ Myr^{-1} and $\delta = 30$ kyr, estimated from this part of the record, are used. This is shown in Figure 1.11. Above $f = 50$ Myr^{-1}, the empirical spectra have higher power than $S(f)$ so the fit is poor. This is likely because the only form of secular variation in the model is a sequence of reversals, while the actual field has lots of other secular variation. Constable et al. (1998) conclude that the low-frequency regime of the more recent part of the record is controlled by geomagnetic reversals.

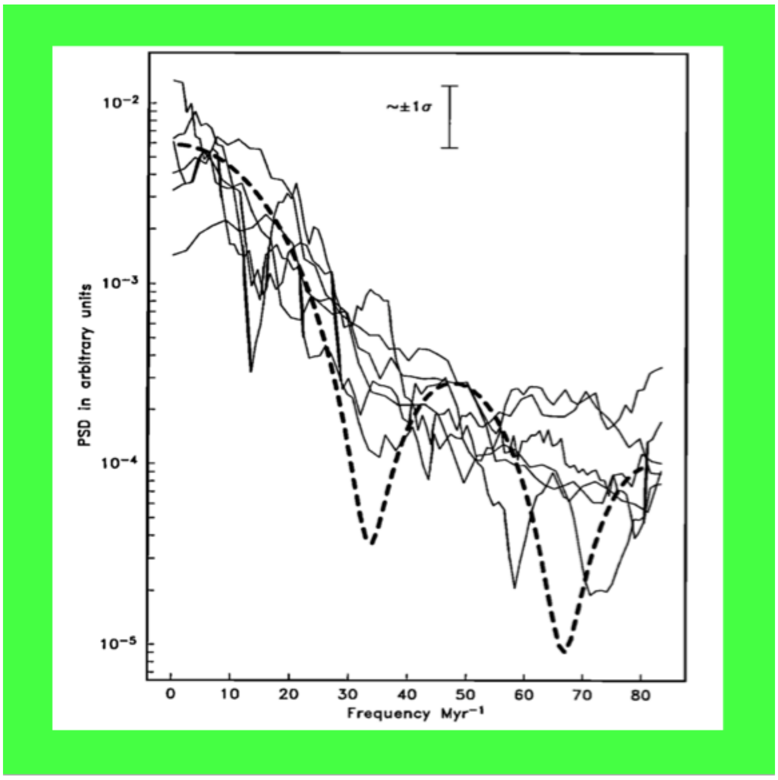

Figure 1.11: Empirical frequency spectra for the five segments of the 22.74 to 28.77 Ma part of the record are plotted. The heavy dashed curve is $S(f)$ with mean reversal rate 4 Myr^{-1}. The fit between the model and the empirical spectra is good at low frequencies. [Constable et al., 1998]

In Figure 1.12 the earlier part of the record from 29.40 to 34.74 Mya shows empirical spectra with higher power than $S(f)$ across all frequencies. While the cause of this is unknown, it is inferred that the frequency distribution of the earlier part of the record is not solely controlled by geomagnetic reversals [Smith-Boughner et al., 2011]. Evidently, the Poisson reversal model of Constable et al. (1998) does not describe the full range of secular variation behavior. After this spearheading attempt to model the frequency spectrum of the axial dipole moment, the newer stochastic models have offered alternative solutions that can describe a wider range of both frequency behavior and datasets.

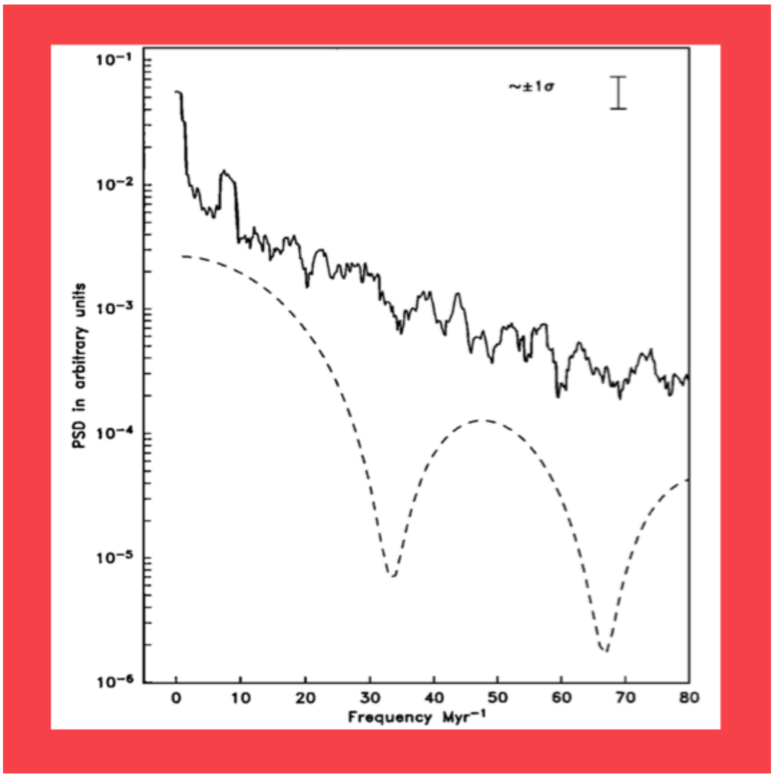

Figure 1.12: Empirical frequency spectra for the five segments of the 29.40 to 34.74 Mya part of the record are plotted. The light dashed curve is $S(f)$ with mean reversal rate 1.6 Myr^{-1}. At all frequencies, the model does not fit the empirical spectra. [Constable et al., 1998]

1.5.2 A Langevin Model

The Langevin model of Buffett and Matsui (2015) was developed in the same way as that of Buffett et al. (2013) but a linear drift and constant diffusion coefficient were obtained from a time series for the axial dipole moment in a numerical geodynamo rather than from PADM2M [Buffett and Matsui, 2015]. Buffett and Matsui (2015) rewrite the Langevin model in terms of the deviation of the axial dipole moment away from its mean and then define the frequency spectrum of their model to be the expected value of the squared magnitude of the Fourier transform of $\varphi'(t)$. Assuming that the diffusion is Brownian motion and uncorrelated, this yields

$$S(f) = \frac{2D_{eq}}{\frac{1}{\tau_l^2} + 4\pi^2 f^2} \tag{1.45}$$

as the frequency spectrum of the Langevin process. Taking the limits at low and high f, this model spectrum is flat at low frequencies and goes like f^{-2} at high frequencies, as does the spectrum of the Poisson model if the oscillations induced by reversals are ignored.

The sinusoidal terms in the large parenthesis of Equation 1.44 are negligible when $\lambda\delta$ is large. Suppose that δ is huge while λ is a "normal" size. By the Poisson model's design, this equates to supposing that the duration of each stable polarity interval is huge so fewer reversals can occur overall. Then the oscillations in the spectrum of the Poisson model vanish and Equation 1.44 is left with only the front term. Comparing the latter with Equation 1.45, we see that when reversals are rare,

$$\begin{aligned} 2D_{eq} &= 4\lambda e^{-\lambda\delta} \\ \lambda^2 &= \frac{1}{\tau_l^2}, \end{aligned} \tag{1.46}$$

which implies that τ_l directly controls the reversal rate.

Meanwhile according to Buffett et al. (2013) the slow drift timescale τ_l dictates the transition from one spectral index (i.e. s in f^{-s}) to the other. Buffett and Matsui (2015) show that the variance of the process is

$$\sigma^2 = D_{eq}\tau_l \tag{1.47}$$

by integrating $S(f)$ across all frequencies. Using the values of D_{eq} and τ_l obtained from binning the time series, the authors verify that this expression gives a value close to the variance of the original time series itself. It is noted that letting the diffusion be a singly-correlated, AR-1 process as proposed by Bouligand et al. (2016) makes the model spectrum

$$S^c(f) = \frac{2D_{eq}\tau_m^{-2}}{\left(\frac{1}{\tau_l^2} + 4\pi^2 f^2\right)\left(\frac{1}{\tau_m^2} + 4\pi^2 f^2\right)}. \tag{1.48}$$

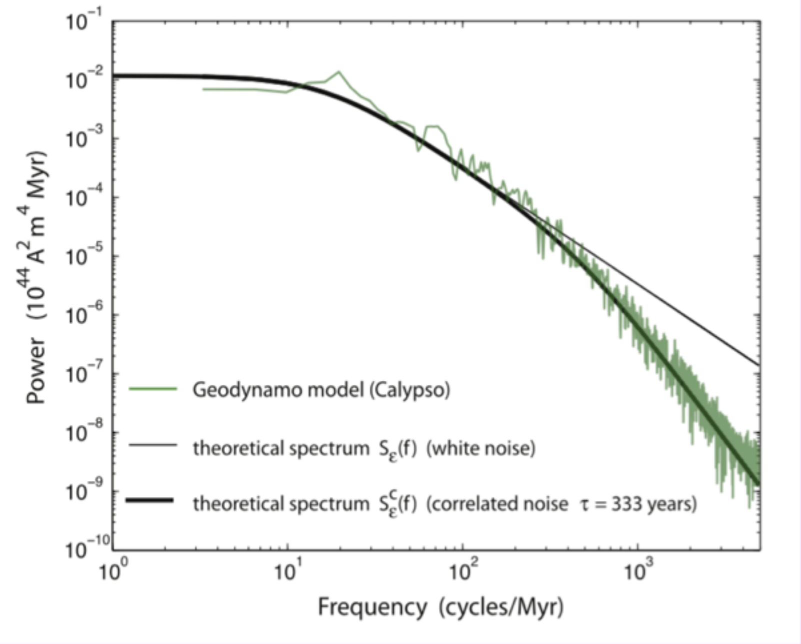

Figure 1.13: The frequency spectrum of the axial dipole moment in a geodynamo simulation called CALYPSO is plotted against Langevin model spectra assuming uncorrelated and singly-correlated noise. [Buffett and Matsui, 2015]

Figure 1.13 compares $S(f)$ and $S^c(f)$ against the empirical frequency spectrum from the axial dipole moment of the numerical geodynamo simulation Calypso [Buffett et al., 2014]. From this, Buffett and Matsui (2015) conclude that the better fit of $S^c(f)$ to the Calypso spectra indicates that the axial dipole moment should be modeled with a correlated diffusion process, $\Gamma(t)$. Using two different Calypso simulations with differing magnetic Reynolds number, the authors interpret that each diffusion correlation time τ_m is approximately one third of the corresponding simulation's convective overturn time.

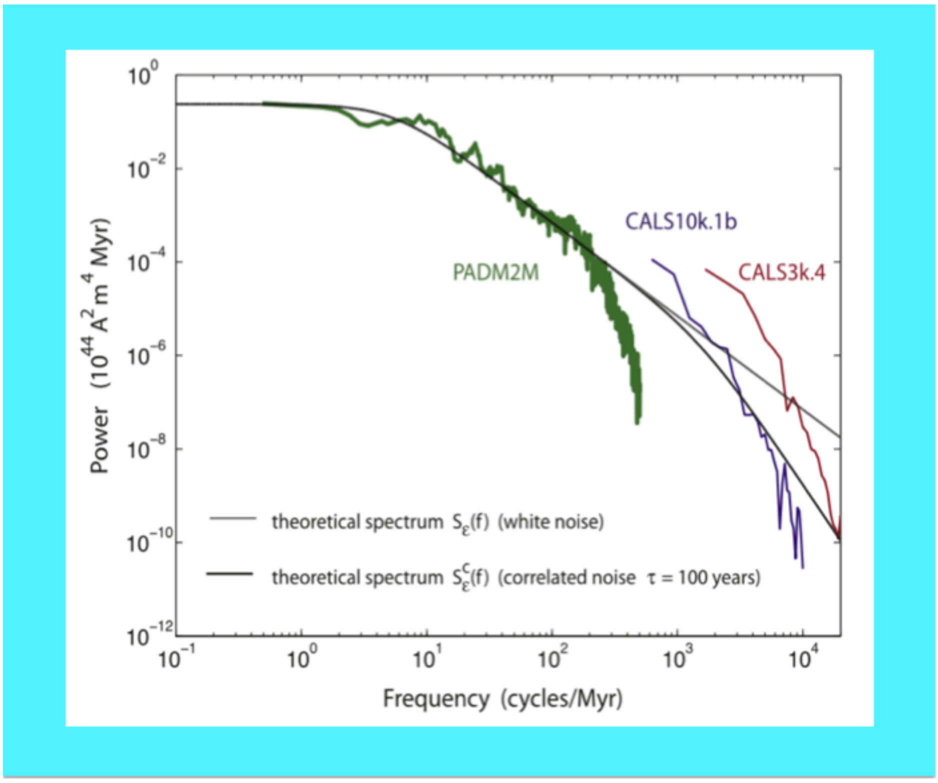

Figure 1.14: CALS10k.1b is a time-varying global field model that spans 0-10 kyr ago. CALS3k.4 is a time-varying global field model that spans 0-3 kyr ago. The empirical frequency spectra of the $g_1^0(t)$ from both models are plotted against the spectrum of PADM2M, which spans 0-2 Myr ago. The Langevin model spectra are both insufficient to describe the geomagnetic axial dipole moment at high frequencies past 10^3 cycles per Myr. [Buffett and Matsui, 2015]

As shown in Figure 1.14, when Buffett and Matsui (2015) superimpose $S(f)$ and $S^c(f)$ on the spectrum of PADM2M and with the frequency spectra for the axial dipole moment from two other time-varying global field models, the fit is poor. Not only do all of the empirical spectra exhibit much steeper curves at high frequency, but some of them do not even overlap with each other within the same frequency band. This is because the temporal resolution of the CALS10k.1b model has lower temporal resolution than CALS3k.4. Not only are frequencies higher than 10^4 cycles per Myr absent from CALS10k.1b, but the high frequencies between $2 \cdot 10^3$ and 10^4 cycles per Myr occur with much lower energy than they do in CALS3k.4. The Langevin model clearly does not capture the high-frequency behavior of the Earth's axial dipole moment, rather than that of a simulation, and further modifications are necessary.

1.5.3 Power Spectra for Numerical Dynamo Simulations

To better model the high-frequency behavior of the geomagnetic field, several authors considered geodynamo simulations with rapid timestep and shorter duration. This is a more practical approach because paleomagnetic data are sparsely distributed in both space and time, and the paleofield does not capture high-frequency variations in the ancient field. Meanwhile, satellite data do capture even hourly variations but it has been shown that some morphological characteristics of the present-day field are not fully representative of the ancient one.

Anyway, Davies and Constable (2014) devise a method of determining "earth-like" numerical dynamos based on four different morphological criteria and successfully obtain earthlike simulations whose axial dipole spectra exhibit f^{-6} dependence at high frequencies [Davies and Constable, 2014]. These are shown along with the frequency spectrum of PADM2M in Figure 1.15. It is interesting that these simulations did not seem to exhibit an f^{-4} dependence as proposed by Buffett and Matsui (2015). While Buffett and Matsui (2015) briefly mention that adding a second correlation timescale to the diffusion and making it an AR-2 process should enable f^{-6} dependence at high frequencies as hinted at by PADM2M, the authors do not propose a way to eliminate the f^{-4} dependence altogether.

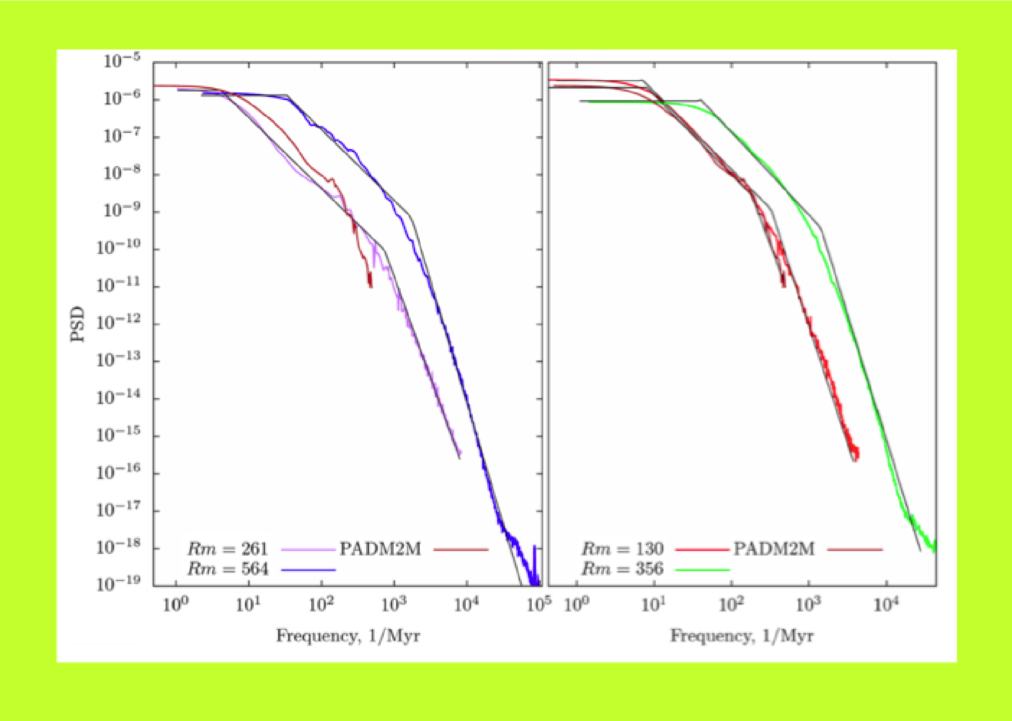

Figure 1.15: Empirical spectra of the earthlike dynamo simulations with various Rm plotted against the frequency spectrum of PADM2M. Rm is the magnetic Reynolds number, which determines the vigor of convection. Black lines show sequential power law curves that best fit the empirical spectra. Spectra are built assuming an advection timescale to give the non-dimensional simulation real-world units. [Davies and Constable, 2014]

1.5.4 Designing Stochastic Models with Appropriate Spectral Indices

Davies and Constable (2014) conclude that their simulated axial dipole spectra match reasonably well with the frequency spectra of PADM2M and two other $g_1^0(t)$ series taken from time-varying global field models. This shows improvement from the results of the Langevin model. The fundamental issue now becomes deciding whether or not the axial dipole exhibits f^{-4} dependence. It was shown that the steep falloff in PADM2M at the highest frequencies could also be modeled by accounting for sedimentary smoothing and observation error [Buffett and Puranam, 2017]. So it might be questioned whether the axial dipole even exhibits f^{-6} dependence; we would benefit greatly from a method to develop and compare varying stochastic models for the axial dipole field or moment in which different, individual spectral indices could be isolated and removed.

Fortunately such a methodology was presented recently by Bouligand et al. (2016). We rewrite Equation 1.40 as

$$\frac{d^2\varphi'}{dt^2} + 2\chi\frac{d\varphi'}{dt} + \omega^2\varphi'(t) = \zeta(t) \tag{1.49}$$

where $\zeta(t)$ is again Brownian motion and

$$2\chi = \frac{1}{\tau_l} + \frac{1}{\tau_m} \quad \texttt{and} \quad \omega^2 = \frac{1}{\tau_l\tau_m}. \tag{1.50}$$

Like Hellio et al. (2014), Bouligand et al. (2016) propose that each Gauss coefficient can be described by this model, with its own $\{\chi, \omega\}$ pair. In a method slightly different from that of Buffett et al. (2015), Bouligand et al. (2016) derive an equation for the model spectrum as

$$S(f) = \frac{4\chi\omega^2\sigma_\varphi^2}{(\omega^2 - 4\pi^2 f^2)^2 + (4\pi\chi f)^2} \tag{1.51}$$

where σ_φ^2 is the variance of the degree-l Gauss coefficient [Bouligand et al., 2016]. Notice how this equation accommodates f^0, f^{-2}, and f^{-4} regimes at low, intermediate, and high frequencies respectively. We will go through method that leads to this equation for $S(f)$ when we develop our new model.

Bouligand et al. (2016) then argue that all of the Gauss coefficients except $g_1^0(t)$ can be modeled as an AR-2 process where $\chi = \omega$ (i.e. $\tau_l = \tau_m$) just as done by Hellio et al. (2014). The model spectrum them becomes

$$S(f) = \frac{4\omega^3\sigma_\varphi^2}{(\omega^2 + 4\pi^2 f^2)^2} \tag{1.52}$$

which exhibits only f^0 and f^{-4} dependence at low and high frequencies, respectively. The latter model spectrum is constrained by only 2 parameters, $\{\sigma, \omega_\varphi\}$, while the first version has the additional parameter, χ. Following Hellio et al. (2014), Bouligand et al. (2016) note that

$$(\omega^{-1})^2 = \tau_l^2 = \frac{\sigma_\varphi^2}{\sigma_{\dot{\varphi}^2}} \rightarrow \tau_l^2 = \frac{R_l}{\dot{R}_l} \tag{1.53}$$

gives the autocorrelation timescale of the stochastic process (except the axial dipole) where $\{\sigma_\varphi^2, R_l\}$ and $\{\sigma_{\dot{\varphi}}^2, \dot{R}_l\}$ are the variance and spatial Lowes spectrum of the degree-l Gauss coefficient and its secular variation, respectively. The authors notice that the Lowes spectrum for the geomagnetic field at the core-mantle boundary computed from actual data looks like white noise and that the calculation in Equation 1.53 with data yields an inverse dependence on the spherical harmonic degree. Assuming therefore that the Lowes spectrum and timescale of the process can be described by

$$R_l \approx \alpha \quad \text{and} \quad \tau_l \approx \frac{\delta}{l}, \tag{1.54}$$

Bouligand et al. (2016) devise a way of estimating the purely-empirical parameters $\{\alpha, \delta\}$, and hence $\{\sigma_\varphi, \omega\}$, from a time-varying global field model or numerical geodynamo that can be decomposed into its spherical harmonic components. Applying these parameters, their model spectrum is compared with empirical frequency spectra from two, long geodynamo simulations with slow timestep and one, short simulation with rapid timestep. In the former two, all of the Gauss coefficients except the axial dipole exhibit f^0 and then f^{-4}

spectral behavior. In the latter simulation, the high frequency falloff is steeper than f^{-4}, suggesting an f^{-6} dependence. Meanwhile the axial dipole in all three simulations clearly exhibits an f^{-2} dependence, leading Bouligand et al. (2016) to conclude that the axial dipole should be described by the original stochastic model with $\chi \neq \omega$.

1.6 The Composite Geomagnetic Spectrum

Ultimately, the aim of this thesis is to develop a stochastic model whose frequency spectrum plausibly matches the empirical frequency spectrum of the axial dipole moment derived from actual geomagnetic field data. Before we develop our new model, we offer a final piece of evidence to convince the reader that the spectrum of the axial dipole moment can be represented by sequential segments each with a separate power law like

$$S(f) = \sum_{i=1}^{N} \alpha_i f^{-s_i} \tag{1.55}$$

where the summation index indicates the ith segment. Panovska et al. (2018) pieced together a composite spectrum for the geomagnetic axial dipole field by linking empirical spectra from various sources spanning different time intervals and with differing temporal resolution. Reversal records CK95 and CK95cc form the spectrum above million year timescales [Cande and Kent, 1995]. The $g_1^0(t)$ terms from five different time-varying global field models, derived from globally-distributed collections of igneous, archeomagnetic and lake-sediment observations (except GUFM1 based on historical data), resolve secular variation from million year to sub-decadal timescales. This is shown in Figure 1.17 and the time series for the various sources except CK95 and CK95cc are displayed in Figure 1.16.

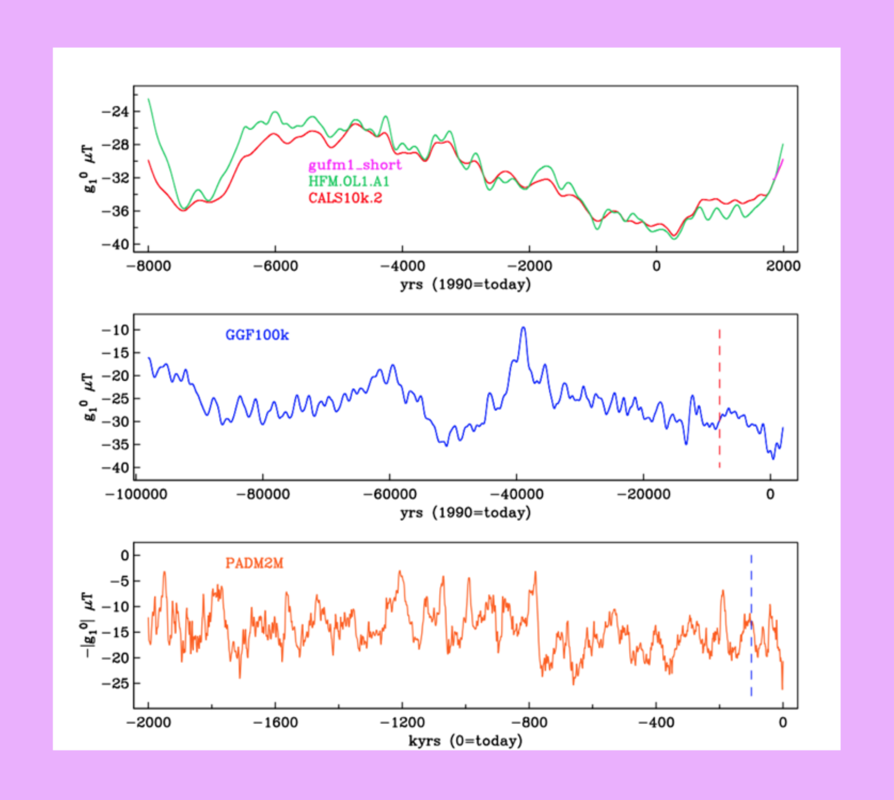

Figure 1.16: Time series representing the geomagnetic axial dipole field. PADM2M ([Ziegler et al., 2011]), GGF100k ([Panovska et al., 2018]), GUFM1 ([Jackson et al., 2000]), HFM.OL1.A1 and CALK10k.2 ([Constable et al., 2016]).

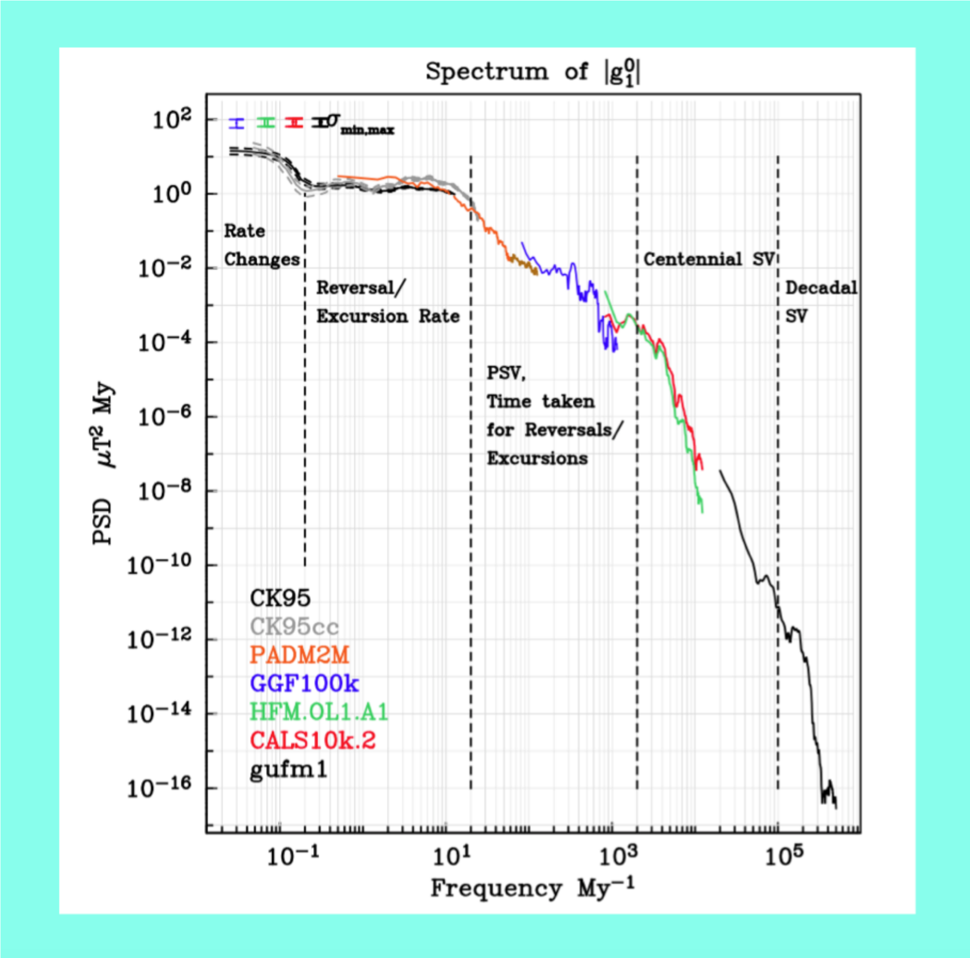

Figure 1.17: A composite spectrum for the geomagnetic axial dipole field [Panovska et al., 2018]. Black = 0-160 Ma reversal record CK95, gray = 0-83 Ma reversal record CK95cc, orange = PADM2M, blue = GGF100k, red = CALS10k.2, green = HFM.OL1.A1, black = GUFM1.

The composite spectrum clearly reflects a power law dependence with sequentially increasing spectral index, except from about $10^2 - 10^3\ Myr^{-1}$ where shallowing is seen in the GGF100k (Global Geomagnetic Field over 100 ka) model [Panovska et al., 2018]. GGF100k is the newest time-varying global field model built from sedimentary, archeomagnetic and igneous measurements. The authors used $l_{max} = 10$ and cubic splines to model time-varying Gauss coefficients. Panovska et al. (2018) multiplied the time-varying (I,D,F) predictions by a smoothing kernel that filtered out high frequencies to simulate sedimentary smoothing. Since the level of smoothing varies among records, the kernel was designed differently to match each record before evaluating the model against data using regularized inversion. Variations in the axial dipole field for GGF100k are plotted against the variations from other time-varying global field models, including PADM2M, in Figure 1.18.

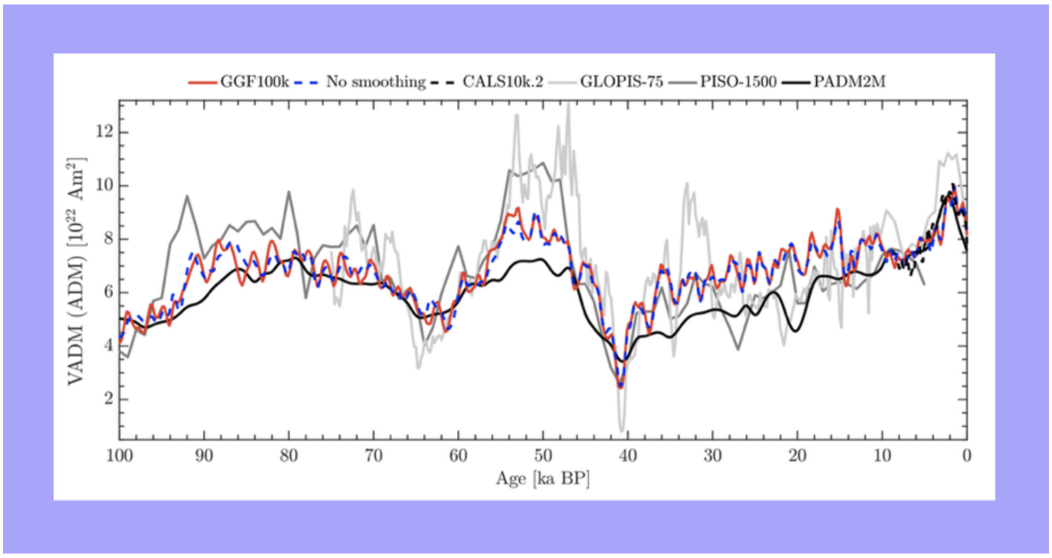

Figure 1.18: Time variations in the axial dipole field corresponding to time-varying global field models over the past 100,000 years [Panovska et al., 2018]. The color-model correspondence is listed at the top.

The jump in Figure 1.17 at frequencies below 10^{-1} Myr^{-1} probably reflects a time-varying geomagnetic reversal rate. The composite spectrum is a more comprehensive reference for stochastic models of the axial dipole field than are individual frequency spectra from time series like PADM2M, GGF100k, CALS10k.2, or GUFM1. The latter were used as references for the numerical geodynamo simulations of Davies and Constable (2014), the Langevin model of Buffett. et al. (2013), and the AR2 model of Bouligand et al. (2016). In addition to the breadth of data types in the composite spectrum, there are several reasons for our reference choice. Davies and Constable (2014) mentioned that their numerical dynamo spectra in Figure 1.15, which match the spectrum of PADM2M pretty well, do not exhibit any f^{-4} dependence and that this may be due to poor frequency resolution. Perhaps there was a short regime of f^{-4} dependence in the geodynamo simulations, but only the smooth transition, $f^0 \to f^{-2} \to f^{-6}$, is visible.

Then, Buffett and Puranam (2017) suggested that the rapid falloff immediately after f^{-2} is actually a consequence of sedimentary smoothing in the paleomagnetic data used to construct PADM2M [Buffett and Puranam, 2017]. They modeled the effect as a low pass filter applied to the Langevin model spectrum (the one with AR1 diffusion) that initially exhibited an $f^0 \to f^{-2} \to f^{-4}$ power law sequence. The cutoff frequency of the filter is inversely proportional to the timescale over which enough sedimentation and compaction occurs. A slow sedimentation rate means that it takes a while for the sediments to settle and “lock in” a single, detrital remanence. Since the locked-in value is essentially an average of the local field over that settling time, the paleofield record is smoothed as high-frequency variations in the local field get averaged out. In this scenario the timescale for compaction is longer, i.e. the cutoff frequency is lower so that the bandpass filter keeps only the lowest frequencies of the original secular variation. Applying the filter yielded Figure 1.19.

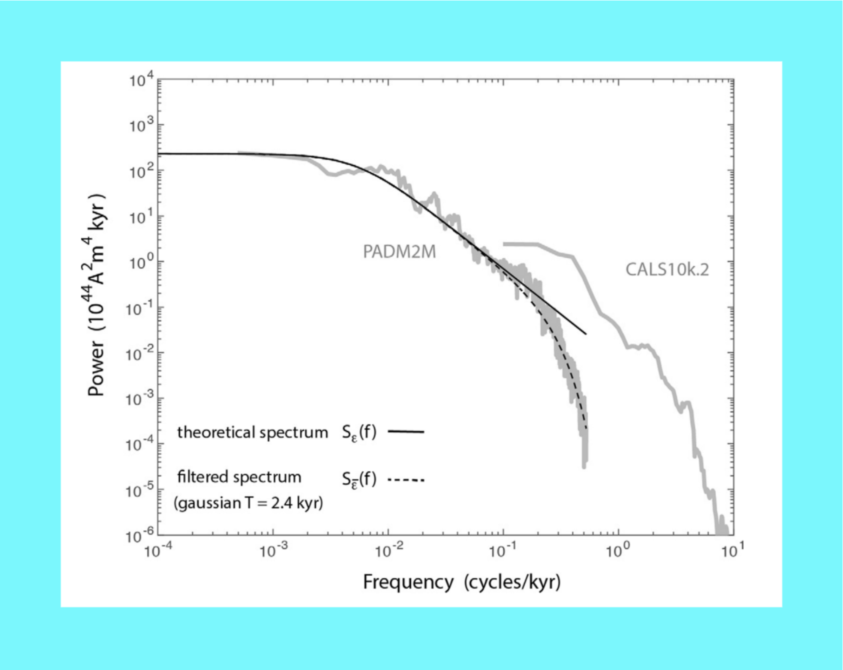

Figure 1.19: A Gaussian filter with averaging time 2.4 kyr was applied to the Langevin model spectrum $S(f)$ derived by assuming that the diffusion is uncorrelated Brownian motion [Buffett and Puranam, 2017].

Buffett and Puranam (2017) therefore argued that the rapid falloff in PADM2M is from the filter and is not a feature of Earth's axial dipole, while any f^{-6} dependence in Earth's axial dipole should occur at higher frequencies with a significant f^{-4} section before it. We hence infer that the frequency spectrum of the geomagnetic axial dipole field likely has $\{f^0, f^{-2}, f^{-4}, f^{-6}\}$ dependence, in that order from lowest to highest frequencies. We just need better resolution to see it, in both geodynamo simulations and in compilations of time-varying global field models.

Chapter 2

Building a New Stochastic Model to Satisfy Geomagnetic Observations

Chapter 1 outlined the current status of stochastic modelling for the geomagnetic field. The GGP models discussed in Section 1.4.4 lack the long-term memory associated with low-frequency changes in the dipolar part of the field. Newer models based on the Langevin and continuous-autoregressive equations are related but their frequency spectra do not fit the composite geomagnetic spectrum for axial dipole field variations shown in Figure 1.17. In this Chapter we extend previously-developed Langevin models and recast them as continuous-autoregressive models for the geomagnetic axial dipole moment. Simulations of a new third-order model are produced and their frequency spectra are compared with the composite geomagnetic spectrum. We first lay out several reference equations that become useful when we extend the previously-published models.

2.1 Derivations of Continuous-Autoregressive (AR) Stochastic Models

2.1.1 Simplified Langevin Equation

The Langevin equation is

$$\frac{d\varphi}{dt} = v(\varphi(t)) + \sqrt{D(\varphi(t))}\Gamma(t), \tag{2.1}$$

where $\varphi(t)$ is the axial dipole moment. The drift $v(\varphi(t))$ describes the tendency of the axial dipole moment to return to its time-averaged steady state when perturbed away. The diffusion $\sqrt{D(\varphi(t))}\Gamma(t)$ describes shorter-term fluctuations of the axial dipole moment away from steady state. $\Gamma(t)$ is assumed to be a zero-mean process as presented by Buffett et al. (2013). The diffusion coefficient $\sqrt{D(\varphi(t))}$ is the time-dependent amplitude of such fluctuations.

Following the derivation of Buffett et. al. (2013), we assume that the drift may be represented by

$$v(\varphi(t)) \approx \frac{-(\varphi(t) - \bar{\varphi}(t))}{\tau_l} = \frac{-\varphi'(t)}{\tau_l} \tag{2.2}$$

where $\varphi'(t)$ is the deviation of the dipole moment from its time-average, $\bar{\varphi}(t)$ [1]. Meanwhile $\sqrt{D(\varphi(t))}$ is the amplitude of fluctuations about $\bar{\varphi}(t)$ so we

---

[1] We will use brackets $< y(t) >$ to indicate taking the expectation value, i.e. an operation,

assume that that on average, it is equal to the value it takes on at $\bar{\varphi}(t)$, like

$$D(\varphi(t)) \approx D(\bar{\varphi}(t)) \equiv D_{eq}. \tag{2.3}$$

The simplified Langevin equation is finally

$$\frac{d\varphi'}{dt} + \frac{\varphi'(t)}{\tau_l} = \sqrt{D_{eq}}\Gamma(t). \tag{2.4}$$

We briefly consider the units of each term in the simplified Langevin equation. We use bracket notation to indicate units. The left side clearly has units of $\frac{Am^2}{Myr}$ and the diffusion coefficient has units $[Deq] = \frac{A^2m^4}{Myr}$; putting these together yields that

$$[\Gamma(t)] = \frac{1}{\sqrt{Myr}}. \tag{2.5}$$

Consequently the autocovariance of the diffusion process has units

$$[R_\Gamma(\tau)] \equiv [< \Gamma(t+\tau)\Gamma(t) >] = \frac{1}{Myr}. \tag{2.6}$$

---

and a bar $\bar{y}(t)$ to indicate the mean of a process, i.e. a defined quantity.

This proves useful later.

2.1.2 Model Spectrum

A general formula for the frequency spectrum of $\varphi(t)$ also proves useful later. To start, we define the frequency spectrum of any arbitrary, zero-mean process $y(t)$ to be

$$S_y(f) \equiv < |\tilde{y}(f)|^2 > \tag{2.7}$$

where the brackets mean an expectation value. The spectrum is also commonly defined as

$$S_y(f) \equiv \mathscr{F}\Big(R_y(\tau)\Big). \tag{2.8}$$

We will use both definitions while developing our three models. Based on the first definition, we take the Fourier transform of Equation 2.4 and obtain our model variance,

$$S_{\varphi'}(f) \equiv |\tilde{\varphi}'(f)|^2 = \frac{D_{eq}|\tilde{\Gamma}(f)|^2}{4\pi^2 f^2 + \frac{1}{\tau_l^2}} \tag{2.9}$$

where $< \Gamma(t) >\equiv 0$. We define the model variance to be

$$\sigma_{\varphi'}^2 \equiv \int_{-\infty}^{\infty} S_{\varphi'}(f)df \tag{2.10}$$

The diffusion spectrum, $|\tilde{\Gamma}(f)|^2$, depends on the correlation of $\Gamma(t)$. Now we can develop first, second, and third-order continuous autoregressive models for the geomagnetic axial dipole moment by modeling the diffusion $\Gamma(t)$ in the Langevin equation as a zeroth, first, and second-order autoregressive process - interchangeably referred to as uncorrelated, singly-correlated, and doubly-correlated diffusion, respectively. [2]

---

[2] Langevin models with uncorrelated and singly-correlated diffusion were developed and proposed, respectively, by Buffett et. al. (2013). We present both here in more detail and extrapolate upon them to derive the corresponding autoregressive equation. Doing so facilitates a smooth transition to the derivation of a new, doubly-correlated model.

2.1.3 An AR1 Stochastic Model for the Axial Dipole Moment

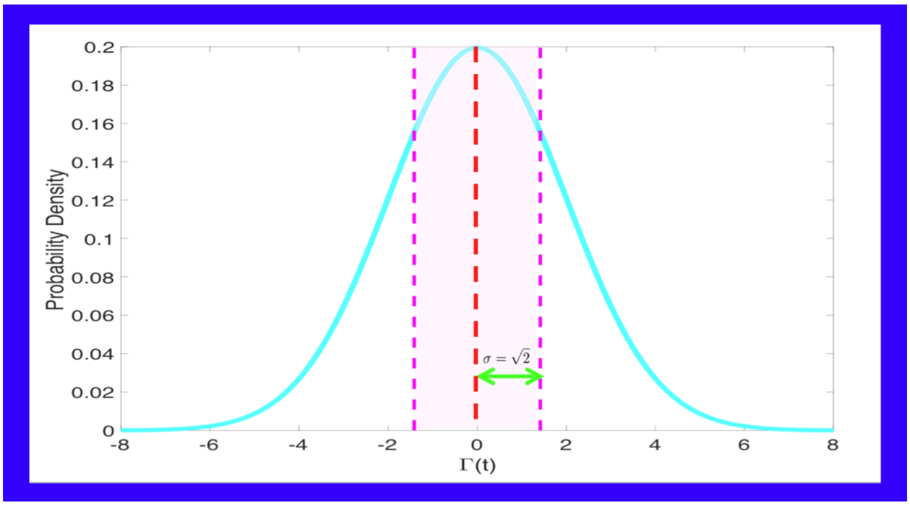

Figure 2.1: The value of $\Gamma(t)$ at any time t is random, but the probability that the value lies within a specific range is prescribed by this distribution. About 68 % of the time the value of $\Gamma(t)$ lies between $\pm\sqrt{2}$ and on average $\Gamma(t)$ is 0.

Suppose that the diffusion, $\Gamma(t)$, is uncorrelated, Gaussian-distributed, random noise with variance 2 [3] (so the standard deviation is $\sqrt{2}$). The Gaussian distribution is illustrated in Figure 2.1. $\Gamma(t)$ is described by

$$\Gamma(t) = \zeta(t) \qquad \text{and} \quad R_\Gamma(\tau) = 2\delta(\tau). \tag{2.11}$$

Equation 2.11 implies that $|\tilde{\Gamma}(f)|^2 = |\tilde{\zeta}(f)|^2 = 2$, so Equation 2.9 gives that

---

[3] The reason for this variance is discussed in Appendix B.

$$S_{\varphi'}(f) = \frac{2D_{eq}}{4\pi^2 f^2 + \frac{1}{\tau_l^2}} \qquad \text{and} \qquad \sigma^2_{\varphi'} = D_{eq}\tau_l \tag{2.12}$$

are the model spectrum and model variance, respectively. Figures 2.2 and 2.3 show the spectrum and the distribution for $\varphi'(t)$, respectively.

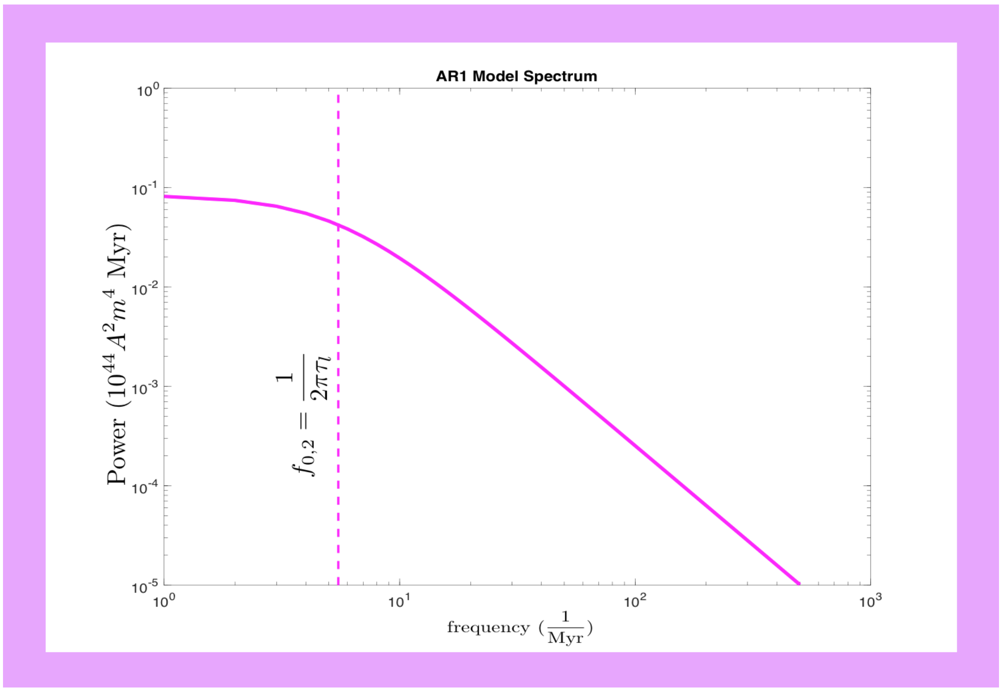

Figure 2.2: We infer the shape of the AR1 model spectrum using Equation 2.12. At low frequencies, $f \to 0$ implies that $S_{\varphi'}(f) \approx 2D_{eq}\tau_l^2$ and at high frequencies, $f \to \infty$ gives that $S_{\varphi'}(f) \propto \frac{1}{f^2}$.

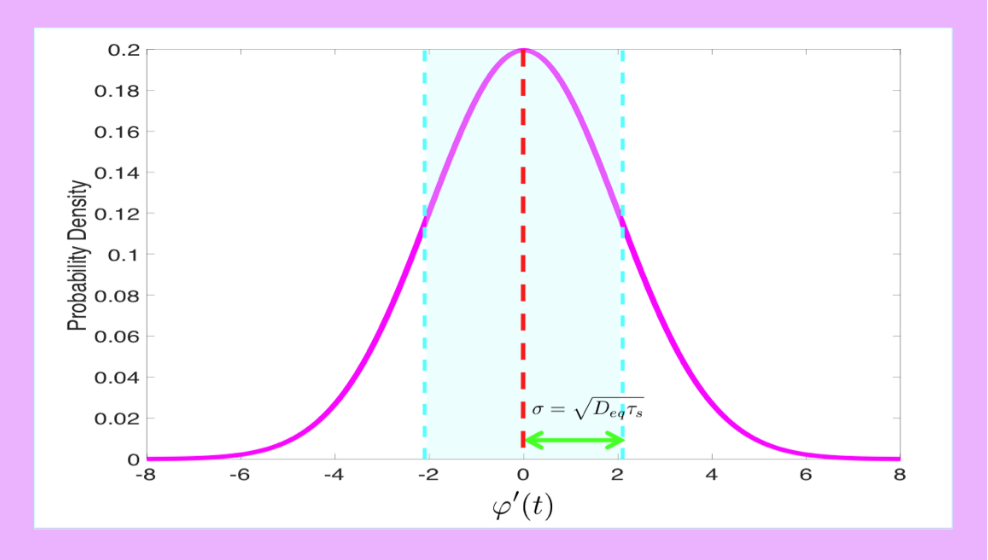

Figure 2.3: We use a Gaussian distribution to represent the probability that $\varphi'(t)$ lies within a specific range of values at any time t. The AR1 model predicts that about 96 % of the time, $\varphi'(t)$ lies between $\pm\sqrt{D_{eq}\tau_l}$ and that on average, $\varphi'(t)$ is 0.

The AR1 model spectrum in Figure 2.2 is flat at low frequencies and then transitions to f^{-2} behavior at higher frequencies. The frequency at which the transition occurs is directly provided by the timescale parameter of the AR1 model, τ_l, via

$$f_{0,2} = \frac{1}{2\pi\tau_l}. \tag{2.13}$$

We combine Equation 2.11 and Equation 2.4 to derive a single, continuous-autoregressive equation that describes the deviation of the axial dipole moment from its time-average,

$$\frac{d\varphi'}{dt} + \frac{1}{\tau_l}\varphi'(t) = \sqrt{D_{eq}}\zeta(t). \tag{2.14}$$

Hence we produce a stochastic differential equation that describes the deviations of the axial dipole moment away from its equilibrium behavior with respect to time. Our differential representation is driven by white noise, $\zeta(t)$ and contains two parameters: the drift timescale τ_l and the diffusion coefficient D_{eq}, the latter of which dictates the relative influence between fluctuations away from and drift towards steady state, on the axial dipole behavior. To obtain the model autocovariance, we compute the solution to the differential equation [4]

$$\frac{dR_{\varphi'}}{d\tau} + \frac{1}{\tau_l} R_{\varphi'}(\tau) = 0, \tag{2.15}$$

which is just $R_{\varphi'}(\tau) = R_0 e^{\frac{-\tau}{\tau_l}}$. By computing the Fourier transform of $R_{\varphi'}(\tau)$ (the second definition for the frequency spectrum of a process) and comparing the result with the model spectrum in Equation 2.12, we infer that $R_0 = D_{eq}\tau_l$ so the model autocovariance is

$$R_{\varphi'}(\tau) = D_{eq}\tau_l e^{\frac{-\tau}{\tau_l}}. \tag{2.16}$$

$R_{\varphi'}(\tau)$ is plotted against the autocovariance of PADM2M [Ziegler et al., 2011], which clearly contains periodic behavior yet to be understood, in Figure

---

[4] See Appendix A for a proof of how this differential equation describes the model autocovariance.

2.4.

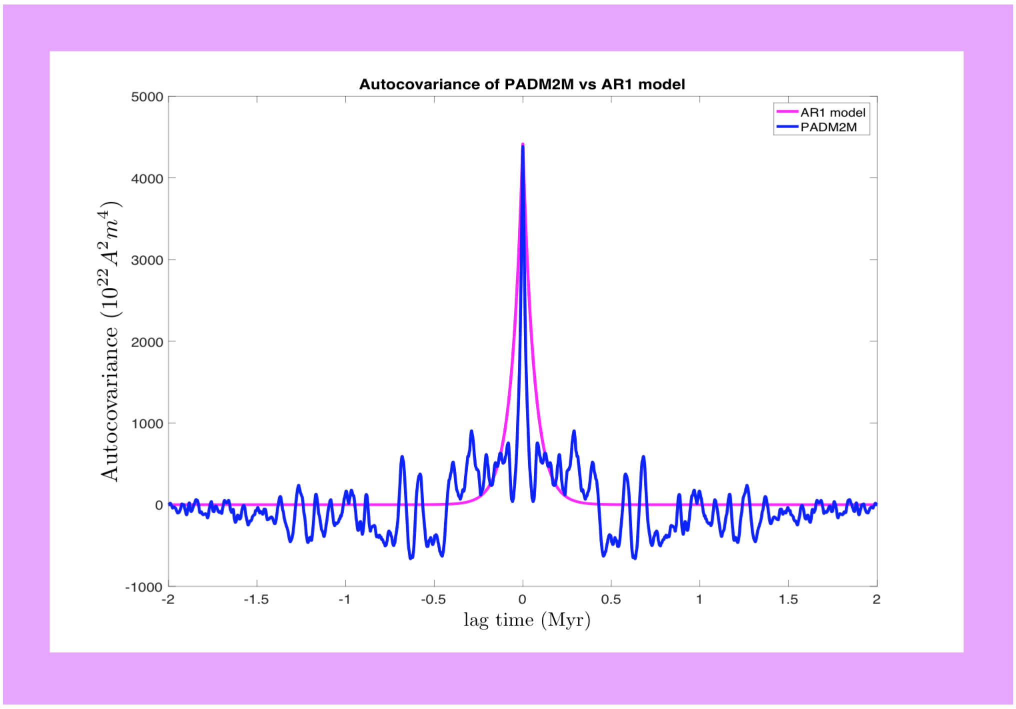

Figure 2.4: The autocovariance of a continuous process often decays exponentially like the pink curve. A process comprised of periodic signals will exhibit similar periodicity in its autocovariance. The autocovariance of PADM2M [Ziegler et al., 2011] decays exponentially on large timescales but is periodic on short timescales.

2.1.4 An AR2 Stochastic Model for the Axial Dipole Moment

Suppose that the diffusion, $\Gamma(t)$, is an order-1 autoregressive process with one autocorrelation timescale, τ_m. So $\Gamma(t)$ is described by

$$a\frac{d\Gamma}{dt} + b\Gamma(t) = \zeta(t) \tag{2.17}$$

where a and b are yet-unknown parameters and $\zeta(t)$ is again Gaussian-distributed random noise with variance 2. Equation 2.17 implies that

$$a\frac{dR_\Gamma}{d\tau} + bR_\Gamma(\tau) = 0 \tag{2.18}$$

where $R_\Gamma(\tau) = R_0e^{\alpha\tau}$ is the autocovariance function of $\Gamma(t)$. We assume that the autocovariance is of exponential form so the characteristic equation simplifies to

$$\alpha = \frac{-b}{a}. \tag{2.19}$$

We want the exponent of $R_\Gamma(\tau)$ to be unitless and the only parameter that describes $\Gamma(t)$ is τ_m so we assume that

$$\alpha = \frac{-b}{a} = \frac{-1}{\tau_m}. \tag{2.20}$$

Meanwhile we know that $[R_\Gamma(\tau)] = \frac{1}{Myr}$ and our only parameter is τ_m so we assume that $R_0 = \frac{1}{\tau_m}$ and thus

$$R_\Gamma(\tau) = \frac{1}{\tau_m} e^{\frac{-\tau}{\tau_m}} \tag{2.21}$$

is the autocovariance of the diffusion process that satisfies

$$\implies \tau_m \frac{d\Gamma}{dt} + \Gamma(t) = \zeta(t). \tag{2.22}$$

We find $|\tilde{\Gamma}(f)|^2$ in two ways. We either compute the Fourier transform of Equation 2.22 and obtain

$$\implies |\tilde{\Gamma}(f)|^2 = \frac{2}{\tau_m^2} \frac{1}{4\pi^2 f^2 + \frac{1}{\tau_m^2}} \tag{2.23}$$

or we compute the Fourier transform of Equation 2.21, which yields the same result. Again combining with Equation 2.9,

$$S_{\varphi'}(f) = \frac{2D_{eq}}{\tau_m^2} \frac{1}{(4\pi^2 f^2 + \frac{1}{\tau_l^2})(4\pi^2 f^2 + \frac{1}{\tau_m^2})} \tag{2.24}$$

$$\text{and} \qquad \sigma^2_{\varphi'} = \frac{D_{eq}\tau_l^2}{\tau_l + \tau_m}, \tag{2.25}$$

are the model spectrum and model variance, respectively. The model spectrum and a Gaussian distribution for $\varphi'(t)$ are plotted in Figures 2.5 and 2.6, respectively. [5]

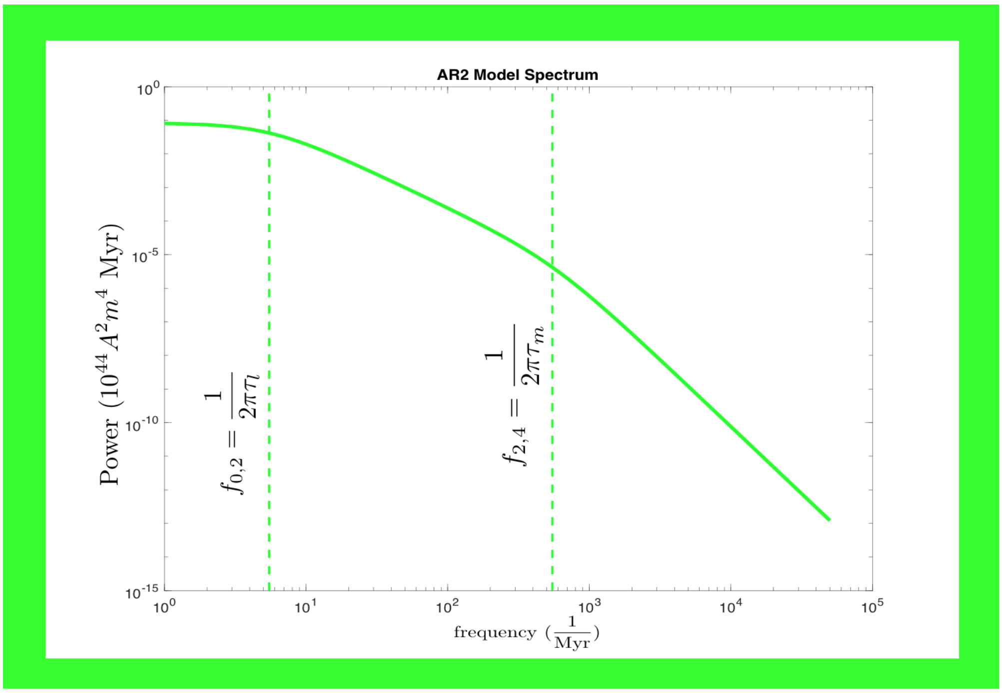

Figure 2.5: We infer the shape of the AR2 model spectrum using Equation 2.24. At lowest frequencies, $f \to 0$ implies that $S_{\varphi'}(f) \approx 2D_{eq}\tau_l^2$. At intermediate frequencies, we have that $S_{\varphi'}(f) \propto \frac{1}{f^2}$. At high frequencies, $f \to \infty$ gives that $S_{\varphi'}(f) \propto \frac{1}{f^4}$.

---

[5] In computing the variance of the process $\varphi'(t)$, we are not explicitly assuming $\varphi'(t)$ is described by a Gaussian probability density distribution. However, it is a useful way of visualizing what is going on.

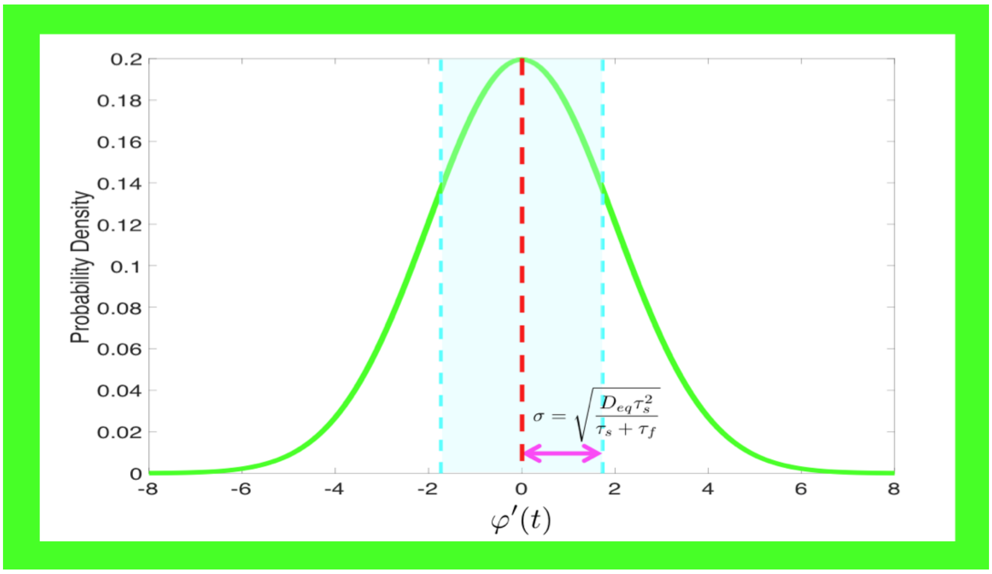

Figure 2.6: We use a Gaussian distribution to represent the probability that $\varphi'(t)$ lies within a specific range of values at any time t. The AR2 model predicts that about 68 % of the time, $\varphi'(t)$ lies between $\pm\sqrt{\frac{D_{eq}\tau_l^2}{\tau_l+\tau_m}}$ and that on average, $\varphi'(t)$ is 0.

The AR2 model spectrum is flat at lowest frequencies, switches to f^{-2} behavior, and then transitions again to f^{-4} behavior. The frequency at which the latter transition occurs is given directly to us by the new timescale parameter τ_m via

$$f_{2,4} = \frac{1}{2\pi\tau_m}. \tag{2.26}$$

We next combine Equation 2.22 with Equation 2.4 to derive a single, continuous-autoregressive equation,

$$\tau_m \frac{d^2\varphi'}{dt^2} + (\frac{\tau_m}{\tau_l} + 1)\frac{d\varphi'}{dt} + \frac{1}{\tau_l}\varphi'(t) = \sqrt{D_{eq}}\zeta(t), \tag{2.27}$$

that describes the deviation of the axial dipole moment away from its time average. The AR2 model autocovariance satisfies

$$\tau_m \frac{d^2 R_{\varphi'}}{d\tau^2} + (\frac{\tau_m}{\tau_l} + 1)\frac{dR_{\varphi'}}{d\tau} + \frac{1}{\tau_l} R_{\varphi'}(\tau) = 0 \tag{2.28}$$

so we assume a general solution of the form

$$R_{\varphi'}(\tau) = \alpha_1 e^{-\frac{\tau}{\tau_l}} + \alpha_2 e^{-\frac{\tau}{\tau_m}}, \tag{2.29}$$

compute its Fourier transform, and compare the result with Equation 2.24 to determine α_1 and α_2. The model autocovariance is

$$R_{\varphi'}(\tau) = \frac{-D_{eq}\tau_l^3}{\tau_m^2 - \tau_l^2} e^{-\frac{\tau}{\tau_l}} + \frac{D_{eq}\tau_m\tau_l^2}{\tau_m^2 - \tau_l^2} e^{-\frac{\tau}{\tau_m}}. \tag{2.30}$$

When $\tau_l = \tau_m$, the AR2 model autocovariance is 0. When $\tau_m << \tau_l$, $e^{-\frac{\tau}{\tau_m}}$ is negligibly small and Equation 2.30 reduces to Equation 2.16.

2.1.5 An AR3 Stochastic Model for the Axial Dipole Moment

Suppose that the diffusion, $\Gamma(t)$, is an order-2 autoregressive process with two autocorrelation timescales τ_m and τ_s. So $\Gamma(t)$ is described by

$$a\frac{d^2\Gamma}{dt^2} + b\frac{d\Gamma}{dt} + c\Gamma(t) = \zeta(t) \tag{2.31}$$

where a, b and c are yet-unknown parameters. In Equation 2.22, a and b ultimately counteract the units of time in the denominator of each derivative term. We assume that a and b will do the same so Equation 2.31 implies that

$$[a] = Myr^2 \qquad [b] = Myr \qquad \text{and} \qquad [c] = 1. \tag{2.32}$$

All of our model parameters inevitably have some physical units so we conclude that c must be 1. Equation 2.31 then implies that

$$a\frac{d^2R_\Gamma}{d\tau^2} + b\frac{dR_\Gamma}{d\tau} + R_{\Gamma(\tau)} = 0 \tag{2.33}$$

where $R_\Gamma(\tau) = R_0 e^{\alpha\tau}$ is the general form autocovariance of $\Gamma(t)$. The characteristic equation simplifies to

$$\alpha = \frac{-b \pm \sqrt{b^2 - 4a}}{2a}. \tag{2.34}$$

To determine a and b, we compute the Fourier transform of Equation 2.31 and compare the denominator in $|\tilde{\Gamma}(f)|^2$ to [6]

$$\propto \frac{1}{(4\pi^2 f^2 + \frac{1}{\tau_m^2})(4\pi^2 f^2 + \frac{1}{\tau_s^2})}. \tag{2.35}$$

We thus obtain a and b as functions of τ_m and τ_s, which result in the diffusion spectrum

$$|\tilde{\Gamma}(f)|^2 = \frac{2}{\tau_m^2 \tau_s^2} \frac{1}{(4\pi^2 f^2 + \frac{1}{\tau_m^2})(4\pi^2 f^2 + \frac{1}{\tau_s^2})}. \tag{2.36}$$

Meanwhile $R_\Gamma(\tau)$ is

---

[6] Equations 2.24 and 2.27 suggest this form for the denominator of the spectrum of a process described by an order-2 autoregressive equation.

$$R_\Gamma(\tau) = R_1 e^{\frac{-\tau}{\tau_m}} + R_2 e^{\frac{-\tau}{\tau_s}} \tag{2.37}$$

and satisfies

$$\tau_m \tau_s \frac{d^2\Gamma}{dt^2} + \tau_m \tau_s (\frac{1}{\tau_m} + \frac{1}{\tau_s}) \frac{d\Gamma}{dt} + \Gamma(t) = \zeta(t). \tag{2.38}$$

We infer R_1 and R_2 by computing the Fourier transform of $R_\Gamma(\tau)$ and comparing it with Equation 2.36. So the autocovariance of $\Gamma(t)$ is

$$R_\Gamma(\tau) = \frac{\tau_m}{\tau_m^2 - \tau_s^2} e^{\frac{-\tau}{\tau_m}} + \frac{\tau_s}{\tau_s^2 - \tau_m^2} e^{\frac{-\tau}{\tau_s}}. \tag{2.39}$$

By Equation 2.36, the model spectrum and model variance are

$$S_{\varphi'}(f) = \frac{2D_{eq}}{\tau_m^2 \tau_s^2} \frac{1}{((4\pi^2 f^2 + \frac{1}{\tau_l^2})(4\pi^2 f^2 + \frac{1}{\tau_m^2})(4\pi^2 f^2 + \frac{1}{\tau_s^2})} \tag{2.40}$$

$$\sigma_{\varphi'}^2 = \frac{D_{eq}}{\tau_m^2 \tau_s^2}\Big(\gamma_s \tau_l + \gamma_1 \tau_m + \gamma_2 \tau_s\Big) \qquad \text{such that} \tag{2.41}$$

$$\begin{aligned}
\gamma_s &= \frac{1}{(\frac{1}{\tau_l^2} - \frac{1}{\tau_m^2})(\frac{1}{\tau_l^2} - \frac{1}{\tau_s^2})} \\
\gamma_1 &= \frac{1}{(\frac{1}{\tau_m^2} - \frac{1}{\tau_l^2})(\frac{1}{\tau_m^2} - \frac{1}{\tau_s^2})} \\
\gamma_2 &= \frac{1}{(\frac{1}{\tau_s^2} - \frac{1}{\tau_m^2})(\frac{1}{\tau_s^2} - \frac{1}{\tau_l^2})}.
\end{aligned} \tag{2.42}$$

These are plotted in Figures 2.7 and 2.8, respectively.

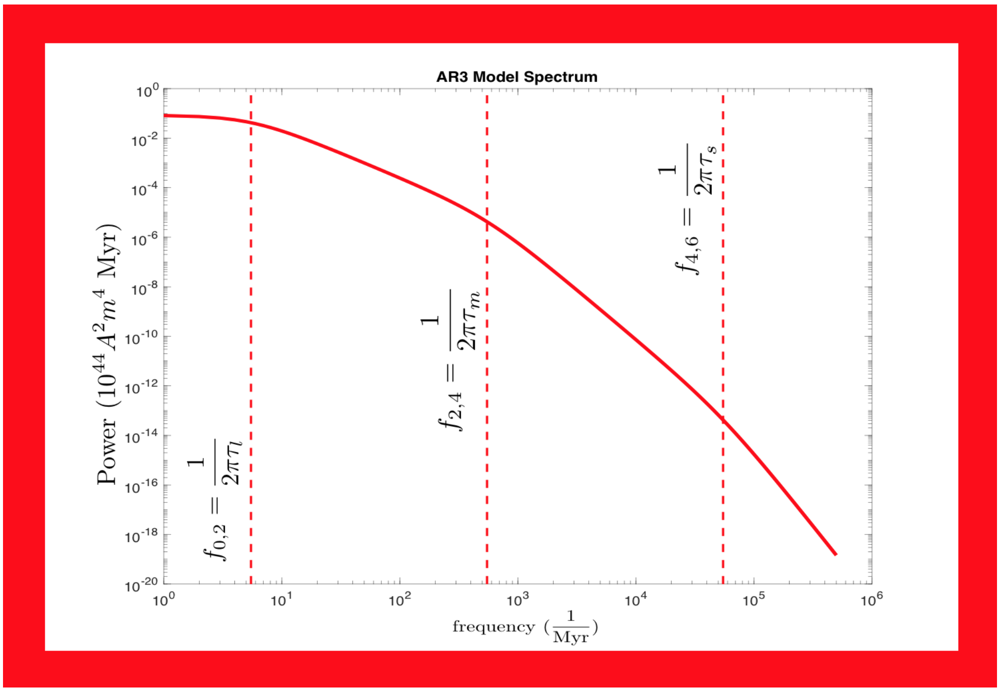

Figure 2.7: We infer the shape of the AR3 model spectrum using Equation 2.40. At lowest frequencies, $f \to 0$ implies that $S_{\varphi'}(f) \approx 2D_{eq}\tau_l^2$. At mid-low frequencies, we have that $S_{\varphi'}(f) \propto \frac{1}{f^2}$. At mid-high frequencies, we have that $S_{\varphi'}(f) \propto \frac{1}{f^4}$. At highest frequencies, $f \to \infty$ gives that $S_{\varphi'}(f) \propto \frac{1}{f^6}$.

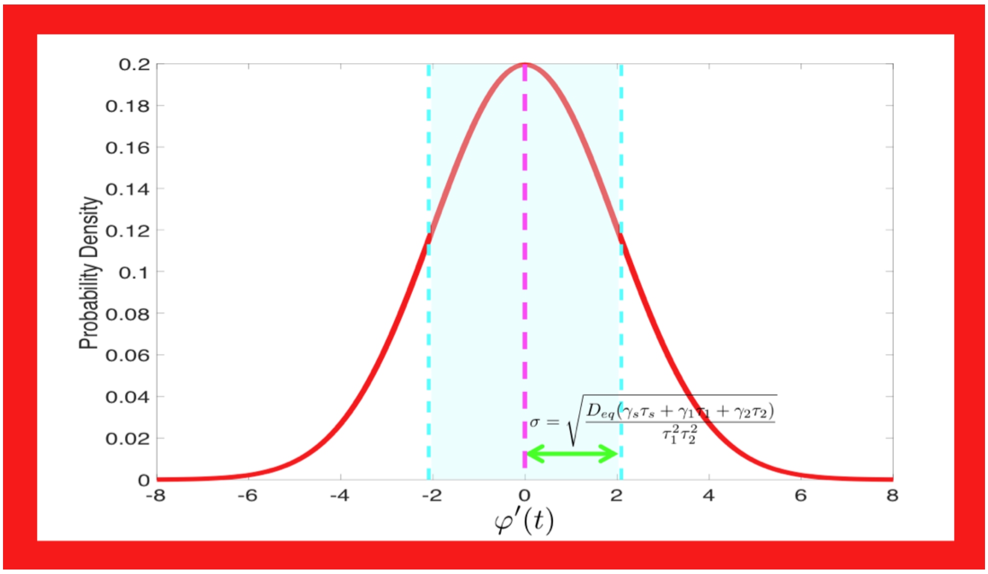

Figure 2.8: We use a Gaussian distribution to represent the probability that $\varphi'(t)$ lies within a specific range of values at any time t. The AR3 model predicts that about 68 % of the time, $\varphi'(t)$ lies between $\pm\sqrt{\frac{D_{eq}}{\tau_m^2\tau_s^2}\left(\gamma_s\tau_l + \gamma_1\tau_m + \gamma_2\tau_s\right)}$ and that on average, $\varphi'(t)$ is 0.

The AR3 model spectrum is flat at lowest frequencies and reaches an f^{-6} dependence at highest frequencies. The frequency at which the transition from f^{-4} to f^{-6} behavior occurs is given by the newest timescale parameter τ_s via

$$f_{4,6} = \frac{1}{2\pi\tau_s}. \tag{2.43}$$

We combine Equation 2.38 with the simplified Langevin equation to derive a single, continuous-autoregressive equation that describes the deviation of the axial dipole moment away from its time average,

$$
\begin{aligned}
&\frac{d^3\varphi'}{dt^3} + \left(\frac{1}{\tau_l} + \frac{1}{\tau_m} + \frac{1}{\tau_s}\right)\frac{d^2\varphi'}{dt^2} \\
&+\left(\frac{1}{\tau_l\tau_m} + \frac{1}{\tau_l\tau_s} + \frac{1}{\tau_m\tau_s}\right)\frac{d\varphi'}{dt} \\
&+\left(\frac{1}{\tau_l\tau_m\tau_s}\right)\varphi'(t) = \frac{\sqrt{D_{eq}}}{\tau_m\tau_s}\zeta(t).
\end{aligned}
\tag{2.44}
$$

2.2 Discrete Stochastic Simulations

We have two fundamentally different stochastic differential equations - the nonlinear Langevin equation and the linear autoregressive equation. The assumptions

$$
v(\varphi(t)) \equiv \frac{-\varphi'(t)}{\tau_l} \qquad \text{and} \qquad D(\varphi(t)) \equiv D_{eq} \tag{2.45}
$$

made in Section 2.1.1 linearize the Langevin system, transforming it into an autoregressive equation. Technically, these assumptions hold true only when the axial dipole moment is near its time average, $\bar{\varphi}(t)$ [Buffett et al., 2013]. [7] To assess whether these assumptions are fair, we compare realizations of

---

[7] They also come directly from applying the Kramers-Moyal equations to PADM2M (with results shown in Figure 1.10) and have not been verified with other datasets or time-varying global field models.

the nonlinear Langevin equation with realizations of the corresponding linear autoregressive equation. To generate these simulations we must discretize the temporal evolution in the Langevin equation.

2.2.1 Discretizing the Langevin Equation

The Langevin equation is

$$\frac{d\varphi}{dt} = v(\varphi(t)) + \sqrt{D(\varphi(t))}\Gamma(t). \tag{2.46}$$

Applying Euler's discretization method like

$$\frac{\varphi(t + \Delta t) - \varphi(t)}{\Delta t} \approx v(\varphi(t)) + \sqrt{D(\varphi(t))}\Gamma(t) \tag{2.47}$$

$$\implies \varphi(t + \Delta t) \approx v(\varphi(t))\Delta t + \sqrt{D(\varphi(t))}\Gamma(t)\Delta t + \varphi(t) \tag{2.48}$$

$$\implies \varphi_{t+1} = v(\varphi_t)\Delta t + \sqrt{D(\varphi_t)}\Gamma_t\Delta t + \varphi_t \tag{2.49}$$

yields a discrete Langevin equation. This process requires an arbitrary seed, φ_1. At each time t we draw values of $\{v(\varphi_t)$ and $D(\varphi_t)\}$ from curves generated by Buffett et. al. (2013), who estimate the drift and diffusion coefficient from PADM2M [Buffett et al., 2013]. Δt must be smaller than the smallest timescale of our model. For example, if we choose an AR2 model for the axial dipole moment, $\Delta t < \tau_m$. $\{\Gamma_t\}$ is a numerical realization of the diffusion process.

$\Gamma(t)$ and $\varphi'(t)$ are both described by linear, autoregressive equations [8]. The former is fed into Equation 2.49 while realizations of the latter are compared with those of Equation 2.49. We could use Euler's method to discretize these linear, autoregressive equations for $\Gamma(t)$ and $\varphi'(t)$. However, Euler's method, in which the derivative is approximated by the slope of the line between one point ahead and the current point, is less accurate than a trapezoidal sum approximation in which the derivative is approximated by the slope of the line between one point ahead and one point behind the current point. The difference is plotted in Figure 2.9.

---

[8] From now on, when we say "autoregressive", we will always mean "continuous autoregressive".

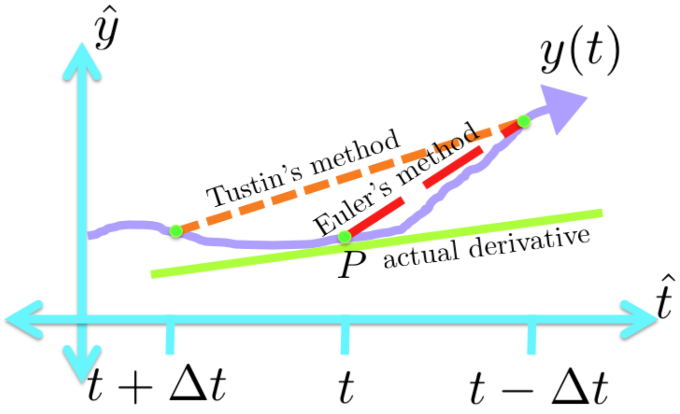

Figure 2.9: Tustin's and Euler's approximations to the derivative of a continuous process, $y(t)$, at time t. The slope of the line from Tustin's method (orange) is much closer to the actual derivative (i.e. the slope of the green line) than the slope of the line due to Euler's method (red).

Since we plan to evaluate our model's accuracy within frequency domain anyway, we can alternatively build a recursive digital filter whose frequency distribution matches that of our continuous process. [9] This is called Tustin's method and is technically equivalent to a trapezoidal approximation to the derivative rather than the forward difference in Euler's method. The basic idea is to find the ratio between the frequency response of the output to the response of the input (white noise) in our continuous model, and construct a discrete filter with the same frequency response ratio between output and input signals. Appendix C contains a full derivation for Tustin's method. We discretize the autoregressive equations for $\Gamma(t)$ and for $\varphi'(t)$ using both methods and compare the results.

---

[9] A digital filter is a discrete equation that mimics our continuous process; Euler's method is indeed a digital filter, but mimics the continuous process perhaps a little less accurately than other digital filters. To build a better filter, we consider frequency domain analysis.

2.2.2 Implementing the discretization for AR1

$\Gamma(t)$

Suppose that the diffusion is uncorrelated, Gaussian-distributed noise with variance 2 that satisfies the equation

$$\Gamma(t) = \zeta(t). \tag{2.50}$$

To simulate this in the discrete time domain, we generate a sequence of Gaussian-distributed random deviates, $\Gamma_t = \zeta_t$, with variance 2.

$\varphi'(t)$

When the diffusion is a random process, the deviation of the axial dipole moment φ' is an order-1 autoregressive process that satisfies Equation 2.14,

$$\frac{d\varphi'}{dt} + \frac{1}{\tau_l}\varphi'(t) = \sqrt{D_{eq}}\zeta(t) \tag{2.51}$$

where τ_l is the drift timescale and the diffusion has no autocorrelation timescale.

Euler's Method The derivative in Equation 2.51 can be approximated by

$$\frac{\varphi'(t+\Delta t) - \varphi'(t)}{\Delta t} \approx \sqrt{D_{eq}}\zeta(t) - \frac{1}{\tau_l}\varphi'(t) \tag{2.52}$$

$$\varphi'_{t+1} = \sqrt{D_{eq}}\Delta t \zeta_t + (1 - \frac{\Delta t}{\tau_l})\varphi'_t. \tag{2.53}$$

This process requires an arbitrary seed, φ'_1.

Tustin's Method The Laplace transform of Equation 2.51 is

$$\left(s\tilde{\varphi}'(s) - \varphi'(0)\right) + \frac{1}{\tau_l}\tilde{\varphi}'(s) = \sqrt{D_{eq}}\tilde{\zeta}(s). \tag{2.54}$$

If we assume that $\varphi'(0) = 0$, then the ratio between output and input is

$$\tilde{g}(s) \equiv \frac{\tilde{\varphi}'(s)}{\tilde{\zeta}(s)} = \frac{\sqrt{D_{eq}}}{s + \frac{1}{\tau_l}}. \tag{2.55}$$

$\tilde{g}(s)$ is called the "transfer function" and describes the frequency response of the output to that of the input process. $\tilde{g}(s)$ describes the frequency responses of continuous signals. To transform this into a description of the frequency responses of discrete signals, we apply the bilinear transformation

$$s = \Big(\frac{2}{\Delta t}\Big)\Big(\frac{z-1}{z+1}\Big) \tag{2.56}$$

and obtain

$$\tilde{g}(z) = \frac{\sqrt{D_{eq}}\Delta t(z+1)}{(\frac{\Delta t}{\tau_l}+2)z + (\frac{\Delta t}{\tau_l}-2)}. \tag{2.57}$$

A digital filter looks like

$$\sum_{k=0}^{K-1} \alpha_k \varphi'_{n-k} = \sum_{l=0}^{L-1} \beta_l \zeta_{n-l} \tag{2.58}$$

and has the associated transfer function

$$\tilde{g}(z) = \frac{\sum_{l=0}^{L-1} \beta_l z^{-l}}{\sum_{k=0}^{K-1} \alpha_k z^{-k}}. \tag{2.59}$$

Expanding Equation 2.59 and comparing with Equation 2.57, we infer that

$$
\begin{aligned}
\beta_0 = \sqrt{D_{eq}}\Delta t \quad \beta_1 = \sqrt{D_{eq}}\Delta t \\
\alpha_0 = \frac{\Delta t}{\tau_l} + 2 \quad \alpha_1 = \frac{\Delta t}{\tau_l} - 2
\end{aligned}
\tag{2.60}
$$

and $\{\beta_j, \alpha_j\} = 0 \quad \forall \quad j \geq 2$. Placing these coefficients into the digital filter and letting $n = t + 1$ to keep a forward-difference form consistent with Euler's method, we obtain

$$
\implies \varphi'_{t+1} = \frac{\beta_0 \zeta_{t+1} + \beta_1 \zeta_t - \alpha_1 \varphi'_t}{\alpha_0}. \tag{2.61}
$$

We assumed that $\varphi'(0) = 0$, so this process requires the mandatory seed $\varphi'_1 = 0$.

2.2.3 Implementing the discretization for AR2

$\Gamma(t)$

Suppose that the diffusion $\Gamma(t)$ is a singly-correlated, order-1 autoregressive process that satisfies Equation 2.22,

$$
\tau_m \frac{d\Gamma}{dt} + \Gamma(t) = \zeta(t) \tag{2.62}
$$

where τ_m is its autocorrelation timescale.

Euler's Method The derivative in Equation 2.62 can be approximated by

$$\implies \frac{\Gamma(t+\Delta t)-\Gamma(t)}{\Delta t} \approx \frac{\zeta(t)-\Gamma(t)}{\tau_m} \tag{2.63}$$

$$\implies \Gamma_{t+1} \equiv \zeta_t\frac{\Delta t}{\tau_m} + \Gamma_t(1-\frac{\Delta t}{\tau_m}). \tag{2.64}$$

This process requires an arbitrary seed, Γ_1.

Tustin's Method The Laplace transform of Equation 2.62 is

$$\tau_m\Big(s\tilde{\Gamma}(s)-\Gamma(0)\Big)+\tilde{\Gamma}(s)=\tilde{\zeta}(s). \tag{2.65}$$

If we assume that $\Gamma(0)=0$, then the transfer function is

$$\tilde{g}(s)=\frac{1}{\tau_m s+1}. \tag{2.66}$$

Applying the bilinear transformation, we derive the discrete transfer function

$$\tilde{g}(z) = \frac{(\Delta t)z + (\Delta t)}{(\Delta t + 2\tau_m)z + (\Delta t - 2\tau_m)}. \tag{2.67}$$

Comparing this with the transfer function of a digital filter, we obtain that

$$\begin{aligned} \beta_0 &= \Delta t \qquad & \beta_1 &= \Delta t \\ \alpha_0 &= \Delta t + 2\tau_m \qquad & \alpha_1 &= \Delta t - 2\tau_m \end{aligned} \tag{2.68}$$

and $\{\beta_j, \alpha_j\} = 0 \quad \forall \quad j \geq 2$. The digital filter is then

$$\implies \Gamma_{t+1} = \frac{\Delta t}{\Delta t + 2\tau_m}(\zeta_{t+1} + \zeta_t) + \frac{2\tau_m - \Delta t}{2\tau_m + \Delta t}\Gamma_t, \tag{2.69}$$

where we have let $n = t + 1$ to keep a forward-difference form consistent with Euler's method. We assumed that $\Gamma(0) = 0$ so this process requires the mandatory seed $\Gamma_1 = 0$.

$\varphi'(t)$

When the diffusion is an order-1 autoregressive process, the deviation of the axial dipole moment φ' is an order-2 autoregressive process that satisfies Equation 2.27,

$$\tau_m \frac{d^2\varphi'}{dt^2} + (\frac{\tau_m}{\tau_l} + 1)\frac{d\varphi'}{dt} + \frac{1}{\tau_l}\varphi'(t) = \sqrt{D_{eq}}\zeta(t) \tag{2.70}$$

where τ_m is the diffusion autocorrelation timescale and τ_l is the drift timescale.

Euler's Method Let

$$\frac{d\varphi'}{dt} = z(t) \tag{2.71}$$

$$\implies \varphi'_{t+1} \approx z_t \Delta t + \varphi'_t. \tag{2.72}$$

Then Equation 2.70 becomes

$$\tau_m \frac{dz}{dt} + (\frac{\tau_m}{\tau_l} + 1)z(t) + \frac{1}{\tau_l}\varphi'(t) = \sqrt{D_{eq}}\zeta(t) \tag{2.73}$$

$$\implies z_{t+1} = \frac{\sqrt{D_{eq}}\Delta t}{\tau_m}\zeta_t + (1 - \frac{\Delta t}{\tau_l} - \frac{\Delta t}{\tau_m})z_t - \frac{\Delta t}{\tau_l \tau_m}\varphi'_t. \tag{2.74}$$

Equations 2.72 and 2.74 are coupled and this process requires arbitrary seeds $\{\varphi'_1, z_1\}$.

Tustin's Method The Laplace transform of Equation 2.70 is

$$\begin{aligned} \tau_m \Big(s^2 \tilde{\varphi}'(s) - s\varphi'(0) - \frac{d\varphi'}{dt}\Big|_{t=0} \Big) \\ +(\frac{\tau_m}{\tau_l} + 1)\Big(s\tilde{\varphi}'(s) - \varphi'(0) \Big) \\ +\frac{1}{\tau_l}\Big(\tilde{\varphi}'(s) \Big) = \sqrt{D_{eq}}\tilde{\zeta}(s). \end{aligned} \tag{2.75}$$

If we assume that $\varphi'(0) = 0 = \frac{d\varphi'}{dt}\Big|_{t=0}$ and apply the bilinear transformation, the discrete transfer function is

$$\tilde{g}(z) = \frac{\sqrt{D_{eq}}\Delta t^2 (z^2 + 2z + 1)}{\Big(4\tau_m + 2\Delta t(\frac{\tau_m}{\tau_l} + 1) + \frac{\Delta t^2}{\tau_l} \Big) z^2 + \Big(-8\tau_m + \frac{2\Delta t^2}{\tau_l} \Big) z + \Big(4\tau_m - 2\Delta t(\frac{\tau_m}{\tau_l} + 1) + \frac{\Delta t^2}{\tau_l} \Big)}. \tag{2.76}$$

Comparing this with the transfer function of a digital filter, we obtain that

$$\begin{aligned} \beta_0 = \Delta t^2\sqrt{D_{eq}} \quad \beta_1 = 2\Delta t^2\sqrt{D_{eq}} \quad \beta_2 = \Delta t^2\sqrt{D_{eq}} \\ \alpha_0 = 4\tau_m + 2\Delta t(\frac{\tau_m}{\tau_l}+1) + \frac{\Delta t^2}{\tau_l} \quad \alpha_2 = 4\tau_m - 2\Delta t(\frac{\tau_m}{\tau_l}+1) + \frac{\Delta t^2}{\tau_l} \\ \alpha_1 = -8\tau_m + \frac{2\Delta t^2}{\tau_l} \end{aligned} \tag{2.77}$$

and $\{\beta_j, \alpha_j\} = 0 \quad \forall \quad j \geq 3$. The digital filter is

$$\implies \varphi'_{t+2} = \frac{\beta_0\zeta_{t+2} + \beta_1\zeta_{t+1} + \beta_2\zeta_t - \alpha_1\varphi'_{t+1} - \alpha_2\varphi'_t}{\alpha_0}. \tag{2.78}$$

and we assumed that $\varphi'(0) = 0 = \frac{d\varphi'}{dt}\Big|_{t=0}$, indicating that this process requires the mandatory seeds $\{\varphi'_1, \varphi'_2\} = 0$.

2.2.4 Implementing the discretization for AR3

$\Gamma(t)$

Suppose that the diffusion $\Gamma(t)$ is a doubly-correlated, order-2 autoregressive process that satisfies Equation 2.38,

$$\tau_m\tau_s\frac{d^2\Gamma}{dt^2} + \tau_m\tau_s(\frac{1}{\tau_m} + \frac{1}{\tau_s})\frac{d\Gamma}{dt} + \Gamma(t) = \zeta(t) \tag{2.79}$$

where $\{\tau_m, \tau_s\}$ are its autocorrelation timescales.

Euler's Method Let

$$\frac{d\Gamma}{dt} = u(t) \tag{2.80}$$

$$\implies \Gamma_{t+1} = u_t\Delta t + \Gamma_t. \tag{2.81}$$

Then Equation 2.79 yields

$$u_{t+1} \approx \frac{\Delta t}{\tau_m\tau_s}\zeta_t + \Big(1 - (\frac{\Delta t}{\tau_m} + \frac{\Delta t}{\tau_s})\Big)u_t - \frac{\Gamma_t\Delta t}{\tau_m\tau_s} \tag{2.82}$$

Equations 2.81 and 2.82 are coupled and this process requires arbitrary seeds, $\{\Gamma_1, u_1\}$.

Tustin's Method The Laplace transform of Equation 2.79 is

$$\tau_m\tau_s\Big(s^2\tilde{\Gamma}(s) - s\Gamma(0) - \frac{d\Gamma}{dt}\Big|_{t=0}\Big) + \tau_m\tau_s(\frac{1}{\tau_m} + \frac{1}{\tau_s})\Big(s\tilde{\Gamma}(s) - \Gamma(0)\Big) + \tilde{\Gamma}(s) = \tilde{\zeta}(s). \tag{2.83}$$

If we assume that $\Gamma(0) = 0 = \frac{d\Gamma}{dt}\Big|_{t=0}$, apply the bilinear transformation, and compare the discrete transfer function with the transfer function of a digital filter, we obtain that

$$\begin{aligned} \beta_0 = \Delta t^2 \qquad \beta_1 = 2\Delta t^2 \qquad \beta_2 = \Delta t^2 \\ \alpha_0 = 4\tau_m\tau_s + 2\Delta t\tau_m\tau_s(\frac{1}{\tau_m} + \frac{1}{\tau_s}) + \Delta t^2 \\ \alpha_1 = -8\tau_m\tau_s + 2\Delta t^2 \\ \alpha_2 = 4\tau_m\tau_s - 2\Delta t\tau_m\tau_s(\frac{1}{\tau_m} + \frac{1}{\tau_s}) + \Delta t^2 \end{aligned} \tag{2.84}$$

and $\{\beta_j, \alpha_j\} = 0 \quad \forall \quad j \geq 3$. The digital filter is

$$\Gamma_{t+2} = \frac{\beta_0\zeta_{t+2} + \beta_1\zeta_{t+1} + \beta_2\zeta_t - \alpha_1\Gamma_{t+1} - \alpha_2\Gamma_t}{\alpha_0}. \tag{2.85}$$

We assumed that $\Gamma(0) = 0$ and $\left.\frac{d\Gamma}{dt}\right|_{t=0} = 0$ so this process requires the mandatory seeds $\{\Gamma_1, \Gamma_2\} = 0$.

$\varphi'(t)$

When the diffusion is an order-2 autoregressive process, the deviation of the axial dipole moment φ' is an order-3 autoregressive process that satisfies Equation 2.44,

$$\begin{aligned}\frac{d^3\varphi'}{dt^3} + \left(\frac{1}{\tau_l} + \frac{1}{\tau_m} + \frac{1}{\tau_s}\right)\frac{d^2\varphi'}{dt^2} \\ + \left(\frac{1}{\tau_l\tau_m} + \frac{1}{\tau_l\tau_s} + \frac{1}{\tau_m\tau_s}\right)\frac{d\varphi'}{dt} \\ + \left(\frac{1}{\tau_l\tau_m\tau_s}\right)\varphi'(t) = \frac{\sqrt{D_{eq}}}{\tau_m\tau_s}\zeta(t)\end{aligned} \tag{2.86}$$

where $\{\tau_m, \tau_s\}$ are the diffusion autocorrelation timescales and τ_l is the drift timescale.

Euler's Method Let

$$\frac{d\varphi'}{dt} = w(t) \qquad \text{and} \qquad \frac{d^2\varphi'}{dt^2} = \frac{dw}{dt} = v(t). \tag{2.87}$$

Then Equation 2.86 gives

$$\varphi'_{t+1} = w_t \Delta t + \varphi'_t \quad \text{and} \quad w_{t+1} \approx v_t \Delta t + w_t \tag{2.88}$$

while

$$\begin{aligned}\implies v_{t+1} \approx {} & \frac{\sqrt{D_{eq}}\Delta t}{\tau_m \tau_s}\zeta_t + v_t\left(1 - (\frac{\Delta t}{\tau_l} + \frac{\Delta t}{\tau_m} + \frac{\Delta t}{\tau_s})\right) \\ & -\left(\frac{\Delta t}{\tau_l \tau_m} + \frac{\Delta t}{\tau_l \tau_s} + \frac{\Delta t}{\tau_m \tau_s}\right) w_t - \left(\frac{\Delta t}{\tau_l \tau_m \tau_s}\right)\varphi'_t\end{aligned} \tag{2.89}$$

All three parts of Equations 2.88 and 2.89 are all coupled and this process requires the arbitrary seeds, $\{\varphi'_1, w_1, v_1\}$.

Tustin's Method We take the Laplace transform of Equation 2.86, suppose that the initial conditions are zero, apply the bilinear transformation, and compare the discrete transfer function to that of a digital filter and obtain that

$$
\begin{aligned}
b_1 &= \tau_m \tau_s \\
b_2 &= \Delta t \tau_m \tau_s (\frac{1}{\tau_l} + \frac{1}{\tau_m} + \frac{1}{\tau_s}) \\
b_3 &= \Delta t^2 \tau_m \tau_s (\frac{1}{\tau_l \tau_m} + \frac{1}{\tau_l \tau_s} + \frac{1}{\tau_m \tau_s}) \\
b_4 &= \frac{\Delta t^3}{\tau_l}
\end{aligned}
\tag{2.90}
$$

where

$$
\begin{aligned}
\beta_0 = \Delta t^3 \sqrt{D_{eq}} \quad & \beta_1 = 3\Delta t^3 \sqrt{D_{eq}} \\
\beta_2 = 3\Delta t^3 \sqrt{D_{eq}} \quad & \beta_3 = \Delta t^3 \sqrt{D_{eq}} \\
\alpha_0 &= 8b_1 + 4b_2 + 2b_3 + b_4 \\
\alpha_1 &= -24b_1 - 4b_2 + 2b_3 + 3b_4 \\
\alpha_2 &= 24b_1 - 4b_2 - 2b_3 + 3b_4 \\
\alpha_3 &= -8b_1 + 4b_2 - 2b_3 + b_4
\end{aligned}
\tag{2.91}
$$

and $\{\beta_j, \alpha_j\} = 0 \quad \forall \quad j \geq 4$. The digital filter is

$$
\varphi'_{t+3} = \frac{\beta_0 \zeta_{t+3} + \beta_1 \zeta_{t+2} + \beta_2 \zeta_{t+1} + \beta_3 \zeta_t - \alpha_1 \varphi'_{t+2} - \alpha_2 \varphi'_{t+1} - \alpha_3 \varphi'_t}{\alpha_0}. \tag{2.92}
$$

We assumed that $\{\varphi'(0), \frac{d\varphi'}{dt}\Big|_{t=0}, \frac{d^2\varphi'}{dt^2}\Big|_{t=0}\} = 0$ so this process requires the mandatory seeds $\{\varphi'_1, \varphi'_2, \varphi'_3\} = 0$.

2.3 Estimating AR Model Parameters

The composite geomagnetic spectrum in Figure 1.17 was built to describe the axial dipole field, $g_1^0(t)$, rather than the axial dipole moment, $\varphi(t)$ [Panovska et al., 2018]. The two quantities are related by Equation 1.8,

$$g_1^0(t) = \frac{\mu_0 \varphi(t)}{4\pi a^3}, \tag{2.93}$$

where $\mu_0 = 4\pi \cdot 10^{-7} \frac{Tm}{A}$ is the magnetic permeability in a vacuum and $a = 6.3781 \cdot 10^6 m$ is Earth's radius. If we want a composite spectrum describing $\varphi(t)$ rather than $g_1^0(t)$, we can scale the spectrum of Panovska et al. (2018) by the proportionality presented in Equation 2.93. Assuming that $g_1^0(t)$ and $\varphi(t)$ have been measured in μT and $10^{22} Am^2$, respectively [10], we obtain the proportionality constant

$$2.5946 \mu T = 1 \cdot 10^{22} Am^2. \tag{2.94}$$

Using Equation 2.94 to scale Figure 1.17 from $\mu T^2 Myr$ to $10^{44} A^2 m^4 Myr$ produces Figure 2.10. We illustrate the sequence of spectral regimes in Figure

---

[10] The former units have been chosen so we may easily compare our model results for the axial dipole moment $\varphi(t)$ to models from previous studies [Buffett et al., 2013].

2.11 by placing straight, colored lines on top of the composite curve. A dark blue arrow in Figure 2.11 points out a flattening in the frequency spectrum of GGF100k [Panovska et al., 2018] that is *not* predicted by our models. The dashed, black line in Figure 2.11 marks the f^{-2} regime that *is* predicted by our models. Note that the dashed, black lines in Figure 1.17 indicate frequency regimes associated with various types of secular variation and do not mark the transition frequencies between adjacent spectral regimes. In contrast, dashed, turquoise lines do mark the transition frequencies in Figure 2.11.

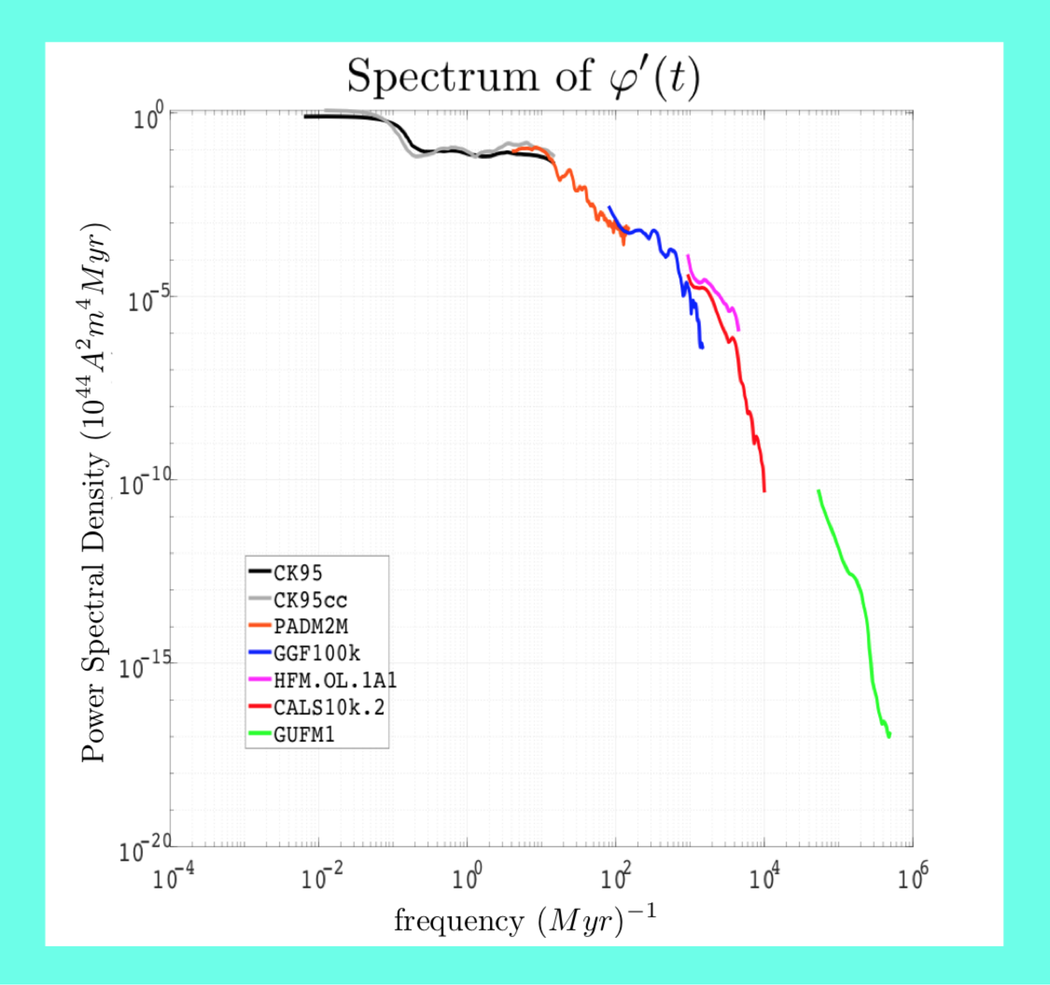

Figure 2.10: A composite spectrum for the geomagnetic axial dipole moment, modified from the composite geomagnetic spectrum of Panovska et al. (2018).

Finally, note that the composite spectrum for $\varphi(t)$ in Figure 2.10 is plotted on a logarithmic scale and has a jump at frequencies below $2 \cdot 10^{-1}$ Myr^{-1}. This jump is predicted to be caused by changes in reversal rate and is not predicted by any of our AR models. We therefore make a simplifying assumption that the f^0 regime at frequencies between $[2 \cdot 10^{-1}, 2 \cdot 10^1]$ Myr^{-1} in Figure 2.10 extends all the way to the left until $f = 0$. [11] We illustrate this assumption as a grey line in Figure 2.11.

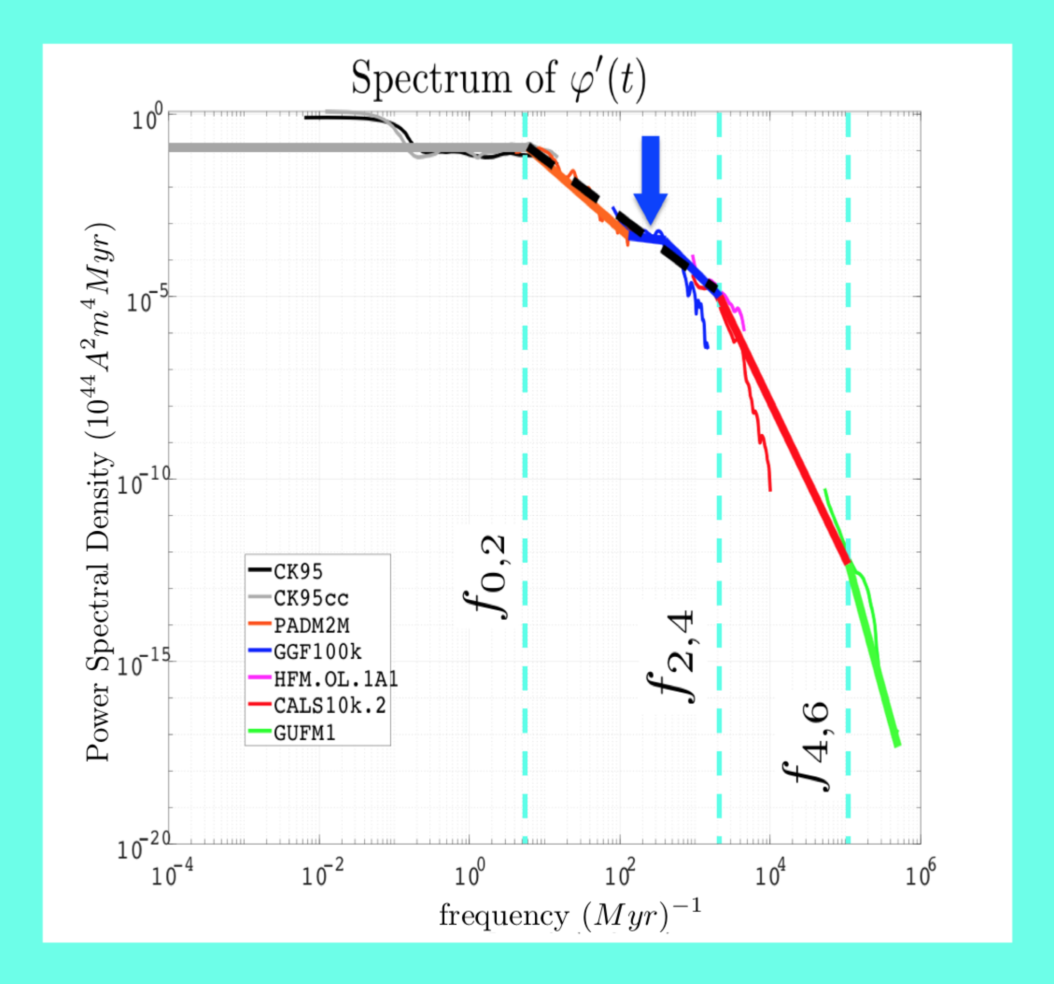

Figure 2.11: Thick grey, black (dashed), green, and red lines indicate f^0, f^{-2}, f^{-4} and f^{-6} regimes, respectively.

---

[11] We discover later that the non-linearity in the Langevin equation is responsible for the jump.

We are ready to estimate our AR model parameters. We want the transitions between successive spectral regimes in our AR model spectra to occur at the same locations as the transitions in Figure 2.11. As explained in Sections 2.1.3, 2.1.4 and 2.1.5, the timescale parameters of our AR models are directly related to the transition frequencies between successive spectral regimes via

$$\begin{aligned} f_{0,2} &= \frac{1}{2\pi\tau_l} \\ f_{2,4} &= \frac{1}{2\pi\tau_m} \\ f_{4,6} &= \frac{1}{2\pi\tau_s}. \end{aligned} \tag{2.95}$$

We inspect Figure 2.11, infer values for $\{f_{0,2}, f_{2,4}, f_{4,6}\}$ from the dashed, turquoise lines, and compute $\{\tau_l, \tau_m, \tau_l\}$ via Equation 2.95. To compute D_{eq}, we notice that the model spectra for all three AR orders reduces to

$$S_{\varphi'}(0) = 2D_{eq}\tau_l^2 \tag{2.96}$$

at $f = 0$. We use Equation 2.96 to compute D_{eq} assuming that $S_{\varphi'}(0)$ can be taken directly as the height of the grey line in Figure 2.11.

2.4 Results

Table 2.1 lists the transition frequencies in Figure 2.11 estimated by visual inspection and Table 2.2 lists the corresponding model parameters. The value obtained for the zero-frequency power (i.e. height of the grey line) in Figure 2.11 was

$$S_{\varphi'}(0) = 0.1346\ 10^{44} A^2 m^4\ Myr. \tag{2.97}$$

Table 2.1: Transition frequencies between spectral regimes in the composite geomagnetic spectrum.

Transition Frequency	Estimated Value
$f_{0,2}$	$5.5 \cdot 10^0 Myr^{-1}$
$f_{2,4}$	$2 \cdot 10^3 Myr^{-1}$
$f_{4,6}$	$1 \cdot 10^5 Myr^{-1}$

Table 2.2: Our AR model parameters.

Parameter	Estimated Value
τ_l	28900 yr
τ_m	79.5775 yr
τ_s	1.5915 yr
D_{eq}	$80.5785\ 10^{44} \frac{A^2 m^4}{Myr}$

Table 2.4 lists the various types of numerical simulations produced for each model order. From now on we call each type of simulation produced a "discrete process" to make our discussion easier. We produced a suite of realizations for each discrete process listed in Table 2.4 using the parameters in Table 2.2. For each discrete process, the variance of every realization was computed and then all of the variances were averaged together, producing a mean variance value across all realizations of the discrete process. For each discrete process, we generated a prolate-tapered spectrum for every realization and then averaged all of the realization spectra together. This produced a mean empirical spectrum across all realizations of the process. A flowchart for the code built to do all of this is provided in Appendix E.

For each AR order, Figure 2.12 juxtaposes the theoretical model variance, computed using the parameters from Table 2.2 and the formulas presented in column 3 of Table 2.3, with the mean variance of each discrete process.

Figures 2.13 through 2.15 show the mean empirical spectrum of each discrete process against the model spectrum, for each AR order. Figure 2.16 shows all three AR model spectra against the composite geomagnetic spectrum of Figure 1.17. The composite geomagnetic spectrum is shown in blue and our AR model spectra are shown in pink, green, and red for orders 1, 2, and 3 respectively.

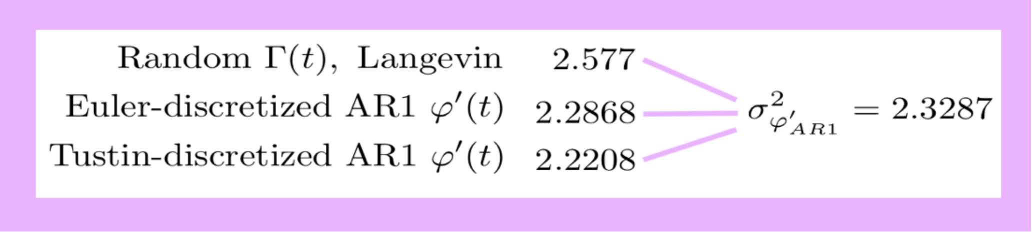

(a) AR1 model variance compared with mean variance of each discrete process for AR1 model.

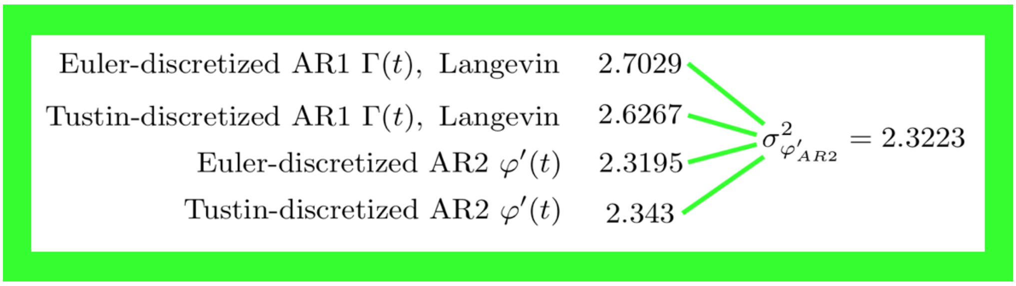

(b) AR2 model variance compared with mean variance of each discrete process for AR2 model.

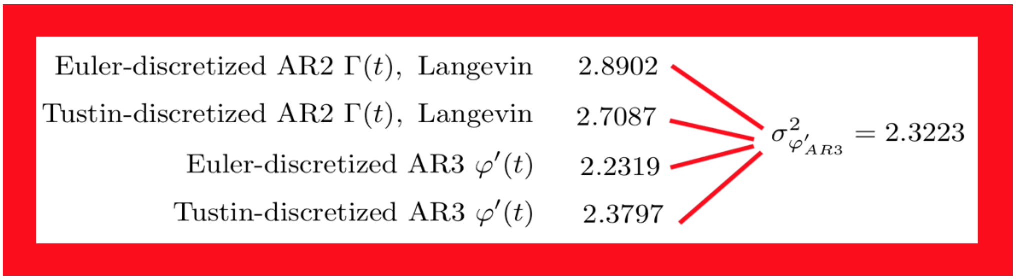

(c) AR3 model variance compared with mean variance of each discrete process for AR3 model.

Figure 2.12: AR model variances versus discrete process variances.

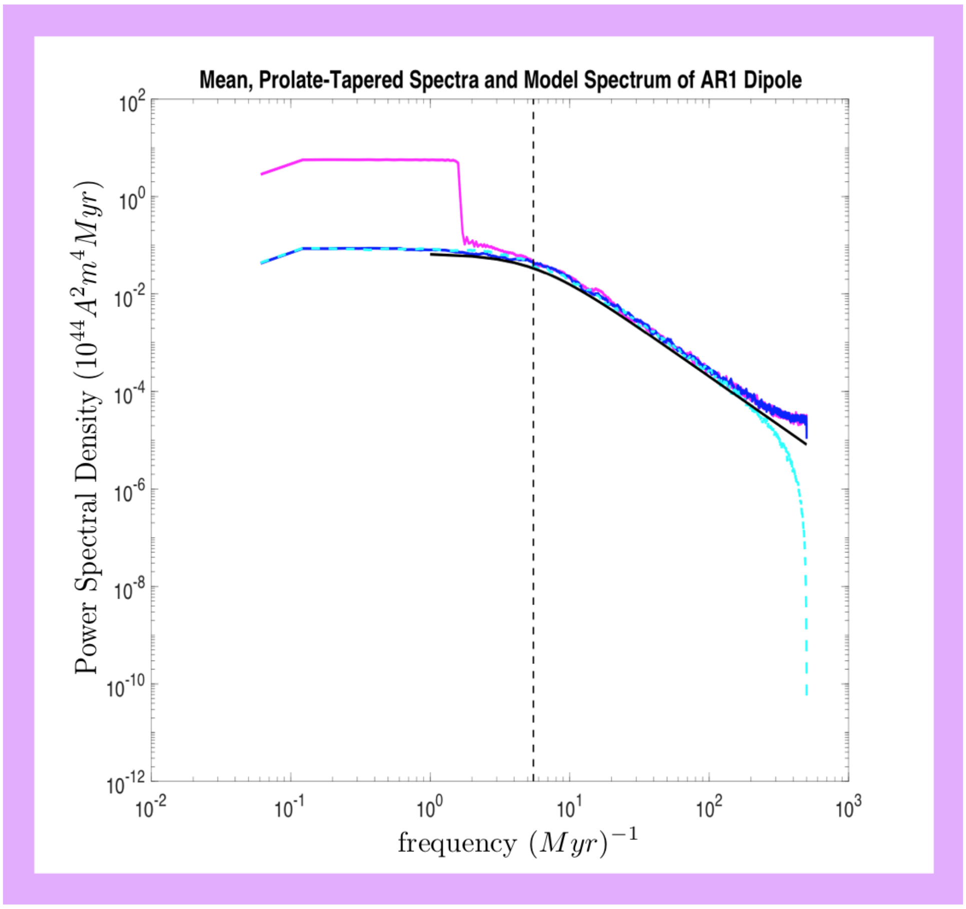

(a)

■ Random $\Gamma(t)$, Langevin

■ Euler-discretized AR1 $\varphi'(t)$

■ Tustin-discretized AR1 $\varphi'(t)$

■ AR1 Model Spectrum

(b)

Figure 2.13: Prolate-tapered spectral estimates corresponding to realizations of the Langevin process with uncorrelated $\Gamma(t)$ and to realizations of the AR1 process.

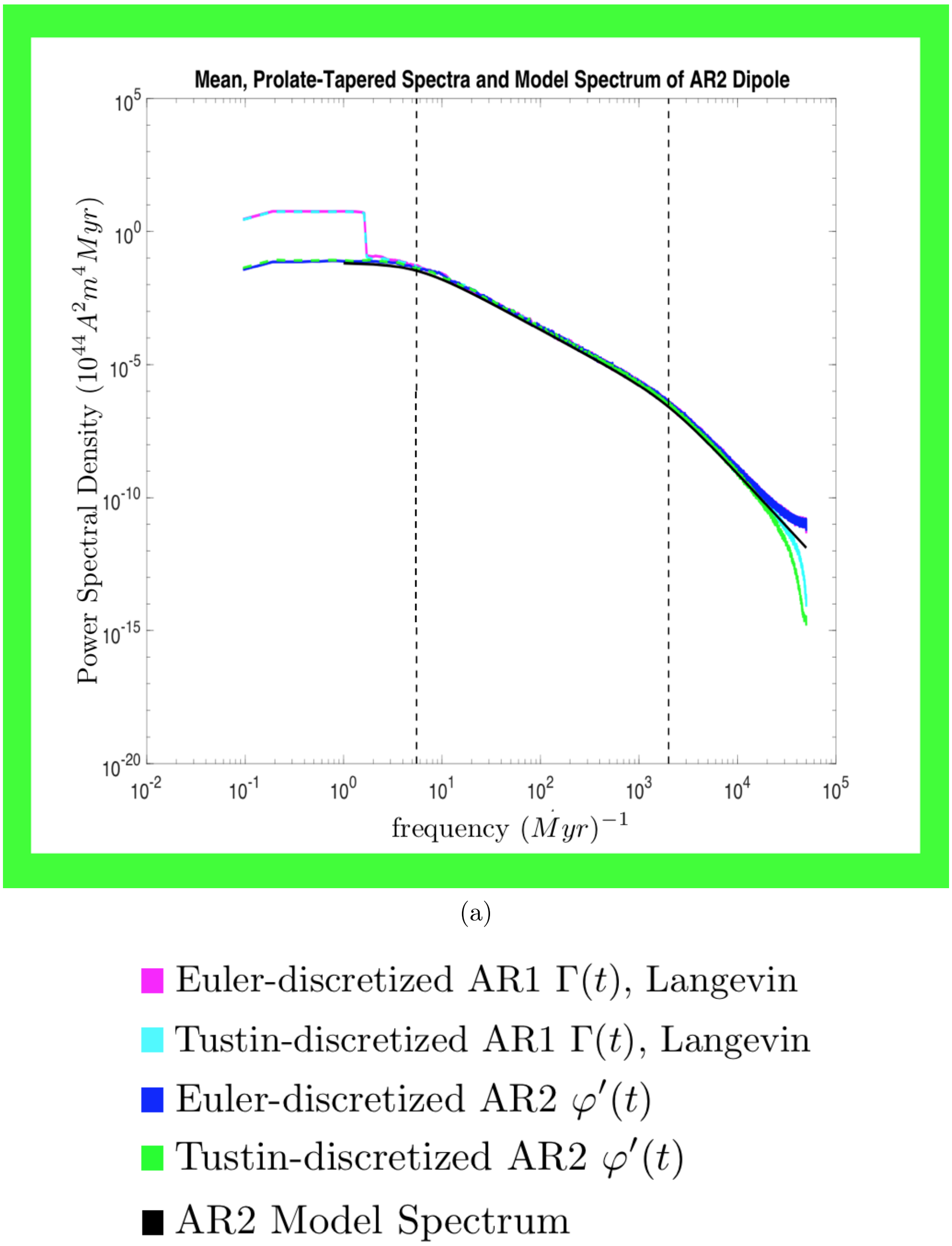

(a)

(b)

Figure 2.14: Prolate-tapered spectral estimates pertaining to realizations of the Langevin process, now with singly-correlated, AR1 $\Gamma(t)$, and to realizations of the AR2 process.

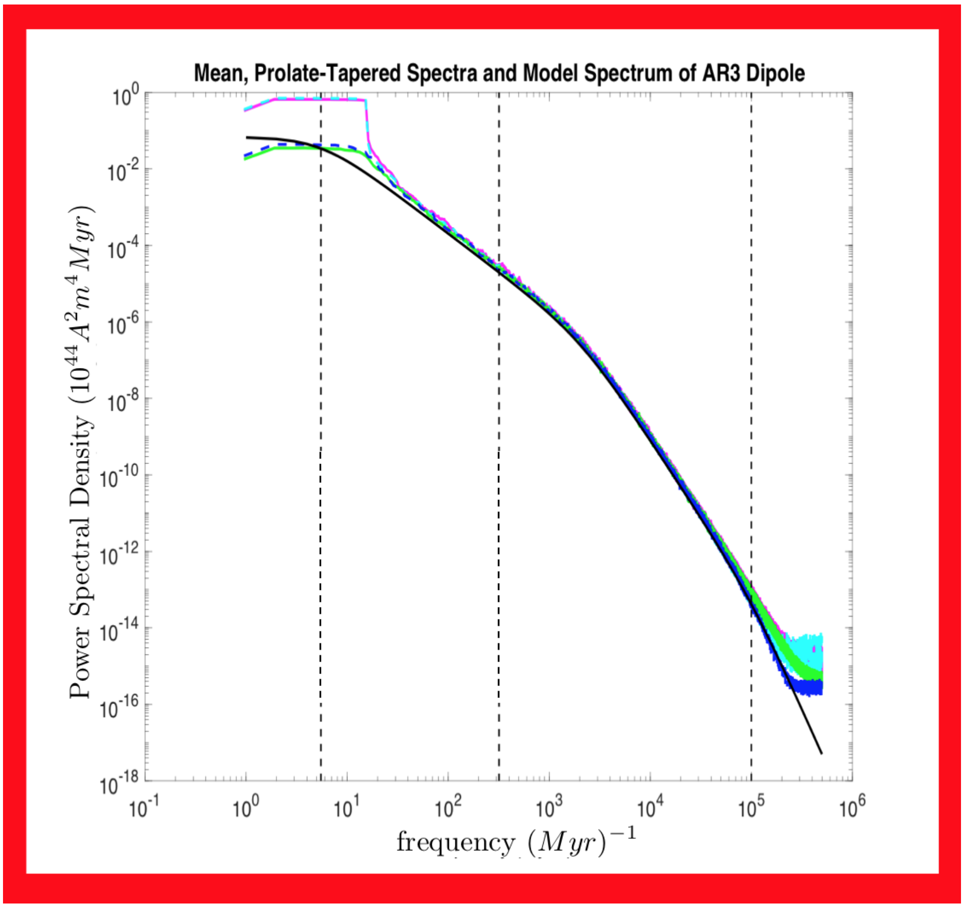

(a)

🟪 Euler-discretized AR2 $\Gamma(t)$, Langevin
🟦 Tustin-discretized AR2 $\Gamma(t)$, Langevin
🟩 Euler-discretized AR3 $\varphi'(t)$
🟦 Tustin-discretized AR3 $\varphi'(t)$
⬛ AR3 Model Spectrum

(b)

Figure 2.15: Prolate-tapered spectral estimates pertaining to realizations of the Langevin process, now with singly-correlated, AR1 $\Gamma(t)$, and to realizations of the AR2 process.

Figure 2.13 shows prolate-tapered spectral estimates corresponding to realizations of the Langevin process with uncorrelated $\Gamma(t)$ show a low-frequency bump similar to that of the composite spectrum. The bump is neither predicted by the AR1 model nor exhibited in the spectral estimates corresponding to realizations of the AR1 process. We do however see the desired transition from f^0 behavior to f^{-2} behavior in all of the curves.

Again, in Figure 2.14 prolate-tapered spectral estimates pertaining to realizations of the Langevin process, now with singly-correlated, AR1 $\Gamma(t)$, exhibit a low-frequency bump like the one in the composite spectrum whereas spectral estimates pertaining to the AR2 process do not. We clearly see the desired transition from f^0 to f^{-2} to f^{-4} regimes with transition frequencies that are consistent across the empirical spectral estimates for all four types of discrete processes and the AR2 model spectrum.

Figure 2.15 displays prolate-tapered spectral estimates for realizations of the Langevin process with doubly-correlated, AR2 $\Gamma(t)$ and for realizations of the AR3 process. The former show a low-frequency bump reminiscent of the one in the composite spectrum. The latter and the AR3 model spectrum both do not show a low-frequency bump. There is a slight discrepancy between the AR3 model spectrum and the empirical spectrum near the first transition frequency, $f_{0,2}$. We expect that this discrepancy is due to loss of frequency resolution due to tapering and averaging procedures built into the Thomson multitaper approach. A full explanation of how this may have occurred is given in Appendix D.

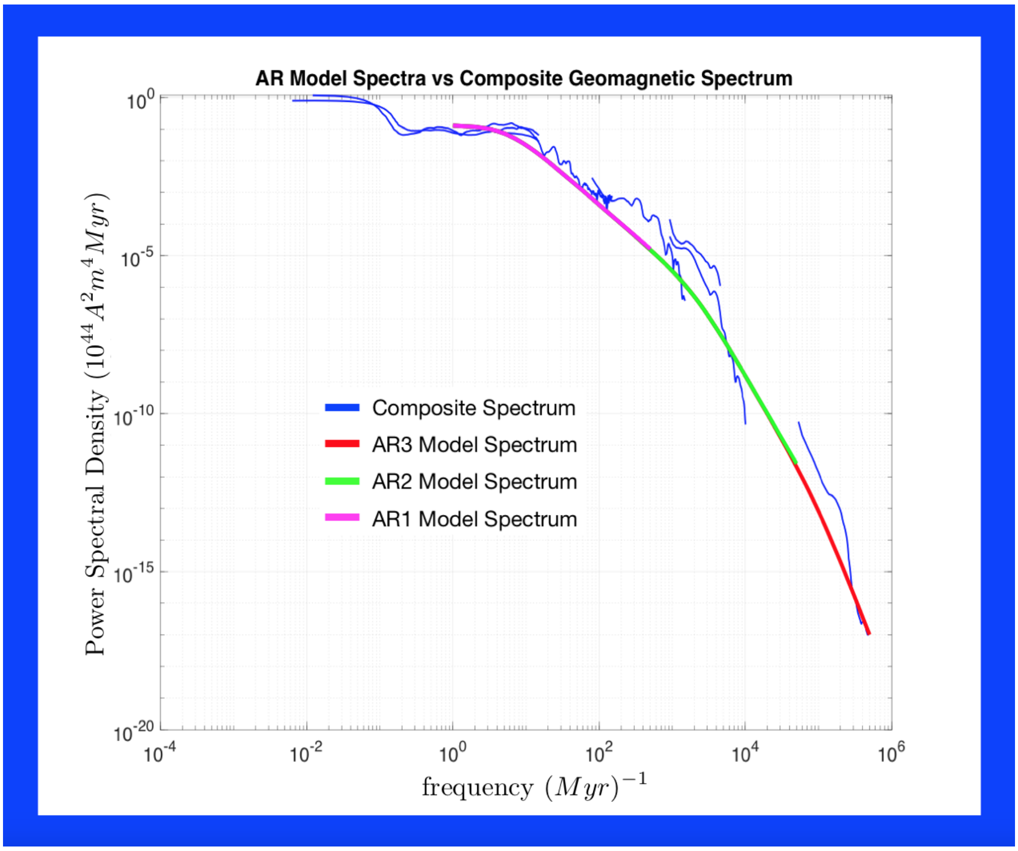

Figure 2.16: Our AR1, AR2, and AR3 model spectra are plotted against the composite spectrum for $\varphi(t)$. The composite spectrum seems to be shallower than the predicted f^{-2} behavior and then seems to be steeper than the predicted f^{-4} and f^{-6} behaviors in the AR model spectra.

2.5 Discussion

2.5.1 A Physical Interpretation of the Model Parameters

The new AR3 model poses some physical implications regarding the dynamics in Earth's outer core. We will investigate each model parameter in Table 2.2 and deduce what its value, obtained by comparing our model with the composite spectrum in Figure 1.17, suggests for the physics of the geodynamo.

Ohmic Diffusion in the Earth's Outer Core

To begin, we analyze our drift timescale, $\tau_l = 28900$ years. This is strikingly close to the theoretical timescale that Ohmic diffusion is expected to operate on in Earth's outer core. The theoretical calculation is derived by considering the magnetic induction equation,

$$\frac{d\vec{B}}{dt} = \nabla \times (\vec{v} \times \vec{B}) + \eta \nabla^2 \vec{B}, \tag{2.98}$$

that describes the temporal variations in the geomagnetic field as a combination of two fundamental processes in Earth's outer core: advection and Ohmic diffusion. In the induction equation, $\vec{v}$ is the velocity and η is the magnetic diffusivity of the outer core fluid.

$$\eta = \frac{1}{\mu_0 \sigma} \tag{2.99}$$

where σ is the electrical conductivity of the outer core fluid and is still not well-constrained for Earth's outer core [Pozzo et al., 2012].

Advection refers to the transportation of magnetic field lines by the outer core fluid as it moves. In fact, Alfven's theorem states that if the outer core fluid had infinite electrical conductivity, which implies $\eta = 0$, the magnetic field lines are frozen to the fluid and move along with it [Backus et al., 1996].

But Earth's outer core is finitely conductive and thus has some electrical resistance. This means that the magnetic field lines passing through the outer core can break away from the fluid flow lines. When they do, the magnetic field lines pass through a finitely resistive fluid and therefore relinquish some of their energy to the environment. The dissipation of energy away from the magnetic field is called Ohmic diffusion.

So advection governs the transportation of magnetic energy, carried in the field lines passing through Earth's outer core, due to the tethering between the flow and field lines described by Alfven's theorem. Meanwhile Ohmic diffusion governs the energy dissipation that occurs because the field lines are not permanently tethered to the flow lines and can break away, releasing energy from the magnetic field.

If η is near 0, the outer core fluid has a strong clutch on magnetic field lines, which take a long time to escape. We expect that Ohmic diffusion occurs over longer timescales than advection in Earth's outer core because the magnetic diffusivity for the outer core is usually estimated to be on the order of $\eta \approx 1$ to $10\frac{m^2}{s}$. To infer the timescale for Ohmic diffusion we first simplify the induction equation by replacing every variable by a scaling parameter like

$$\begin{gathered} dt \to T \\ v \to U \\ \nabla \to \tfrac{1}{L}. \end{gathered}$$

We then estimate the timescale for Ohmic diffusion by considering what would happen if the outer core fluid stopped moving. Then the magnetic induction equation becomes the diffusion equation

$$\frac{d\vec{B}}{dt} = \eta \nabla^2 \vec{B} \tag{2.100}$$

which reduces to an eigenvalue problem with an infinite set of solutions. The nth solution has the form

$$\vec{B}_n(t) \approx \vec{B}_n(\vec{r})e^{-\frac{t}{t_d}} \quad \Big| \quad t_d \propto \frac{c^2}{\eta} \tag{2.101}$$

where $\vec{r} = (r, \theta, \phi)$, c is the outer core radius, a typical length scale across which Ohmic diffusion occurs, and t_d is the e-folding time of magnetic energy in the geodynamo [Backus et al., 1996]. With $\eta \approx 1\frac{m^2}{s}$ and $c \approx 1000$ km, we approximate $t_d \approx 30,000$ years for Earth's outer core. This is *right* in the ballpark of our estimated value for τ_l, which suggests that Ohmic diffusion drives the drift of the axial dipole moment towards its steady state. [12]

MAC Waves in Earth's Outer Core

The second timescale parameter obtained by comparison of our AR3 model with the composite spectrum is $\tau_m = 80$ years. This value hints at a reference to MAC waves, where MAC stand for "magnetic" (i.e. Lorentz), "Archimedes" (i.e. buoyant), and "Coriolis" forces. In 1993 Braginsky theoretically predicted the possibility of MAC waves in Earth's outer core due to the interplay between these three forces in the momentum-balance equation for fluid parcels in Earth's outer [Braginsky, 1993]. [13] MAC waves are commonly expected to operate on timescales between 60 and 80 years in Earth's outer [Buffett, 2014], which act as an approximate bound for our estimated $\tau_m = 80$ years. Our new model suggests that MAC waves are partially responsible for the fluctuations of the

---

[12] Of course, because thermal conductivity values are not well constrained for Earth's outer core, a variety of estimates for σ and hence η are possible and will change the timescale we expect Ohmic diffusion to occur on. In addition, the length scale L used is subjective; L could be the outer core radius, the total core radius, the total core diameter, or even the outer core circumference at the core-mantle boundary. What really matters is that we have constrained a timescale for Ohmic diffusion τ_d that lies within a small order-of-magnitude range and is roughly reflected by the first transition frequency in the composite spectrum.

[13] MAC waves are similar to Rossby waves, which occur in Earth's atmosphere as a result of the interplay between Coriolis and inertial forces in the momentum balance equation for fluid parcels in Earth's atmosphere.

axial dipole moment away from its equilibrium behavior.

Torsional Oscillations in Earth's Outer Core

The third timescale parameter describing fast fluctuations of the axial dipole moment away from its steady state is $\tau_s = 1.6$ years. Subdecadal variations in the geomagnetic field are often called geomagnetic jerks, and are associated with changes in the length of day [Holme and de Viron, 2005] and with torsional oscillations in Earth's outer core [Cox et al., 2016], [Mound and Buffett, 2003], [Buffett et al., 2009]. To understand torsional oscillations, we must first understand how there might be cylindrical regimes of fluid motion in Earth's outer core.

As we have found immensely useful in our modeling approach, the spherical harmonic with the strongest contribution and the most temporal variability in the total geomagnetic field is the dipole. The 11° tilt between the dipole axis and Earth's rotation axis averages out to 0° over time so we can approximate the geomagnetic field as an axial dipole field, which could be reproduced by a hypothetical ring current sitting at Earth's center. The latter suggests that the dominant axial dipole field reflects a ring or cylindrical current structure in the outer core. Ring-like outer-core currents also make sense because the Earth's rotation influences the fluid motion. We thus expect cylindrical fluid formations that are coaxial with Earth's axis of rotation. Figure 2.17 shows three, discrete coaxial cylinders of fluid but the actual outer core should consist of a continuous distribution of coaxial cylinders.

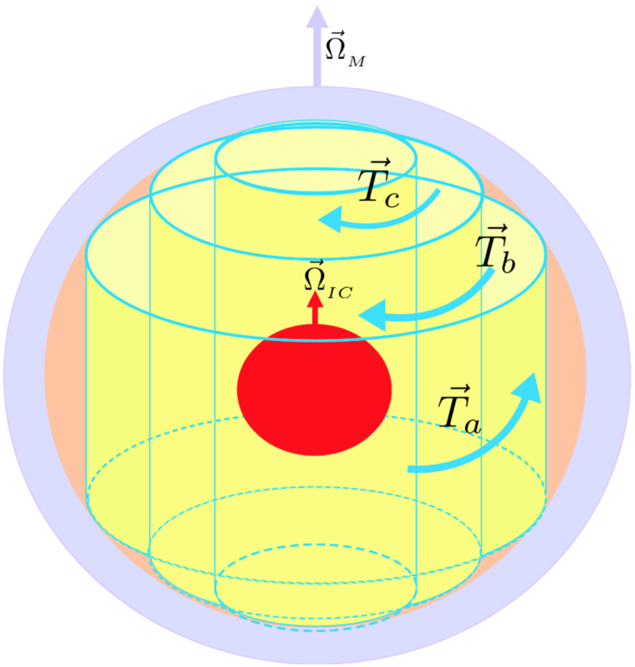

$$\vec{T}_a + \vec{T}_b + \vec{T}_c = \vec{0}$$

Figure 2.17: Illustrated are three, discrete coaxial fluid cylinders of flow in the outer core. The inner core is in red, the mantle is in violet, and the outer core is everything in between (yellow to show cylindrical flow and brown to show general outer core). $\vec{T}$ is the Lorentz torque on one cylinder - the net Lorentz torque across all three cylinders must be $\vec{0}$ to satisfy the Taylor constraint.

It turns out that if the Earth's outer core *does* exhibit such cylindrical flow, the geomagnetic field in the outer core must be structured so that the net Lorentz torque integrated across all of the coaxial cylinders must be zero at all times. This is called the Taylor constraint [Dumberry, 2008]. Since both the field structure and the outer core flow vary with time, the Lorentz torque on each, individual cylinder varies with time. If the angular velocity of one fluid cylinder changes even a little bit, the Lorentz torque on that cylinder will change. In order to maintain the Taylor constraint, all of the other cylinders must adjust their angular velocity as quickly as possible. And then because the fluid motion has changed, the field produced is different so its structure and resulting Lorentz torque acting on coaxial cylinders in the outer core must be different. The latter forces fluid cylinders to adjust their flow again to maintain the Taylor constraint.

The coaxial fluid cylinders thus oscillate back and forth with respect to each other as they respond to continuous changes in the geomagnetic field and outer-core fluid motions. These oscillations are called torsional oscillations. Gillet et al. (2010) showed that surface measurements of the geomagnetic field could be inverted for core flow models and that the latter showed torsional oscillations operating in Earth's outer core [Gillet et al., 2010]. On the other hand, numerical geodynamo simulations that are considered to be "Earthlike" cannot timestep rapidly enough to produce torsional oscillations, so it remains ambiguous whether torsional oscillations are really occurring in Earth's outer core.

Because torsional oscillations are related to the angular velocity of the fluid in Earth's outer core, which is related to the gravitationally-coupled angular velocity of Earth's mantle and inner core via the core-mantle boundary and the inner-core boundary respectively, several studies have related torsional oscillations to changes in the length of day [Holme and de Viron, 2005]. The latter was shown to operate on a 6-year timescale, which does not quite match our $\tau_s = 1.6$ years. However, τ_s was obtained by inspection of the composite spectrum and as is evident from Figure 2.16, our visual estimate for $f_{4,6}$ could be off due to a variety of reasons (smoothing in the inversion procedures used to build CALK10k.2, HFM.OL1.A1 and GUFM1 causes their spectra to drop rapidly, or possibly we need a higher-order model that reaches f^{-8} behavior and skips f^{-6} behavior entirely).

Our new model tentatively suggests that fluctuations of the axial dipole moment away from its equilibrium behavior are partially due to torsional oscillations in Earth's outer core, if they exist.

The Rate of Energy Re-stabilization in the Dipole Field

The last parameter obtained for our new model is the diffusion coefficient, $D_{eq} = 80.6\ \frac{10^{44} A^2 m^4}{Myr}$. Below we give two equations that describe the diffusion coefficient. We used Equation 2.102 to estimate D_{eq} from the composite spectrum. Equation 2.103 was obtained by solving for the diffusion coefficient as a function of each AR model variance in Table 2.3. The equivalence is exact for the AR1 case. Since τ_m and τ_s are so small relative to τ_l, the influence of the former two quantities on the predicted variance is relatively negligible in the AR2 and AR3 cases and thus we have an approximate equivalence that produces Equation 2.103.

$$D_{eq} = \frac{S_{\varphi'}(0)}{2\tau_l^2} \tag{2.102}$$

$$D_{eq} = \frac{\sigma_{\varphi'}^2}{\tau_l} \tag{2.103}$$

Equation 2.103 looks like a rate of some kind. If we consider the scenario in Figure 2.18 where the axial dipole moment fluctuates away (blue box) from equilibrium (orange line) and then drifts back (pink box), we can label the time taken for the axial dipole moment to return to equilibrium as τ_l and label the deviation away from equilibrium as the standard deviation predicted by our AR models, $\sigma_{\varphi'}$. At first glance, it seems like the ratio between the standard deviation and the drift timescale tells us a rate at which the axial dipole moment returns to steady state.

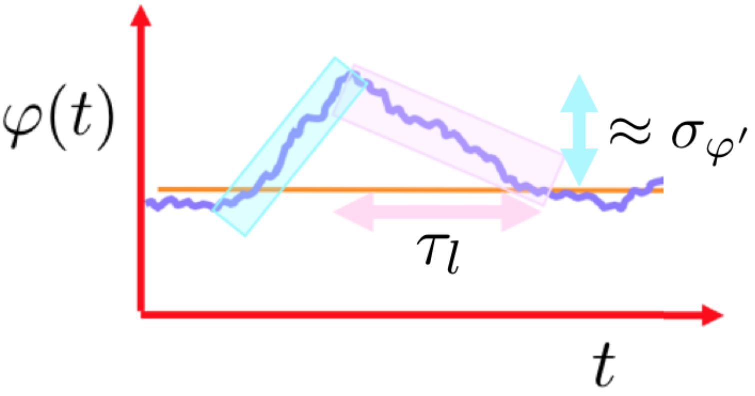

Figure 2.18: τ_l is the timescale taken by the axial dipole moment to return to its equilibrium behavior after it has been perturbed away and the model standard deviation $\sigma_{\varphi'}$ can be taken as the approximate deviation of the axial dipole moment from equilibrium each time it is perturbed away.

Recall that the energy in a magnetic field is always proportional to the squared field strength [Griffiths, 2017], so the energy contained within the axial dipole field will be proportional to the axial dipole moment squared. Consequently, the energy carried within variations of the axial dipole field away from its equilibrium state should be proportional to the variance of the axial dipole moment, $\sigma^2_{\varphi'}$. We hence propose that Equation 2.103 tells us the rate at which the energy in the axial dipole field is depleted by Ohmic diffusion operating on timescale τ_l.

This starts to paint a clearer picture of what may be going on in Earth's outer core. MAC waves and torsional oscillations pump the axial dipole field with magnetic energy on decadal and subdecadal timescales, which makes the axial dipole field less energetically stable. Meanwhile, Ohmic diffusion occurs on ten-thousand year timescales, lowering the axial dipole field back to a stable energy state at a rate near $D_{eq} = 80.6\ \frac{10^{44} A^2 m^4}{Myr}$.

2.5.2 Comparing the Nonlinear Langevin and Linear Autoregressive Models

Understanding the variance of the axial dipole moment gives us insight into the energy states of the dipole field and thus can help us understand how energy moves throughout the geodynamo. Figure 2.12 shows that simulations of the Langevin models consistently have a higher variance than simulations of the autoregressive models. There are several reasons for this. First of all, simulations of the Langevin model for each correlation of $\Gamma(t)$ are generated by drawing a value for the drift $v(\varphi)$ and for the diffusion coefficient $D(\varphi)$ from the curves in Figure 1.10, at each timestep. Figure 1.10 shows that $v(\varphi)$ and $D(\varphi)$ are nonlinear functions of axial dipole moment, $\varphi(t)$, and thus also nonlinearly depend on time. The drift and diffusion thus inherently have a variance of their own, before even playing a role in the Langevin equation. Meanwhile, in the AR models $D(\varphi)$ is assumed to be constant so it has 0 variance and $v(\varphi)$ is linearly dependent on $\varphi(t)$, which implies that the variance of the drift is just the variance of the axial dipole moment. Ultimately, realizations of the Langevin models will always have higher variance than realizations of the autoregressive models as a direct consequence of the assumptions used to recast the Langevin equation as an autoregressive equation.

Since the model variance is technically derived to match the autoregressive representation it should match the variance of our AR model simulations. In the AR1 case, both Euler's method and Tustin's method yield simulations with variances that are lower than the model variance. In the AR2 and AR3 cases, the model variance sits above the variance produced by Euler's method and below the variance produced by Tustin's method. However, the differences between all three variance values are much less than their magnitudes and thus we conclude that the simplified Langevin model and its simulations both have statistically similar variance values.

Second of all, because $v(\varphi)$ and $D(\varphi)$ are drawn from Figure 1.10, which displays axial dipole moment values that range from negative to positive, at each timestep, the code built to discretize the Langevin models for $\varphi(t)$ can simulate reversals whereas the code that discretizes the autoregressive models for $\varphi'(t)$ describes the variations of the moment about a stable polarity state and thus do not simulate reversals. Each time we simulated a discrete process for the Langevin model, we took the absolute value of the realization before computing its variance and producing its frequency spectrum [14]. Doing so treats the dipole low associated with a reversal as normal secular variation, rather than a separate behavior that must be extracted out, and taking the absolute value of a Langevin model simulation effectively turns the reversal into an excursion, as illustrated in Figure 2.19. Hence an added amount of variance arises from the excursional dips that remain after taking the absolute value of a simulation for the Langevin model while corresponding autoregressive simulations totally lack excursional dips and thus have lower overall variance.

---

[14]- only after this did we compute the average variance and average spectrum across all realizations of the discrete process

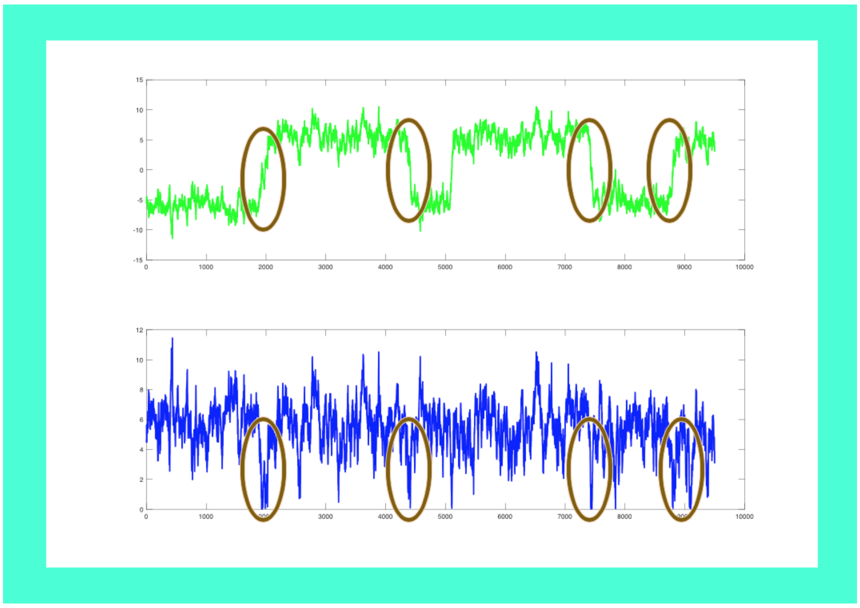

Figure 2.19: The top panel shows a simulation of the Langevin model with uncorrelated $\Gamma(t)$. The reversals are circled. The bottom panel shows the absolute value of the simulation, in which the reversal events have all been replaced with excursions that are circled.

Figures 2.13 through 2.15 show that the Langevin model predicts the lowest-frequency jump that we see in the geomagnetic composite spectrum. For the geomagnetic field, this jump is expected to reflect changes in reversal rate. Since simulations of the Langevin model exhibit reversals and simulations of the autoregressive models don't, it makes sense that the former have the jump and the latter do not. Our Langevin models do not explicitly predict reversals other than by the nonlinear odd and even curves for drift and diffusion coefficient in Figure 1.10.

Fortunately, the Poisson reversal model of Constable et al. (1998) is specifically built to simulate reversals. It may prove useful to modify their Poisson reversal model so that the average reversal rate λ and the average reversal duration δ both vary with time. The new Poisson model spectrum will be a time-varying spectrum, often referred to as a Wigner spectrum, that replaces

Equation 1.44 and has the form

$$S(f) = \frac{4\lambda(t)e^{-\lambda(t)\delta(t)}}{\lambda^2(t) + 4\pi^2 f^2}\left(1 - e^{-\lambda(t)\delta(t)}\left(\cos(2\pi f\delta(t)) + \frac{\lambda(t)\sin(2\pi f\delta(t))}{2\pi f}\right)\right). \tag{2.104}$$

This new spectral curve should help us investigate exactly how a time-varying $\lambda(t)$ impacts the spectrum of the axial dipole moment at lowest frequencies, and whether the lowest-frequency jump in the composite geomagnetic spectrum actually reflects changes in reversal rate.

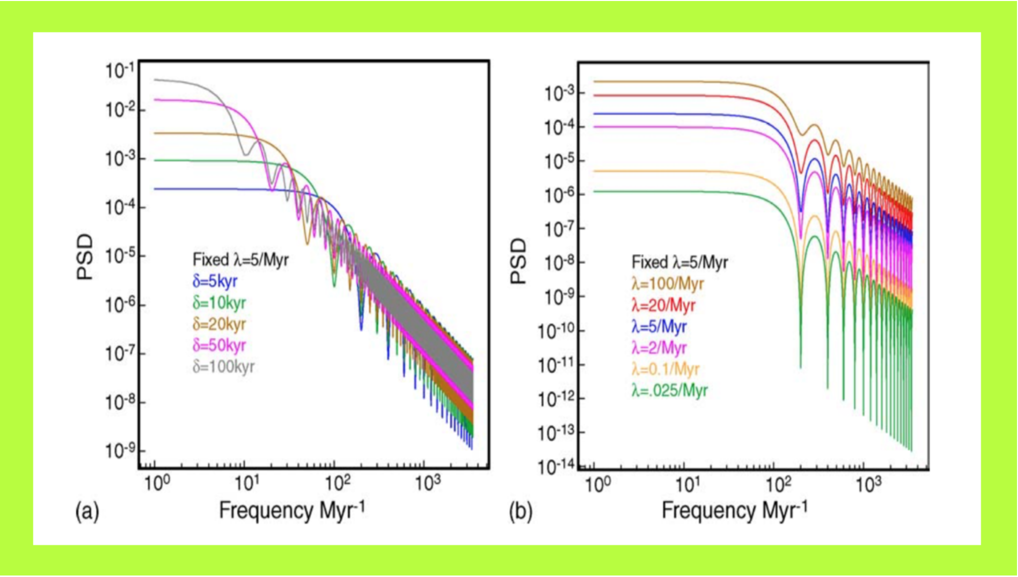

Figure 2.20: The effects of changing average reversal duration δ or average reversal rate λ on the Poisson model spectrum are plotted. [Constable and Johnson, 2005]

Constable and Johnson (2005) tested the effects of changing the average reversal rate λ and the average reversal duration δ in Equation 2.104, as shown in Figure 2.20. The authors also took the reversal records CK95 and CK95cc, treated each reversal as an axial dipole moment drop to 0, supposed that each reversal could be given a specific duration δ, and plotted the resulting empirical spectra against the Poisson model spectrum in Figure 2.21.

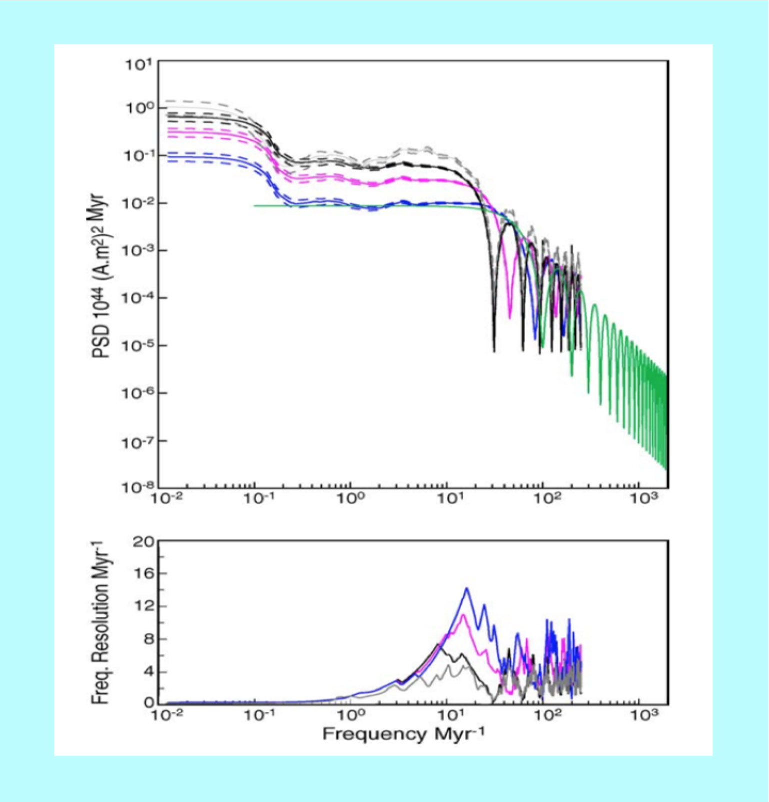

Figure 2.21: Blue, pink and black curves correspond to $\delta = 10, 20$ or 30 kyr respectively for CK95 while the grey curve is for CK95cc. CK95 spans 0-160 Ma while CK95cc spans 0 - 83 Ma with $\delta = 30$ kyr. The dashed lines provide one standard error estimates for the spectral curves. The green curve is the Poisson model spectrum with $\lambda\delta = 0.02$. The lower panel shows the frequency resolution corresponding to the spectral curves. [Constable and Johnson, 2005]

As we mentioned previously, the spectrum of the AR1 model is similar to Equation 2.104 and the only significant difference is the term in large parentheses. Meanwhile, we do not yet know the spectrum that pertains to the nonlinear Langevin model - we only computed the spectrum for the simplified (i.e. linear autoregressive) version because we do not have explicit forms for $v(\varphi(t))$ and

$D(\varphi(t))$. It is possible that the presence of time-varying $v(\varphi(t))$ and $D(\varphi(t))$ will modify the spectrum of the simplified Langevin model by introducing a multiplicative term just like the parentheses-enclosed term in Equation 2.104.

We anticipate this solely because the time-dependent drift and diffusion coefficient seem to be responsible for changes in reversal rate - if and only if the lowest-frequency jump in our Langevin simulations corresponds to the jump in the composite spectrum and the latter does, in fact, reflect changes in reversal rate - and the multiplicative factor in Equation 2.104 directly describes dipole reversals. In turn, the influence of the time-varying $v(\varphi(t))$ and $D(\varphi(t))$ on the autoregressive model spectrum might be inferred from the changes to parentheses-enclosed term in the Poisson model spectrum when $\lambda(t)$ and $\delta(t)$ are functions of time. This process potentially offers insight into the explicit forms of $v(\varphi(t))$ and $D(\varphi(t))$.

2.5.3 Comparing the Stochastic Models with the Composite Geomagnetic Spectrum

Figure 2.16 shows that our model does not perfectly match the composite geomagnetic spectrum. The f^{-2} regime looks like it is too steep and the f^{-4} and f^{-6} regimes looks like they are not steep enough. The latter might just be an issue with smoothing in the high-frequency data or inversion methods that were used to build CALS10k.2, HFM.OL1.A1 and GUFM1 that acts like a lowpass filter. Also, there is a large gap in the composite spectrum between CALS10k.2 and GUFM1 which leaves us to guess visually at whether the actual spectrum of the geomagnetic axial dipole moment should be more or less steep than what the adjacent segments suggest. To address the former issue, note that the cause for the shallowing in GGF100k is yet unclear and we do not know whether this is a distinct feature or if it indicates that the $s = -2$ spectral index is indeed too steep. We could bandpass filter GGF100k to keep only the domain where its spectrum shallows and investigate whether a pattern emerges.

2.6 Conclusions

In this study we developed an order-3 autoregressive model for the continuous variations in the axial dipole moment of the geomagnetic field with respect to time. The new model takes the form of a linear differential equation driven by Gaussian-distributed white noise. The model is characterized by a slow drift timescale τ_l by which the axial dipole moment returns to its equilibrium state after being pulled away. Such perturbations from equilibrium are characterized by shorter timescales τ_m and τ_s and a diffusion coefficient, D_{eq}, that dictates the relative influences between the fluctuations away from, and drift towards, equilibrium on axial dipole behavior.

The new AR3 model is expedient because it predicts a theoretical frequency spectrum with the same shape as a known, composite spectrum for the geomagnetic axial dipole moment. Values for $\{\tau_l, \tau_m, \tau_s, D_{eq}\}$ estimated by comparing our model spectrum with the composite spectrum suggest that MAC waves and torsional oscillations in Earth's outer core cause the axial dipole moment to fluctuate away from equilibrium while Ohmic diffusion drives the drift of the axial dipole moment toward equilibrium. D_{eq} may reflect a rate at which Ohmic diffusion re-stabilizes the axial dipole field on 10^4-year timescales while MAC waves and torsional oscillations pump the axial dipole field with energy and render it unstable on 10^0 to 10^1-year timescales.

Evidently, we can deduce possible physics of the geodynamo from such a stochastic model without needing to directly observe the Earth's outer core. Stochastic modeling of geomagnetic field variations thus presents a powerful tool to understanding the Earth's deep interior.

Table 2.3: $\{\gamma_s, \gamma_1, \gamma_2\}$ are in Equation 2.42.

AR Order	Spectrum, $S(f)$	Variance, $\sigma^2_{\varphi'}$	Autocovariance, $R_{\varphi'}(\tau)$
1	$\frac{2D_{eq}}{4\pi^2 f^2+\frac{1}{\tau_l^2}}$	$D_{eq}\tau_l$	$D_{eq}\tau_l e^{\frac{-\tau}{\tau_l}}$
2	$\frac{2D_{eq}\tau_m^{-2}}{(4\pi^2 f^2+\frac{1}{\tau_l^2})(4\pi^2 f^2+\frac{1}{\tau_m^2})}$	$\frac{D_{eq}\tau_l^2}{\tau_l+\tau_m}$	$\frac{-D_{eq}\tau_l^3}{\tau_m^2-\tau_l^2}e^{-\frac{\tau}{\tau_l}} + \frac{D_{eq}\tau_m\tau_l^2}{\tau_m^2-\tau_l^2}e^{-\frac{\tau}{\tau_m}}$
3	$\frac{2D_{eq}\tau_m^{-2}\tau_s^{-2}}{((4\pi^2 f^2+\frac{1}{\tau_l^2})(4\pi^2 f^2+\frac{1}{\tau_m^2})(4\pi^2 f^2+\frac{1}{\tau_s^2})}$	$\frac{D_{eq}}{\tau_m^2\tau_s^2}\left(\gamma_s\tau_l + \gamma_1\tau_m + \gamma_2\tau_s\right)$	

Table 2.4: Our simulated, discrete processes.

1	Random $\Gamma(t)$, Langevin		Euler-discretized AR1 $\varphi'(t)$	Tustin-discretized AR1 $\varphi'(t)$
2	Euler-discretized AR1 $\Gamma(t)$, Langevin	Tustin-discretized AR1 $\Gamma(t)$, Langevin	Euler-discretized AR2 $\varphi'(t)$	Tustin-discretized AR2 $\varphi'(t)$
3	Euler-discretized AR2 $\Gamma(t)$, Langevin	Tustin-discretized AR2 $\Gamma(t)$, Langevin	Euler-discretized AR3 $\varphi'(t)$	Tustin-discretized AR3 $\varphi'(t)$

Appendix A

Developing a Differential Equation for the Autocovariance of a Process

We first show how to derive a differential equation for the autocovariance of a process that is described by a continuous, autoregressive equation. The order of the equation does not matter - the result is essentially the same. Suppose that a process, $y(t)$, is described by the stochastic differential equation

$$a\frac{d^2y}{dt^2} + b\frac{dy}{dt} + cy(t) = \zeta(t) \tag{A.1}$$

where $\zeta(t)$ is Gaussian-distributed white noise. We use $\zeta(t)$ to indicate Gaussian-distributed random noise throughout this study. We multiply both sides by $y(t+\tau)$, and then take the expectation value. Distributing the expectation value throughout yields

$$< a\frac{d^2y}{dt^2}y(t+\tau) > + < b\frac{dy}{dt}y(t+\tau) > + < cy(t)y(t+\tau) > \quad = \quad < \zeta(t)y(t+\tau) > \tag{A.2}$$

where the last term is 0 because $\zeta(t)$ is a white noise process so it is totally uncorrelated and thus on average the rightmost product will turn to 0. We address each of the three terms on the left side individually. The first term can be simplified as

$$< a\frac{d^2y}{dt^2}y(t+\tau) > \quad = \quad < a\frac{d^2y}{dt^2}y(t) > \tag{A.3}$$

because we assume that the stochastic process is infinite and stationary, so the expectation value should not change after *any* lag time τ. Then we notice that $\frac{d^2y}{dt^2}$ and $\frac{d^2y}{d\tau^2}$ because τ is just a time increment of shift, and thus a small change in it is equivalent to a small change in time. So we have

$$< a\frac{d^2y}{dt^2}y(t+\tau) > \quad = \quad < a\frac{d^2y}{d\tau^2}y(t) > \tag{A.4}$$

$$= \quad < a\frac{d}{d\tau}\Big(\frac{dy}{d\tau}y(t)\Big) > \tag{A.5}$$

$$= \quad < a\frac{d}{d\tau}\Big(\frac{d}{d\tau}y(t+\tau)y(t)\Big) > \tag{A.6}$$

$$= \; < a\frac{d^2}{d\tau^2}\Big(y(t+\tau)y(t)\Big) > \tag{A.7}$$

$$= \; a\frac{d^2}{d\tau^2}\Big(< y(t+\tau)y(t) > \Big) \tag{A.8}$$

$$\Longrightarrow < a\frac{d^2y}{dt^2}y(t+\tau) > \; = \; a\frac{d^2(R_y(\tau))}{d\tau^2} \tag{A.9}$$

is the first term. Similarly,

$$< b\frac{dy}{dt}y(t+\tau) > \tag{A.10}$$

$$= \; < b\frac{dy}{dt}y(t) > \; = \; < b\frac{dy}{d\tau}y(t) > \tag{A.11}$$

$$= \; b\frac{d}{d\tau}\Big(< y(t+\tau)y(t) > \Big) \tag{A.12}$$

$$\Longrightarrow < b\frac{dy}{dt}y(t+\tau) > \; = \; b\frac{d(R_y(\tau))}{d\tau} \tag{A.13}$$

and

$$< cy(t)y(t+\tau) > \; = \; cR_y(\tau). \tag{A.14}$$

The original stochastic differential equation becomes

$$a\frac{d^2R_y}{d\tau^2} + b\frac{dR_y}{d\tau} + cR_y(\tau) = 0. \tag{A.15}$$

Appendix B

Why $\zeta(t)$ Has Variance 2

The Fourier transform of $R_{\varphi'}(\tau)$ for the AR1 model is

$$\mathscr{F}\Big(R_{\varphi'}(\tau)\Big) = \int_{-\infty}^{\infty} Deq.\tau_l e^{\frac{-\tau}{\tau_l}} e^{-2\pi i f \tau} d\tau \tag{B.1}$$

$$= (Deq.\tau_l)\Big(\frac{2\frac{1}{\tau_l}}{4\pi^2 f^2 + \frac{1}{\tau_l^2}}\Big) \tag{B.2}$$

$$= \frac{2Deq.}{4\pi^2 f^2 + \frac{1}{\tau_l^2}}. \tag{B.3}$$

Equation B.2 reveals that the Fourier transform of double-sided exponential decay function automatically has a 2 in its numerator. The same applies to the AR2 and AR3 models, where $R_{\varphi'}(\tau)$ contains multiple double-sided exponential functions and thus a factor of 2 emerges when we compute the model spectrum according to Equation2.8.

This is why we mandate that the white noise process, $\zeta(t)$, must have a variance of 2. From the AR1 example it is clear that inserting $|\tilde{\zeta}(f)|^2 = 2$ into Equation 2.9 produces Equation B.3. In fact for any model order, $|\tilde{\zeta}(f)|^2 = 2$ ensures that we obtain matching model spectra according to *both* Equation 2.8 and Equation 2.7.

Appendix C

Tustin's Method

Tustin's method is used to design a digital filter that yields a discrete sequence whose frequency distribution matches that of a continuous process. The first step to designing a digital filter is to recall the Laplace transform. That is,

$$\tilde{y}(s) \equiv \mathscr{L}\Big(y(t)\Big) \equiv \int_{-\infty}^{\infty} y(t)e^{-st}dt, \tag{C.1}$$

in which s is complex. If and only if $s = 2\pi if$, this integral turns into the (continuous-time) Fourier transform. The Fourier transform is just the Laplace transform evaluated on the imaginary axis of the complex s plane. When $s = 2\pi if$ and f are real-valued, changing f equates to picking points along the imaginary axis. While the Fourier transform exhibits the behavior of our system in a one-dimensional "real frequency" domain, the Laplace transform shows us the behavior of our system in a two-dimensional "complex frequency" domain. The difference can be visualized as shown in Figure C.1.

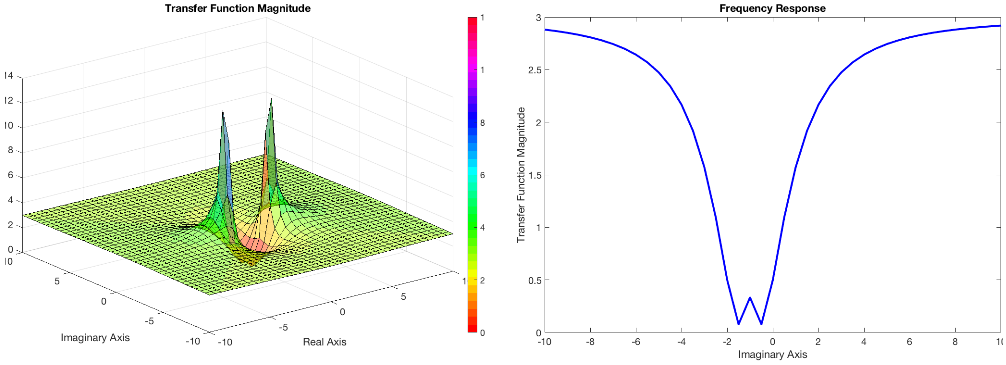

Figure C.1: On the left is a plot of the magnitude of the transfer function $\tilde{g}(s) \equiv \frac{3s^2+6is-2}{-is^2+2s+4i}$ atop the complex s plane. The two poles and two zeros are visibly at $i+\sqrt{3}$, $i-\sqrt{3}$, $\frac{-i}{3}(\sqrt{3}+3)$, and $\frac{i}{3}(\sqrt{3}-3)$, respectively. On the right is the magnitude of the transfer function exactly at the imaginary axis; this is the ratio between the real frequency distributions of the output and the input for the differential system described by $\tilde{g}(s)$.

We must also derive a discrete analog to the Laplace transform. Suppose we sample from the continuous process $y(t)$ at the regular time interval Δt. As illustrated in Figure C.2, our sequence of samples is

$$y_n = \sum_{n=0}^{\infty} \delta(t - n\Delta t) y(t); \tag{C.2}$$

we are assuming that the sequence is infinite because the continuous process is infinite. Then, taking the Laplace transform of the sequence yields

$$\mathscr{L}\Big(y_n\Big) \tag{C.3}$$

$$= \int_{-\infty}^{\infty} e^{-st} \sum_{n=0}^{\infty} \delta(t - n\Delta t) y(t) dt \tag{C.4}$$

$$= \sum_{n=0}^{\infty} \int_{-\infty}^{\infty} e^{-st} \delta(t - n\Delta t) y(t) dt \tag{C.5}$$

$$= \sum_{n=0}^{\infty} e^{-sn\Delta t} y(n\Delta t). \tag{C.6}$$

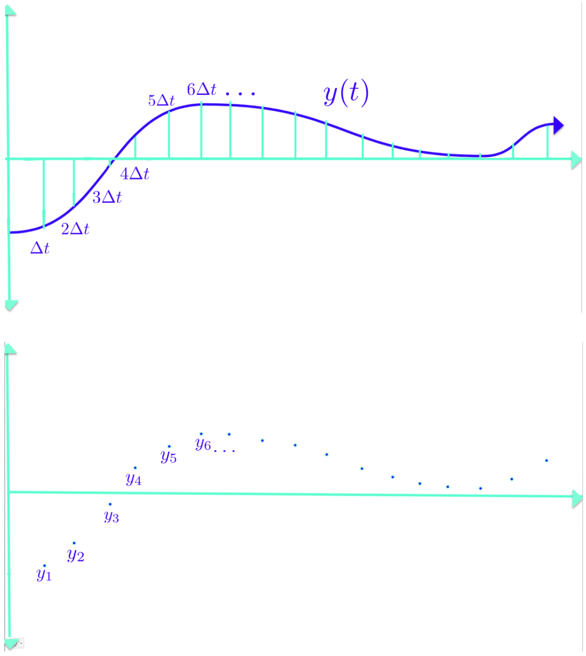

Figure C.2: Sampling a continuous process. The smaller the value of Δt, the better the sequence y_n will resemble the original process $y(t)$.

Notice how $y(n\Delta t) = y_n$ from Figure C.2. If we simplify our sum by letting

$$z \equiv e^{s\Delta t}, \quad \text{then} \tag{C.7}$$

$$\Longrightarrow \; \tilde{y}(z) \equiv \sum_{n=0}^{\infty} z^{-n} y_n, \tag{C.8}$$

is formally called the “z-transform”, in which z is complex. If and only if $z = e^{2\pi i f \Delta t}$, this sum turns into the discrete Fourier transform of an infinite sequence.

So the discrete Fourier transform is just the z-transform evaluated on the unit circle in the complex z plane. This can be visualized as shown in the diagram. While the Laplace transform describes the complex frequency distribution of a continuous signal, the z-transform describes the complex frequency distribution of a discrete process - in our case a recursive digital filter.

We look at things in the complex frequency domain because it provides general theory for recursive digital filters that mimic complex-coefficient differential equations; we return to real coefficients and frequencies at the very end. First, we take the Laplace transform of the entire autoregressive equation. For example, if we have a second-order stochastic differential equation,

$$a\frac{d^y}{dt^2} + b\frac{dy}{dt} + cy(t) = \zeta(t) \tag{C.9}$$

$$\implies \mathscr{L}\Big(a\frac{d^y}{dt^2} + b\frac{dy}{dt} + cy(t) = \zeta(t)\Big) \tag{C.10}$$

$$\implies a\Big(s^2\tilde{y}(s) - sy(0) - \frac{dy}{dt}\Big|_{t=0}\Big) + b\Big(s\tilde{y}(s) - y(0)\Big) + c\tilde{y}(s) = \tilde{\zeta}(s). \tag{C.11}$$

Next we assume that all of the initial conditions are zero and then solve for the ratio between the output and the input. So $y(0) = 0$ and $\frac{dy}{dt}\Big|_{t=0} = 0$ and

$$(as^2 + bs + c)\tilde{y}(s) = \tilde{\zeta}(s) \tag{C.12}$$

$$\Longrightarrow \frac{\tilde{y}(s)}{\tilde{\zeta}(s)} \equiv \tilde{g}(s) = \frac{1}{as^2 + bs + c}. \tag{C.13}$$

This ratio is called the transfer function. Notice that the bottom is a polynomial, indicating that there are "poles", s_i, in the complex plane where the transfer function blows up because the s_i are the roots of the polynomial. The reason we look at this ratio rather than just $\tilde{y}(s)$ is because both $y(t)$ and $\zeta(t)$ are continuous processes we want to discretize, so it is efficient to analyze both as a ratio in one, clean sweep.

Meanwhile, a recursive digital filter has the standard form

$$\sum_{k=0}^{K-1} \alpha_k y_{n-k} = \sum_{l=0}^{L-1} \beta_l \zeta_{n-l} \tag{C.14}$$

when $\{\zeta_t\}$ is the input sequence and $\{y_t\}$ is the output sequence. We assume that the input is white noise and want to find the $\{\alpha_k, \beta_l\}$ that make the complex frequency distribution of this filter process have the same poles, s_i, as that of our continuous process. So taking the z-transform and isolating the ratio between the output and input yields

$$\frac{\tilde{y}(z)}{\tilde{\zeta}(z)} \equiv \tilde{g}(z) = \frac{\sum_{l=0}^{L-1} \beta_l z^{-l}}{\sum_{k=0}^{K-1} \alpha_k z^{-k}} \tag{C.15}$$

as the transfer function of a digital filter. Now recall from Equation C.7 that

$$z = e^{s\Delta t}. \tag{C.16}$$

We can rewrite this as

$$z = \frac{e^{\frac{s\Delta t}{2}}}{e^{-\frac{s\Delta t}{2}}} \tag{C.17}$$

$$\approx \frac{1 + \frac{s\Delta t}{2} + \dots}{1 - \frac{s\Delta t}{2} + \dots} \tag{C.18}$$

$$\implies s = \left(\frac{2}{\Delta t}\right)\left(\frac{z-1}{z+1}\right) \tag{C.19}$$

where the expansion

$$e^x = \sum_{n=0}^{\infty} \frac{x^n}{n!} \tag{C.20}$$

is used. Equation C.19 is called the "bilinear transformation" and approximates the exact exponential transformation from s to z domain. We substitute equation C.19 into equation C.13 and algebraically simplify the result into a large fraction whose numerator and denominator are each polynomials of z. Comparing the coefficients of these polynomials with equation C.15, we obtain $\{\alpha_k, \beta_l\}$ and thus our digital filter as presented in Equation C.14.

Appendix D

Loss of Resolution In Spectral Estimates

When we want to model a physical quantity statistically, we usually treat the quantity represented in our model as a random variable with a mean and variance. This was the approach of CP88 [Constable and Parker, 1988] used to model various Gauss coefficients and describes our models of the axial dipole moment, which produce a theoretical variance for $\varphi'(t)$ and assume that it has mean 0. [1]

Suppose now that $S(f)$ is the true frequency spectrum of the continuously time-varying axial dipole moment of the geomagnetic field. Given a time series that samples the continuous process at N points, formalisms have been developed to compute a spectral estimate, $\hat{S}(f)$, which is a random variable that has a mean and standard deviation along a continuous range of frequencies.

So $\hat{S}(f)$ is the curve we compute using a time series that samples the continuous process in an effort to elucidate the shape of the true spectrum, $S(f)$.

---

[1] We do not discuss the theoretical probability function for $\varphi(t)$ predicted by the Langevin and AR models; for a discussion, see [Buffett et al., 2013].

There are two things that are difficult about producing a spectral estimate.

First, if we compute a direct spectral estimate using the formula

$$\hat{S}(f) = \frac{1}{N} \left| \sum_{n=0}^{N-1} y_n e^{-2\pi i n f} \right|^2 \tag{D.1}$$

then the standard deviation of $\hat{S}(f)$ is equal to its value at each frequency. When the standard deviation of our estimate is as big as the estimate itself, we know that our estimation procedure is not great.

Second, the expectation value of $\hat{S}(f)$ obtained via Equation D.1 is likely distorted from $S(f)$. A bit of algebra shows that the expectation value is

$$< \hat{S}(f) >= \int_{-\frac{1}{2}}^{\frac{1}{2}} S(f') F_N(f' - f) df' \tag{D.2}$$

where

$$F_N(f' - f) = \frac{1}{N} \frac{\sin^2(\pi N f)}{\sin^2(\pi f)} \tag{D.3}$$

is called the Fejer kernel. So the direct spectral estimate obtained from Equation D.1 is produced by convolving the true spectrum of the continuous process with the Fejer kernel.

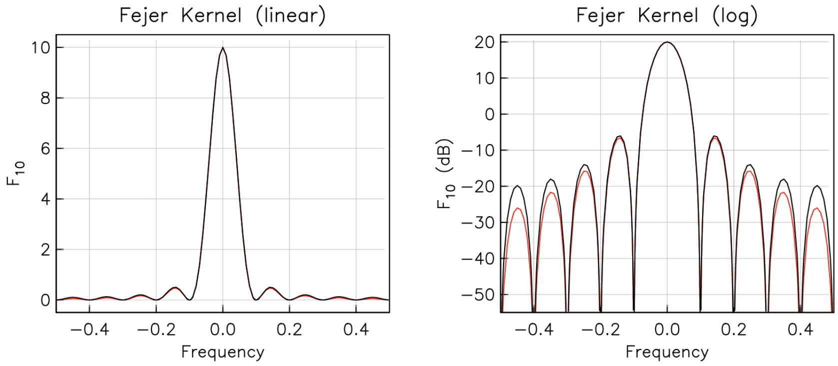

Figure D.1: Fejer kernel for N = 10 in a linear and log scale. The red curves are a sinc-squared approximation to the Fejer kernel. [Agnew et al., 2018]

The Fejer kernel is shown in Figure D.1 and has a significant amplitude away from its central peak. Notice that as $N \to \infty$, the Fejer kernel becomes a Dirac delta function and we ideally get $S(f) = \hat{S}(f)$. The Dirac delta function perfectly samples the true spectrum at every frequency with no interfering influence from the values of the spectrum at other frequencies. [2] Meanwhile, the large sidelobes of the Fejer kernel cause each spectrum value estimated at each frequency to be influenced by the values of the spectrum at adjacent frequencies and this effect is called spectral leakage.

Spectral leakage is a large problem when $S(f)$ has a large dynamic range. Since we cannot see $S(f)$ and only obtain $\hat{S}(f)$, we do not know precisely how much leakage occurred or where, during the estimation procedure.

We can solve the first issue by adopting some sort of averaging method. If we split the original time series into K segments and assume that the series is stationary and ergodic, then each segment gives us an independent time series for the axial dipole moment and we can compute K, independent direct spectral estimates (DSE) using Equation D.1 and finally average the K estimates

---

[2] So the value of $\hat{S}(f_0)$ only depends on the value of $S(f_0)$, and not on any other $S(f_i) \mid i \neq 0$.

together. The final, mean DSE has a variance that is $\frac{1}{K}$ times the variance of each DSE in the average. We have effectively lowered the variance of our estimate by a factor of K.

We can solve the second issue by considering Equation D.1 a little differently. Suppose that we multiply the time series by a sequence of weights, $\{w_n\}$, and recompute the weighted spectral estimate as

$$\hat{S}(f) = \frac{1}{N}\left|\sum_{n=0}^{N-1} w_n y_n e^{-2\pi i n f}\right|^2 \tag{D.4}$$

with expectation value

$$< \hat{S}(f) >= \int_{-\frac{1}{2}}^{\frac{1}{2}} S(f')\tilde{w}_k(f'-f)df' \tag{D.5}$$

where

$$\tilde{w}_k(f) = \frac{1}{N}\left|\tilde{w}(f)\right|^2 \tag{D.6}$$

is the squared Fourier transform of the wight sequence divided by its length. When $w_n = 1 \forall n \in [1, N]$, i.e. the weight sequence is a boxcar function whose squared Fourier transform over length is actually the Fejer kernel, we retrieve the formulas for the direct spectral estimate and its expectation value.

To ameliorate the spectral leakage caused by large sidelobes in the Fejer kernel, we design a sequence of weights $\{w_n\}$, called a taper, whose squared Fourier transform instead has small sidelobes relative to a prominent central lobe. To reduce the variance of our spectral estimate, it is sometimes useful to apply K different tapers to the entire time series rather than applying one taper to K individual segments of the time series. Furthermore, if we have K tapers that are mutually orthogonal, then each spectral estimate that results from the taper-and-transform procedure in Equation D.4 will be uncorrelated with the estimate produced using the next taper. This, in turn, reduces the variance of the final mean estimate as much as possible.

When we average K spectral estimates together, the mean curve is smoother and has lower frequency resolution than did each, independent estimate. Large and small values for K produce spectral estimates with less and more frequency resolution, respectively. So the averaging process lowers the variance of our final estimate, which is good, but also lowers the frequency resolution of our final estimate, which is unfortunate.

Often times tapers have broad central lobes and small sidelobes. The latter characteristic suppresses spectral leakage but the broad central lobe introduces a loss of frequency resolution. Like the tradeoff between variance and resolution that arises from averaging K spectral estimates together, a useful weight function introduces a tradeoff between spectral leakage and resolution.

The process of obtaining a spectral estimate with small variance and minimized spectral leakage is multifold: we multiply the time series - i.e. a realization of the axial dipole moment - by K orthogonal prolate tapers, compute K mutually-uncorrelated spectral estimates, and finally average all K spectral estimates together to form a mean estimate.

To generate empirical spectral estimates for realizations of the Langevin and AR processes, we used mutually-orthogonal prolate spheroidal tapers, shown by David Slepian in 1978 to have a Fourier transform that concentrates energy into the central lobe as much as possible [Slepian, 1978].

When computing empirical spectra for our order 3 model, we used a larger “time-bandwidth product”, p, than the one used for our lower-order cases. The time-bandwidth product p is a parameter that controls the width of the central lobe in each prolate taper. So the central lobe of all K prolate tapers got a little broader, lowering the frequency resolution of each spectral estimate produced per prolate taper.

The time-bandwidth product is also directly proportional to the number of tapers used. A higher value for p implies a higher value for K, lowering the frequency resolution in the mean spectral estimate produced for a single realization. Furthermore, the frequency resolution diminishes further when we average together 20 mean estimates pertaining to 20 realizations of a discrete process, and plot the final result in Figure 2.15.

When we generated DSE for the order-3 discrete processes, there was no discrepancy near $f_{0,2}$ but the DSE also flattened out before $f_{4,6}$ and failed to exhibit any f^{-6} behavior - a clear sign of spectral leakage. After prolate tapering, the spectral estimate continued to steepen at $f_{4,6}$ into f^{-6} behavior, but the discrepancy near $f_{0,2}$ appeared. We expect that in our aim to view the f^{-6} regime we lost spectral resolution, giving rise to the discrepancies between the empirical spectra and the composite curve near $f_{0,2}$ in Figure 2.15.

Appendix E

A Flowchart for our Code

In Figure E.1, "Equ. …" refers to stochastic differential equations that are labeled in the text.

A sequence of Γ_t values is produced, according to the linear AR equation for $\Gamma(t)$ that corresponds to each model order being considered, using either Euler or Tustin discretization. For each model order and for each discretization method, a value from the corresponding Γ_t sequence is fed into the nonlinear Langevin equation at each timestep. Values for the drift and diffusion coefficient are pulled from the curves in Figure 1.10 and also fed into the nonlinear Langevin equation at each timestep. The Euler-discretized nonlinear Langevin equation then generates a value for φ_t, at each timestep, according to the particular model order being considered (superscript) and discretization method used (subscript) - i.e. according to a particular discrete process from Table 2.3. Each discrete process in the row indicated by (a) in Figure E.1 is simulated 20 times. A prolate-tapered spectral estimate $\{S_f\}$ for every simulation of every discrete process is generated using the pmtm function in MATLAB and a half-bandwidth of 15, which yields the row marked by (b). The 20 spectral estimates produced for each realization of a discrete process are averaged to produce one, mean spectral estimate for that discrete process. The superscript indicates the AR order of $\Gamma(t)$ that was fed into the nonlinear Langevin equation. The subscript indicates which method was used to discretize the AR equation for $\Gamma(t)$.

Meanwhile, for each model order, the corresponding linear AR equation is discretized using either Euler or Tustin discretization. This generates a simulation for φ'_t pertaining to a particular discrete process from Table 2.3, depending on the model order and the discretization procedure used. Each discrete process in the row indicated by (c) in Figure E.1 is simulated 20 times. A prolate-tapered spectral estimate $\{S_f\}$ for every simulation of every discrete process is generated using the pmtm function in MATLAB and a half-bandwidth of 15, which yields the row marked by (d). The 20 spectral estimates produced for each realization of a discrete process are averaged to produce one, mean spectral estimate for that discrete process. The superscript indicates the AR order of $\varphi'(t)$. The subscript indicates the method used to discretize the AR equation for $\varphi'(t)$.

Prolate-tapered spectral estimates for discrete processes as well as the model spectrum pertaining to the order-1, 2, and 3 axial dipole are boxed in lilac, green and red, respectively. Mean spectral estimates are finally plotted against the corresponding AR model spectrum in Figures 2.13 through 2.15.

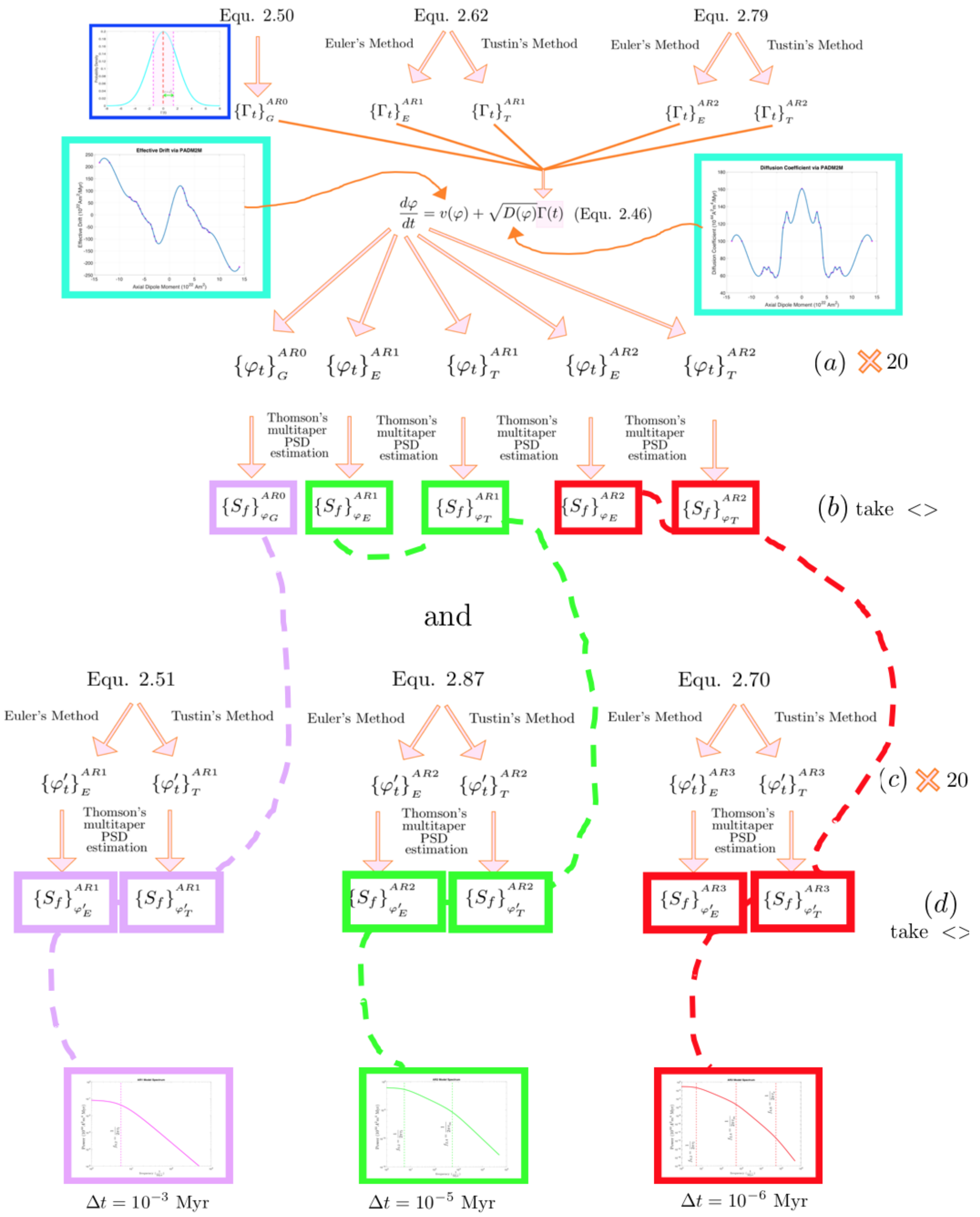

Figure E.1: A flowchart of the logic used to build our MATLAB code. The lilac, green, and red dashed lines link empirical spectra and the model spectrum pertaining to orders 1, 2, and 3, respectively. Spectra boxed in lilac, green, and red are superimposed to show our results for simulations of model orders 1, 2, and 3, respectively, in Section 2.4.

Bibliography

[Agnew et al., 2018] Agnew, D. C., Parker, R. L., and Constable, C. (2018). Geophysical data analysis: Fourier methods.

[Avery et al., 2017] Avery, M. S., Gee, J. S., and Constable, C. G. (2017). Asymmetry in growth and decay of the geomagnetic dipole revealed in seafloor magnetization. *Earth and Planetary Science Letters*, 467:79 – 88.

[Backus et al., 1996] Backus, G., Parker, R., and Constable, C. (1996). *Foundations of Geomagnetism*. Cambridge University Press.

[Bouligand et al., 2016] Bouligand, C., Gillet, N., Jault, D., Schaeffer, N., Fournier, A., and Aubert, J. (2016). Frequency spectrum of the geomagnetic field harmonic coefficients from dynamo simulations. *Geophysical Journal International*, 207:1142–1157.

[Braginsky, 1993] Braginsky, S. I. (1993). Mac-oscillations of the hidden ocean of the core. *Journal of Geomagnetism and Geoelectricity*, 45(11-12):1517–1538.

[Brockwell, 2001] Brockwell, P. (2001). Continuous-time arma processes. In *Stochastic Processes: Theory and Methods*, volume 19 of *Handbook of Statistics*, pages 249 – 276. Elsevier.

[Buffett, 2014] Buffett, B. (2014). Geomagnetic fluctuations reveal stable stratification at the top of the earth?s core. *Nature*, 507:484–487.

[Buffett and Matsui, 2015] Buffett, B. and Matsui, H. (2015). A power spectrum for the geomagnetic dipole moment. *Earth and Planetary Science Letters*, 411:20 – 26.

[Buffett and Puranam, 2017] Buffett, B. and Puranam, A. (2017). Constructing stochastic models for dipole fluctuations from paleomagnetic observations. *Physics of the Earth and Planetary Interiors*, 272:68 – 77.

[Buffett et al., 2014] Buffett, B. A., King, E. M., and Matsui, H. (2014). A physical interpretation of stochastic models for fluctuations in the earth's dipole field. *Geophysical Journal International*, 198:597–608.

[Buffett et al., 2009] Buffett, B. A., Mound, J., and Jackson, A. (2009). Inversion of torsional oscillations for the structure and dynamics of earth's core. *Geophysical Journal International*, 177:878–890.

[Buffett et al., 2013] Buffett, B. A., Ziegler, L., and Constable, C. G. (2013). A stochastic model for palaeomagnetic field variations. *Geophysical Journal International*, 195(1):86–97.

[Cande and Kent, 1995] Cande, S. C. and Kent, D. V. (1995). Revised calibration of the geomagnetic polarity timescale for the late cretaceous and cenozoic. *Journal of Geophysical Research: Solid Earth*, 100:6093–6095.

[Constable, 1990] Constable, C. (1990). A simple statistical model for geomagnetic reversals. *Journal of Geophysical Research: Solid Earth*, 95:4587 – 4596.

[Constable and Johnson, 2005] Constable, C. and Johnson, C. (2005). A paleomagnetic power spectrum. *Physics of the Earth and Planetary Interiors*, 153:61 – 73.

[Constable et al., 2016] Constable, C., Korte, M., and Panovska, S. (2016). Persistent high paleosecular variation activity in southern hemisphere for at least 10000 years. *Earth and Planetary Science Letters*, 453:78–86.

[Constable and Parker, 1988] Constable, C. and Parker, R. (1988). Statistics of geomagnetic secular variation for the past 5 My. *Journal of Geophysical Research: Solid Earth*, 93:11569–11581.

[Constable and Johnson, 1999] Constable, C. G. and Johnson, C. L. (1999). Anisotropic paleosecular variation models: implications for geomagnetic field observables. *Physics of the Earth and Planetary Interiors*, 115:35–51.

[Constable et al., 1998] Constable, C. G., Tauxe, L., and Parker, R. L. (1998). Analysis of 11 myr of geomagnetic intensity variation. *Journal of Geophysical Research*, 103:17,735 – 17,748.

[Constable et al., 1987] Constable, S. C., Parker, R. L., and Constable, C. G. (1987). Occam's inversion: A practical algorithm for generating smooth models from electromagnetic sounding data. *Geophysics*, 52:289–300.

[Cox et al., 2016] Cox, G., Livermore, P., and Mound, J. (2016). The observational signature of modelled torsional waves and comparison to geomagnetic jerks. *Physics of the Earth and Planetary Interiors*, 255:50 – 65.

[Davies and Constable, 2014] Davies, C. J. and Constable, C. G. (2014). Insights from geodynamo simulations into long-term geomagnetic field behavior. *Earth and Planetary Science Letters*, 404:238–249.

[Dumberry, 2008] Dumberry, M. (2008). Course 7 Taylor's constraint and torsional oscillations. In Cardin, P. and Cugliandolo, L., editors, *Dynamos*, volume 88 of *Les Houches*, pages 383 – 401. Elsevier.

[Finlay et al., 2016] Finlay, C. C., Olsen, N., Kotsiaros, S., Gillet, N., and Toffner-Clausen, L. (2016). Recent geomagnetic secular variation from swarm and ground observatories as estimated in the CHAOS-6 geomagnetic field model. *Earth, Planets and Space*, 68(1):112.

[Gillet et al., 2010] Gillet, N., Jault, D., Canet, E., and Fournier, A. (2010). Fast torsional waves and strong magnetic field within the earth?s core. *Nature*, 465:74–77.

[Glassmeier and Tsurutani, 2014] Glassmeier, K. and Tsurutani, B. T. (2014). Carl Friedrich Gauss, General Theory of Terrestrial Magnetism, a revised translation of the German text. *History of Geological and Space Sciences*, 5(1):11–62.

[Griffiths, 2017] Griffiths, D. J. (2017). *Introduction to Electrodynamics Fourth Edition*. Cambridge University Press.

[Gutenberg, 1951] Gutenberg, B., editor (1951). *Internal Constitution of the Earth*. Dover Publications, Inc.

[Hellio et al., 2014] Hellio, G., Gillet, N., Bouligand, C., and Jault, D. (2014). Stochastic modelling of regional archaeomagnetic series. *Geophysical Journal International*, 199:931–943.

[Holme and de Viron, 2005] Holme, R. and de Viron, O. (2005). Geomagnetic jerks and a high-resolution length-of-day profile for core studies. *Geophysical Journal International*, 160(2):435–439.

[Hulot et al., 2011] Hulot, G., Balogh, A., Christensen, U., Constable, C., Mandea, M., and Olsen, N. (2011). *Terrestrial Magnetism*. Springer Science+Business Media, LLC.

[Jackson and Finlay, 2015] Jackson, A. and Finlay, C. (2015). Chapter 5 volume 5 - Geomagnetic Secular Variation and Its Applications to the Core. In Schubert, G., editor, *Treatise on Geophysics (Second Edition)*, pages 137 – 184. Elsevier, Oxford, second edition.

[Jackson et al., 2000] Jackson, A., Jonkers, A. R. T., and Walker, M. R. (2000). Four centuries of geomagnetic secular variation from historical records. *Philosophical Transactions of the Royal Society A*, 358:957–990.

[Johnson and Constable, 1995] Johnson, C. L. and Constable, C. G. (1995). The time-averaged geomagnetic field as recorded by lava flows over the past 5 myr. *Geophysical Journal International*, 122:489–519.

[McFadden et al., 1988] McFadden, P. L., Merrill, R. T., and McElhinny, M. W. (1988). Dipole/quadrupole family modeling of paleosecular variation. *Journal of Geophysical Research: Solid Earth*, 93(B10):11583–11588.

[Moffatt, 1978] Moffatt, H. K. (1978). *Magnetic field generation in electrically conducting fluids.* Cambridge University Press.

[Mound and Buffett, 2003] Mound, J. E. and Buffett, B. A. (2003). Interannual oscillations in length of day: Implications for the structure of the mantle and core. *Journal of Geophysical Research: Solid Earth*, 108.

[O'Rourke et al., 2017] O'Rourke, J. G., Korenaga, J., and Stevenson, D. J. (2017). Thermal evolution of earth with magnesium precipitation in the core. *Earth and Planetary Science Letters*, 458:263 – 272.

[Panovska et al., 2018] Panovska, S., Constable, C. G., and Korte, M. (2018). Extending global continuous geomagnetic field reconstructions on timescales beyond human civilization. *Geochemistry, Geophysics, Geosystems.*

[Pozzo et al., 2012] Pozzo, M., Davies, C., Gubbins, D., and Alfè, D. (2012). Thermal and electrical conductivity of iron at earth's core conditions. *Nature*, 485:355–358.

[Quidelleur and Courtillot, 1996] Quidelleur, X. and Courtillot, V. (1996). On low-degree spherical harmonic models of paleosecular variation. *Physics of the Earth and Planetary Interiors*, 95:55–77.

[Shearer, 2009] Shearer, P. M. (2009). *Introducion to Seismology.* Cambridge University Press.

[Siefert and Peinke, 2004] Siefert, M. and Peinke, J. (2004). Reconstruction of the deterministic dynamics of stochastic systems. *International Journal of Bifurcation and Chaos*, 14:2005 – 2010.

[Slepian, 1978] Slepian, D. (1978). Prolate spheroidal wave functions, fourier analysis, and uncertainty — v: the discrete case. *The Bell System Technical Journal*, 57:1371 – 1430.

[Smith-Boughner et al., 2011] Smith-Boughner, L., Ziegler, L., and Constable, C. (2011). Changing spectrum of geomagnetic intensity variations in a fragmented 12my sediment record from the oligocene. *Physics of the Earth and Planetary Interiors*, 188(3):260 – 269. Proceedings of the 12th Symposium of SEDI.

[Tauxe, 2010] Tauxe, L. (2010). *Essentials of Paleomagnetism.* University of California Press.

[Tauxe and Kent, 2004] Tauxe, L. and Kent, D. V. (2004). A simplified statistical model for the geomagnetic field and the detection of shallow bias in paleomagnetic inclinations: Was the ancient magnetic field dipolar? *AGU Geophysical Monograph.*

[Wang et al., 2016] Wang, D., Sun, S., Chen, X., and Yu, Z. (2016). A 3d shape descriptor based on spherical harmonics through evolutionary optimization. *Neurocomputing*, 194:183 – 191.

[Ziegler et al., 2011] Ziegler, L. B., Constable, C. G., Johnson, C. L., and Tauxe, L. (2011). PADM2M: a penalized maximum likelihood model of the 0-2 Ma palaeomagnetic axial dipole moment. *Geophysical Journal International*, 184:1069–1089.